U.PORTO
FEUP FACULDADE DE ENGENHARIA
UNIVERSIDADE DO PORTO
INSTITUTO DE CIÊNCIAS
BIOMÉDICAS ABEL SALAZAR
UNIVERSIDADE DO PORTO

Nanoplatforms role in bacterial infections: design and development of new delivery systems and membrane mimetic models

Pedro Miguel Rodrigues Ribeiro da Costa

Master Thesis for the Degree in
Master in Bioengineering
Specialization in Molecular Biotechnology

Oriented by Cláudia Nunes Pinho
and Salette Reis

October, 2020

Nanoplatforms role in bacterial infections: design and development of new delivery systems and membrane mimetic models

Pedro Miguel Rodrigues Ribeiro da Costa

Master Thesis for the Degree in
Master in Bioengineering
Specialization in Molecular Biotechnology

October, 2020

This thesis is under the framework of the project Nano4Film - PTDC/NAN-MAT/31444/2017.

Resumo

A resistência bacteriana aos antibióticos é atualmente uma grande preocupação em todo o mundo, sendo os biofilmes da bactéria Gram-positiva *Staphylococcus aureus* um dos mais resistentes e também uma das causas mais comuns de infeções bacterianas humanas. Nesse contexto, estão a ser amplamente desenvolvidas alternativas às terapias convencionais e às metodologias de *screening* mais rentáveis. Em particular, abordagens baseadas na nanotecnologia estão a começar a fornecer estratégias eficientes para combater infeções bacterianas. Algumas nanopartículas já se mostraram eficazes como agentes antimicrobianos e na diminuição do desenvolvimento de resistência bacteriana. Em particular, nanopartículas superparamagnéticas de óxido de ferro (SPIONs) mostraram recentemente propriedades antibacterianas por meio de hipertermia magnética. No entanto, uma vez que os SPIONs são muito pequenos em tamanho e tendem a agregar-se, efeitos tóxicos (como obstrução dos vasos sanguíneos e acumulação em vários sistemas do corpo) representam uma desvantagem importante destas partículas. Deste modo, a sua combinação com outras nanopartículas - sistemas híbridos - pode ser uma alternativa promissora. Por outro lado, existe a necessidade de um *screening* mais eficaz de novas moléculas e nanossistemas. Os estudos de interação com bactérias são demorados e muitas vezes requerem condições especiais de trabalho. Nesse sentido, a nanotecnologia está também a ser explorada, através do desenvolvimento de sistemas miméticos da membrana bacteriana capazes de mimetizar a membrana externa das bactérias e estudar a sua interação com potenciais moléculas e sistemas terapêuticos. Entre eles, as vesículas unilamelares gigantes (GUVs) têm um papel fundamental.

Neste contexto, o plano de trabalhos iniciou-se com o desenvolvimento, otimização e caracterização de lipossomas fusogénicos carregados com SPIONs (magnetolipossomas PEGuilados) com caraterísticas adequadas para administração intravenosa, usando um desenho experimental do tipo Box-Behnken. A caracterização incluiu o tamanho, a polidispersão e a determinação da quantidade de SPIONS encapsulados. A formulação otimizada foi obtida para uma concentração lipídica de 30 mM utilizando 0,5 minutos de tempo de sonicação e 1,5 mL de SPIONs, tendo-se obtido resultados de caracterização de acordo com as previsões do modelo matemático. Posteriormente, GUVs com características similares à membrana da *S. aureus* foram desenvolvidos e preparados através de um processo de eletroformação. A capacidade fusogénica dos lipossomas magnéticos desenvolvidos foi avaliada, utilizando o modelo dos GUVs através de microscopia de fluorescência e lipossomas constituídos por 1,2-dimiristoil-*sn*-glicero-3-fosforilglicerol (DMPG) para ensaios de transferência de energia de ressonância Förster (FRET). A capacidade fusogénica foi verificada com ambos os modelos: com os

lipossomas, obteve-se uma eficiência FRET de 26,5%; com os GUVs, a fusão foi observada através da combinação de imagens de canais diferentes (FITC e TRITC), um para os GUVs e outro para os magnetolipossomas (com NBD e rodamina respetivamente, dois marcadores de fluorescência com diferentes espectros de excitação e emissão).

Abstract

Bacterial resistance to antibiotics is nowadays a major concern worldwide, with Gram-positive bacterium *Staphylococcus aureus* biofilms among the most resistant and also one of the most common causes of human bacterial infections. In this context, alternatives to conventional therapies and high-throughput screening methodologies are being widely researched. In particular, nanotechnology-based approaches are starting to provide efficient strategies to combat bacterial infections. Some nanoparticles have already shown effective as antimicrobial agents and to decrease the development of bacterial resistance. In particular, superparamagnetic iron oxide nanoparticles (SPIONs) have recently showed antibacterial properties through magnetic hyperthermia. Nonetheless, since SPIONs are very small in size and tend to aggregate, toxic effects (such as obstruction of blood vessels and sequestration in several body systems) represent an important drawback of these particles. Thereby, their combination with other nanoparticles – hybrid systems - may be a promising alternative. On another hand, there is a need for a more effective screening of new molecules and nanosystems. Interaction studies with bacteria are time consuming and many times require special work conditions. In this sense, nanotechnology is also being exploited, through the development of bacterial membrane mimetic systems able to mimic the outer membrane of bacteria and study their interaction with potential therapeutic molecules and systems. Among them, giant unilamellar vesicles (GUVs) have a pivotal role.

In this context, the work plan started with the development, optimization and characterization of fusogenic liposomes loading SPIONs (PEGylated magnetoliposomes) with suitable features for intravenous administration using a Box–Behnken design. The characterization included size, polidispersity and the determination of the amount of loaded SPIONS. The optimized formulation was obtained for a lipid concentration of 30 mM using 0.5 minutes of sonication time and 1.5 mL of SPIONs, with the characterization results in agreement with the mathematic model predictions. Afterwards, GUVs resembling the *S. aureus* membrane were developed and prepared through an electroformation process and the fusogenic capacity of the developed magnetic liposomes was evaluated, using the GUVs model through fluorescence microscopy and using 1,2-dimyristoyl-*sn*-glycero-3-phosphorylglycerol (DMPG) liposomes for Förster resonance energy transfer (FRET) assays. The fusogenic capacity was verified with both models: with liposomes, a FRET efficiency of 26,5% was obtained; with GUVs, the fusion was observable by merging images from different channels (FITC and TRITC), one for the GUVs and the other for the magnetoliposomes (with NBD and rhodamine respectively, two fluorescence dyes with different excitation and emission spectrums).

Acknowledgments

I never thought it would be more difficult to write acknowledgements than the introduction, but here we are, 30 minutes later, looking to a blank page reliving the last 5 years. What a journey it was, between two cities, three universities and countless colleagues. But let's get started.

I would like to thank, first and foremost, my supervisor Prof. Cláudia Nunes Pinho, for her support, guidance and encouragement during this year that was not easy for anyone. Yet, she was always there when I needed.

Secondly but equally important, thank you to Filipa Soares for all the hours by my side in the lab, it definitely required a lot of patience (ps: an extra thank you for all the 942 pieces of parafilm you cut for me! Maybe in another life I will be able to use a scissor!).

Thank you to my co-supervisor, Prof. Sallete Reis, and all the members of the MB^2 group for the warm welcome and integration. To Dr. David Pereira for his availability and all the help with the microscope.

To all my colleagues and specially my closest friends, for wandering these five years by my side, for all the hours in our virtual library (playing Counter Strike) and all the procrastination that kept us sane during the quarantine. For all the Chicken Bacons at Mc Donalds. For all the francesinhas. For all the suecas. For all the coffee breaks every 17 minutes. Danke (memes)!

A special thank you to the city and university of Aveiro, for giving me three of the best years of my life. To FEUP and ICBAS, a thank you for the journey, quite challenging but surely rewarding.

To my family, for all the support since the very first day. An eternal thanks to my parents, for everything. To my younger brother, for always remembering me that I was procrastinating instead of working while asking me to play with him. Oh, and for telling me that writing a thesis is so damn easy since I was able to play "all the time".

To Inês, mostly for getting mad every time I skipped writing to play Pokémon. Well, maybe also for being by my side even before these 5 years, for the support I cannot even describe, for believing in me even when I didn't, for grumbling when the profit of the day was less than 10 lines. For the lunches, snacks, dinners, vacations and all the escapes when needed. For being who you are. Thank you.

Contents

Chapter 6

List of Figures

List of Tables

Abbreviations and Symbols

A	Acceptor
AC	Alternating Current
CES	Carboxyethylsilanetriol
CFU	Colony-Forming Unit
CHEMS	Cholesterol Hemisuccinate
CL	Cardiolipin
D	Donor
DAPI	4′,6-diamidino-2-phenylindole
DLS	Dynamic Light Scattering
DMPC	1,2-dimyristoyl-*rac*-glycero-3-phosphocholine
DMPG	1,2-dimyristoyl-*sn*-glycero-3-phosphorylglycerol
DOE	Design of Experiments
DOPC	1,2-dioleoyl-*sn*-glycero-3-phosphatidylcholine
DOPE	1,2-dioleoyl-*sn-glycero*-3-phosphoethanolamine
DOPE-Rho	1,2-dioleoyl-*sn*-glycero-3-phosphoethanolamine -N-(lissamine rhodamine B sulfonyl)
DOPG	1,2-dioleoyl-*sn*-glycero-3-phosphatidylglycerol
DPhPc	1,2-diphytanoyl-*sn*-glycero-3-phosphocholine
DPPC	1,2-dipalmitoyl-*sn*-glycero-3-phosphocholine
DPPE	1,2-dipalmitoyl-*sn*-glycero-3-phosphoethanolamine
DPPE-NBD	1,2-dipalmitoyl-*sn*-glycero-3-phosphoethanolamine-N-(7-nitro-2-1,3-benzoxadiazol-4-yl)
DPPG	1,2-dipalmitoyl-*sn*-glycero-3-phosphoryglycerol
eDNA	Extracellular DNA
%EE	Encapsulation Efficiency
EPC	Egg phosphatidylcholine
EPS	Extracellular Polymeric Substance
FITC	Fluorescein-isothiocyanate
FRET	Förster Resonance Energy Transfer
GUVs	Giant Unilamellar Vesicles
ITO	Indium Tin Oxide
LB	Langmuir-Blodgett
LPs	Liposomes
LS	Langmuir-Schäfer
LUVs	Large Unilamellar Vesicles
Lysyl PG	1,2-dioleoyl-*sn*-glycero-3-[phospho-rac-(3-lysyl(1-glycerol))]
MHT	Magnetic Hyperthermia
MIC	Minimum Inhibitory Concentration

MLPs	Magnetoliposomes
MLVs	Multilamellar Vesicles
MNPs	Magnetic Nanoparticles
MRI	Magnetic Resonance Imaging
MRSA	Methicillin-resistant *Staphylococcus aureus*
MSCRAMMs	Microbial Surface Components Recognizing Adhesive Matrix Molecules
NBD	N-(7-nitro-2-1,3-benzoxadiazol-4-yl)
NMR	Nuclear Magnetic Resonance
NPs	Nanoparticles
PBS	Phosphate Buffered Saline
PDI	Polidispersity Index
PE	Phosphatidylethanolamine
PEG	Polyethylene Glycol
PG	Phosphatidylglycerol
PIA	Polysaccharide Intercellular Adhesin
PNAG	Polymeric N-Acetyl-Glucosamine
POEGA-b-PMAEP	Poly((oligo(ethylene glycol) methyl ether acrylate)-block-poly(monoacryloxyethyl phosphate)
POPC	1-palmitoyl-2-oleoyl-*sn*-glycero-3-phosphatidylcholine
POPE	1-palmitoyl-2-oleoyl-*sn*-glycero-3-phosphatidylethanolamine
POPG	1-palmitoyl-2-*oleoyl*-*sn*-glycero-3-phosphatidylglycerol
PS	Phosphatidylserine
PVA	Polyvinyl Alcohol
PVP	Polyvinyl Pyrrolidine
Rho	N-(lissamine rhodamine B sulfonyl)
ROS	Reactive Oxygen Species
SLBs	Supported Lipid Bilayers
SPIONs	Superparamagnetic Iron Oxide Nanoparticles
SUVs	Small unilamellar vesicles
T_M	Phase Transition Temperature
TRITC	Tetramethylrhodamine-isothiocyanate

α-	Alpha
β-	Beta
γ-	Gamma
δ-	Delta

Chapter 1

Bacterial Infections

The increasing investigation and development of new nanotechnologies over the last years has enhanced their potential applications within biomedical sciences, with a major focus in targeted drug delivery systems, theranostics applications and new therapeutics, such as for the control of infectious diseases. In the past decades, antibiotic resistance has become a major concern for the medical community and a rising issue for the public health in general, following the prevalent use of antibiotics all around the globe, often poorly controlled (Labruère *et al.*, 2019). An example is the bacteria *Staphylococcus aureus*, a human pathogenic agent with already several known resistant strains: the two most common are the methicillin-resistant *S. aureus* and vancomycin-resistant *S. aureus*. Additionally, in response to aggressive conditions, *S. aureus* can form biofilms, bacterial communities typically wrapped in self-produced extracellular polymeric substances (EPS), decreasing the susceptibility to both antibiotics and the immune system (Archer *et al.*, 2011). A small overview focused on *S. aureus* biofilms will be provided below, while the *nano* approaches for its treatment will be addressed in the following chapter.

1.1. *Staphylococcus Aureus*

With a gram-positive coccus, *S. aureus* is a non-motile and non-spore forming bacteria, belonging to the *Micrococcaceae* family. It is a facultative anaerobe bacterium, however, it

presents a better development under aerobic conditions (Kanafani and Fowler, 2006). The human host is one of the many species that *S. aureus* has adapted to, with the transmission through organisms occurring upon contact, either by skin-to-skin contact or contaminated object-skin contact, or through coughing and sneezing. Although a representative percentage of the population are healthy carriers of *S. aureus*, there is a potential hazard associated with the penetration of this bacterium through the epithelial and mucosa layers. Hence, it can reach the bloodstream and lead to severe infections in the bone, brain, blood and other organs, where *S. aureus* can release lethal toxins, such as α-, ß-, γ-, and δ-toxins and enterotoxins (Labruère *et al.,* 2019).

Due to *S. aureus* portfolio full of possible infections, numerous antibiotics were developed in the last century, where penicillin and methicillin (a penicillin analogue) found a major role (Labruère *et al.,* 2019). However, the extensive and under controlled use of such antibacterial agents led to the appearance of *S. aureus* strains that acquired genes for drug resistance. Methicillin-resistant *S. aureus* (MRSA) is the most common example of antibiotic-resistant strain in these bacteria, with vancomycin, linezolid and daptomycin as some of the antibiotics used against it. Yet, resistant *S. aureus* against those were already identified (Gu *et al.,* 2013; Mcguinness *et al.,* 2017; Sabat *et al.,* 2018). Moreover, the majority of antibiotics struggle to reach the infection site across several possible locations of *S. aureus*, including the fatty tissue and the surfaces of bone and implanted devices (Labruère *et al.,* 2019). Another limitation to the effectiveness of antibiotics is the formation of biofilms.

By definition, bacterial biofilm is a complex and differentiated community of bacteria, attached to an inert or biological surface and to each other and embedded in a matrix of self-produced EPS (Archer *et al.,* 2011). The bacterial cell cluster forming the biofilm, so-called sessile cells, display an altered phenotype, affecting their growth, gene expression and protein production. Additionally, the thickness can range from a singular layer to complex multilayer domains. Structurally, biofilms can be divided based on the cell activity, with the majority of cells located on inner layers, characterized by an anoxic environment where cells adopt a dormant state. In the surface, cells remain metabolically active. Depending on the nutrient source, biofilm growth can be mushroom or flat-shaped (Hall-Stoodley *et al.,* 2004). Additionally, bacteria can communicate between each other, in a process called quorum sensing, strengthening the cooperation in response to hostile environments. Thus, treating biofilm infections presents several complications, facing substantial resistance to antibiotics coupled with high evasiveness to the immune system. The combination of these two adversities rises the morbidity and mortality of chronic infections caused by biofilms (Forier *et al.,* 2014). Different mechanisms of antimicrobial resistance were already proposed, such as limited diffusion into the matrix, antimicrobial agent deactivation through binding with matrix components or due to the development of dormant persister cells as examples (Forier *et al.,* 2014; Lister and Horswill, 2014).

S. aureus is a major biofilm-producing pathogen, associated with serious chronic infections. The matrix is predominantly composed of polysaccharide intercellular adhesin (PIA), a polymer with a noteworthy impact on the architectural integrity of the biofilm, also found in biofilms of *S. epidermidis* (Lister and Horswill, 2014). It is also known as polymeric N-acetyl-glucosamine (PNAG) and the enzymes responsible for its production are encoded in the *icaADBC* locus. Besides PIA, the matrix is also composed of host factors, secreted and lysis-derived proteins and extracellular DNA (eDNA), where the impact of each factor depends heavily on the environment and the specific *S. aureus* strain in question (Lister and Horswill, 2014). Regarding the stages of development, *S. aureus* biofilms have a similar pathway as other bacterial species, following a three-steps sequence – attachment, maturation and dispersion, with subphases in between. Initially, a planktonic cell needs to attach to a surface, a procedure mediated by microbial surface components recognizing adhesive matrix molecules (MSCRAMMs) in biotic surfaces or driven by hydrophobic, electrostatic and Van der Waals interactions in abiotic surfaces (Mohammed *et al.,* 2018; Moormeier and Bayles, 2017). These MSCRAMMs promote intercellular binding shortly after initial attachment, leading to a multiplication period, characterized by a progressive proliferation of the biofilm. Before the maturation step, an early dispersal event occurs via a nuclease-dependent degradation of eDNA – a process not fully understood called "exodus". It allows the formation of three-dimensional microcolonies, functioning as a base for the maturation step. The final step is the biofilm dispersion, finding new invasive phases to initiate new planktonic attachments and the development of more biofilms (Moormeier and Bayles, 2017). The preferred dispersal mechanism used by *S. aureus* is the production of enzymes and surfactants to disrupt the EPS matrix, with the effectiveness depending on the specific composition of the strain. The most common enzymatic dispersal mechanisms are mediated by proteases, nucleases and dispersin-B (Lister and Horswill, 2014). Moreover, several dispersal mechanisms have been linked with the *agr* quorum sensing system, which plays a role on the production of dispersal-mediating proteases and induces the expression of both proteases and phenol-soluble modulins (PSMs). These surfactant peptides, already proven to be effective in the dispersion of *S. aureus* biofilms (Lister and Horswill, 2014).

Biofilms remain linked with a substantial burden to the healthcare system, commonly associated with various medical devices and human chronic infections (Pinto *et al.,* 2020; Del Pozo 2018). With all the resistances acquired, *S. aureus* biofilms are one of the most prevailing, on both categories. Countless strategies to overcome the formation and proliferation of biofilms were already studied, with the novel strategies currently focused on the EPS matrix as a barrier to overcome through the use of matrix disruptive agents (Pinto *et al.,* 2020). Here, the biofilm dispersal agents are reversed against itself, engineered to be used for the biofilm disassembly, with enzymes and mucolytic agents as the main strategies. Additionally, nanosystems can also be used as a twofold strategy, in both targeting and disruption of the matrix. Gold nanoparticles (NPs), positively charged lipids and polymeric-based NPs already

proved to be effective against biofilms. For example, Hasan *et al.* (2019) developed polymeric NPs capable of binding to the biofilm matrix to facilitate nitric oxide delivery to MRSA biofilm-infected diabetic wounds (Hasan *et al.*, 2019). Pinto *et al.* (2019) explored the impact of several nanosystems in *S. aureus* biofilm treatment, reporting an extraordinary amount of nanoformulations already developed as an attempt to eradicate *S. aureus* biofilms (Pinto *et al.*, 2019). In addition to lipid and polymeric-based NPs, quantum dots, metallic and silica-based nanosystem were also stated.

Recently, innovative technologies for biofilm physical removal were proposed, primarily focused on the application of magnetic fields combined with NPs, photodynamic therapy, ultrasounds and laser-induced microbubbles. Pinto, Soares and colleagues (2020) published a review on these topics, highlighting the bacteria strain used in each experiment, with a higher focus on *S. aureus* and MRSA strains (Pinto *et al.*, 2020). All the recent therapies mentioned before are illustrated in Figure 1.

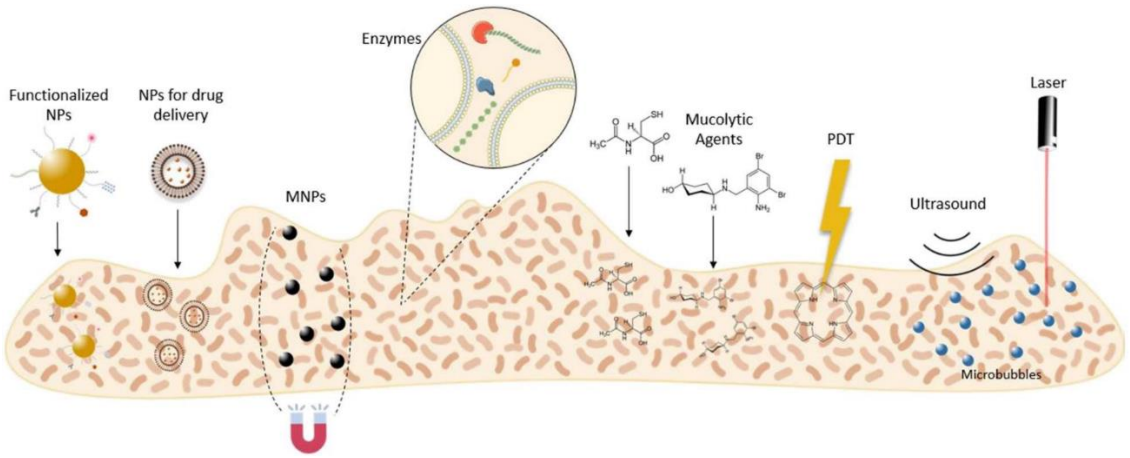

Figure 1 - Innovative strategies for biofilm eradication through matrix disruption. Reproduced with permission from the authors (Pinto et al., 2019)

Herewith, the next chapter will provide an overview on a specific nano approach for biofilm disruption, resulting from the combination of liposomes as the nanocarrier, loaded with iron oxide nanoparticles.

Chapter 2

Nanossystems as a Solution

The urgent need for innovative strategies able to fight the resistance that many pathogenic bacteria acquired against the most commonly used antibiotics, led to several possible approaches proposed, but one of them is gaining considerable attention. The research for nanomedicines, more precisely based on lipid and polymer nanoparticles, has seen the number of publications sharply increase over the last decade, with various desirable properties on their side. Specifically, lipid based nanoparticles can deliver antimicrobial agents directly to the bacterial cell, by fusing with their outer membrane, thus maximizing the therapeutic effect (Forier *et al.*, 2014). This nanotechnology approach, combined with metal nanoparticles such as superparamagnetic iron oxide nanoparticles (SPIONs), represents a solid strategy against the increasing antibiotic resistance of bacteria, and will be further discussed below.

2.1. Liposomes

In 1963, Alec Bangham was able to obtain a "spontaneous formation of unlimited closed membrane ('smectic mesophases')". Two years later, he established the major properties of the 'smectic mesophases' as a cell membrane model. From that moment onwards, this model was called liposome (LP) (Bangham, 1993).

LPs can be defined as sphere-shaped phospholipid-based vesicles composed by one or more phospholipidic double layers concentrically arranged around an aqueous core. Size-wise,

these nanocarriers can range from incredible small vesicles (0.025 μm) (Akbarzadeh *et al.*, 2013) to amazingly large ones (up to 200 μm) (Dimova and Marques *et al.*, 2012). Based on their number of bilayers, liposomes have two classifications: multilamellar vesicles (MLVs) and unilamellar vesicles. The last can be classified regarding size, with vesicles under 100 nm called small unilamellar vesicles (SUVs), between 100 nm and 1 μm called large unilamellar vesicles (LUVs) and above 1 μm called giant unilamellar vesicles (GUVs).

LPs possess several advantages that justifies their title as the main delivery nanosystem in cosmetics and pharmaceutical industries. Their size and structure allows both hydrophobic and hydrophilic drugs to be encapsulated into the phospholipid bilayer and the aqueous core respectively, while the bilayer composition regulates charge, rigidity and fluidity of the cell-like membrane. Moreover, LPs present high biocompatibility, low immunogenicity, flexibility, biodegradability, reduce drug toxicity, increase efficiency, stability and ensures protection for the drug or active biomolecule (Akbarzadeh *et al.*, 2013). In order to maximize the efficacy of LPs for each specific application, their physiochemical properties can be modified. Besides the ones already addressed, the pH and temperature sensitivity also have a significant role (Drulis-Kawa and Dorotkiewicz-Jach, 2010).

There are several methods already well established to prepare these vesicles, but the core is the same to all: after drying down the lipids from an organic solvent, they are dispersed in an aqueous media, purified and then analyzed. The most common methods can be divided between mechanical dispersion, solvent dispersion and detergent removal (Akbarzadeh *et al.*, 2013).

As referred before, drug resistance amongst bacterial pathogens is a serious problem restringing the traditional therapies, and LPs are the most widely used nanocarrier for antimicrobial drug delivery. The interaction with the cell membrane, either by a mediated or passive fusion process, allows a direct delivery of the drug into the membrane of the target, which may reduce the amount of antimicrobial drug required to maximize the therapeutic effect. These LPs can be called fusogenic liposomes and will be addressed below.

2.1.1. Fusogenic Liposomes

Fusogenic liposomes are traditional LPs with two unique features: not only they present a more fluid lipid bilayer but, with the right lipids chosen for the assembly, can also promote the disruption of biological membranes. Thus, a more direct drug deliver into cells is accomplished, reducing unwanted interactions with the environment around the target (Forier *et al.*, 2014; Rukavina and Vanic, 2016).

The fluidity of fusogenic liposomes can be tweaked, depending on the lipids in play. One example is the combination of cholesterol hemisuccinate (CHEMS) with 1,2-dioleoyl-*sn*-

glycero-3-phosphoethanolamine (DOPE)(Scriboni *et al.*, 2019), used alone or with other phospholipids. Due to the DOPE acyl chains based on oleic acid, its main phase transition temperature (T_M) is very low, thus dropping the overall T_M of the obtained liposome. Thereby, these fusogenic liposomes tend to be in the liquid crystalline phase, allowing them to lose the bilayer arrangement and fuse under some conditions, like acidic media or in the presence of cations (Scriboni *et al.*, 2019). Moreover, the T_M can be even lower, if the chosen phospholipids have smaller acyl chains (Forier *et al.*, 2014). However, Scriboni and co-workers reported that the use of 1,2-dipalmitoyl-*sn*-glycero-3-phosphocholine (DPPC) was required for stabilization of the lipid bilayer, as a consequence of the presence of DOPE, which promotes destabilization at acidic pH (towards inverse hexagonal structures) (Scriboni *et al.*, 2019).

In order to begin the fusion process between the liposomal membrane and the target membrane, the vesicle needs to adhere or aggregate to the membrane. This is the first step required and mediated by different interaction forces such as electrostatic interactions, attractive Van der Waals interactions and hydration forces. Secondly, a small perturbation in the site of interest of the lipid membrane occurs, due to the fluidity presented by the LP membrane. With that, the outer monolayers begins to merge, and the fusion is completed after the mixing of the inner content of the vesicles and their membranes. This procedure can be accelerated with different fusogens, ranging from fatty substances like lysolecithin, to inert biological elements such as metal ions. The fusion also depends on other aspects, like temperature, pH, the surface charge and the size and constitution of both vesicles in play (Wang *et al.*, 2016).

The most widely used method for monitoring and quantifying membrane fusion is the lipid-mixing assay, using a Förster resonance energy transfer (FRET) technique (Forier *et al.*, 2014). The most common labeled liposomes used are derivates of N-(lissamine rhodamine B sulfonyl) (Rho) and N-(7-nitro-2-1,3-benzoxadiazol-4-yl) (NBD) – *e.g.* combined with 1,2-dipalmitoyl-*sn*-glycero-3-phosphoethanolamine (DPPE) or DOPE – representing the acceptor and donor fluorescence dyes, respectively (Kao *et al.*, 2012; Lira *et al.*, 2019; Wang *et al.*, 2016). The underlines of this procedure will be discussed later in the materials and methods chapter. Additionally, there are less used techniques, like negative staining, fluorescence activated cell sorter and immunoelectron microscopy (Rukavina and Vanic, 2016; Wang *et al.*, 2016). However, the lipid-mixing assay has proven to be more reliable, since it measures the distance between the two fluorescent probes (one in the fusogenic liposome and the other in the bacteria), while other methods evaluate vesicular aggregation (Wang *et al.*, 2016).

Wang *et al.* (2016) have studied the mechanism of fusion between tobramycin-encapsulated fusogenic liposomes (composed of DPPC/1,2-dimyristoyl-sn-glycero-3-phosphorylglycerol [DMPG] 9:1) with different bacteria cells (*P. aeruginosa*, *E. coli*, *B. cepacia*, *S. maltophilia* and *S. aureus*) and the different factors involved. The highest percentage of fusion was obtained near the T_M of the fluid liposomes – 37°C – and with both low pH and high

pH. Regarding the effect of various divalent cations in the medium, Fe^{2+} presented the best degree of fusion, followed by Mg^{2+}, Ca^{2+} and Ba^{2+}, in that order. The authors had already studied the influence of the size and demonstrated that fusion is not dependent on either liposomal size or lamellarity, with same results across a wide range of diameters – 100 to 800 nm. Additionally, the level of fusion was shown to be dependent on the membrane fluidity, decreasing with the addition of cholesterol – responsible for perturbations in the fluid state – while increasing with higher PE content in the outer membrane. However, the most important identified factor in liposome-bacterial fusion was the nature of the bacterial membrane, with gram-negative bacteria presenting superior degrees of fusion compared to gram-positive bacteria. The bactericidal efficacy was also evaluated and compared to PBS and free tobramycin, with the liposomal formulation having a quicker effect in the bacteria, which may be justified by the fusion process. The tobramycin encapsulation efficiency was superior to 70% for all the preparations (Wang *et al.*, 2016).

A recent study from Scriboni and co-workers (2019) was aimed at studying different vancomycin-encapsulated liposomal preparations and compare their *in vitro* antimicrobial activity against *S. aureus* biofilms. Fusogenic liposomes of DOPE:DPPC:CHEMS (4:2:4) were prepared following a composition already well-established in the literature (Nicolosi et al. 2010). The 50x MIC (Minimum Inhibitory Concentration) results demonstrated that fusogenic liposomes encapsulated with vancomycin present better antimicrobial activity than cationic liposomes, traditional liposomes and free vancomycin (Scriboni *et al.*, 2019).

With several reports already published about the bactericidal effect of antibiotic-encapsulated fusogenic liposomes, this method allows an effective drug delivery to bacterial cells with increased contact between cell and antibiotic, and therefore a more efficient antibacterial activity. Moreover, fusogenic LPs ensures protection of the antibiotic from degrading enzymes. Yet, a new foe appeared when bacteria began to resist the most common antibiotics and such resistance is improving fast. A possible solution may be combining liposomes with magnetic nanoparticles, particularly superparamagnetic iron oxide nanoparticles (SPIONs), to obtain promising multifunctional nano weapons against antibiotic-resistant bacteria, presenting good biocompatibility and magnetic behavior as key properties. These nanoformulations will be addressed in the next section.

2.2. SPIONs

The interest towards magnetic nanoparticles has been rising in the scientific community, furthering several investigation areas such as biotechnology, biomedical, engineering, material science and environment-focused research, each one facing their challenges (Akbarzadeh, Samiei and Davaran, 2012). For biomedical uses, SPIONs remain as one of the most useful

nanosystems. Here, the nature of the magnetic component, the size of the particles, the coatings and the concentration strongly influence the NP's toxicity and biocompatibility (M. Mahmoudi *et al.*, 2011).

In fact, the applied coating deeply influences the potential of these NPs, mainly for biomedical applications. It acts as a shield for the magnetic particle from the surrounding environment, reducing SPION's agglomeration and increasing their stability. Also, an extra functionalization, by adding biotin, avidin, carboxyl groups and other molecules, can increase the direct targeting of these particles (M. Mahmoudi *et al.*, 2011). Different coatings have already been reported, from polyethylene glycol (PEG), polyvinyl pyrrolidine (PVP), polyvinyl alcohol (PVA) and chitosan to other compounds such as silica and dextran. A common example is dextran coating of SPIONs with cores between 3 to 6 nm for magnetic resonance imaging (MRI), which have already originated commercial products like Feridex, Endorem, Combidex and Sinerem (M. Mahmoudi *et al.*, 2011). Additionally, SPIONS have also already been combined with other nanoparticles, like liposomes, which will be discussed on a following section.

SPIONs are, by far, the most used NPs for biomedical applications – *e.g.* magnetite (Fe_3O_4), maghemite (γ-Fe_2O_3) and hematite (α-Fe_2O_3) (Akbarzadeh *et al.*, 2012). These magnetic compounds present a magnetic behavior when an external magnetic field is applied, but, once that field is removed, the particles no longer show magnetic interaction, due to their reduced size and increased surface-to-volume ratio. This phenomenon is called superparamagnetism.

2.2.1. Superparamagnetism

Using an external magnetic field combined with micron size magnetic ions was already introduced in the past century (Freeman, Arrott and Watson, 1960), gathering considerable attention for various targeted drug delivery applications. The concept was deeply exploited, and nowadays magnetic NPs show remarkable properties, such as high field irreversibility, high saturation field, extra anisotropy contributions, shifted loops after field cooling and the already mentioned superparamagnetism (Akbarzadeh *et al.*, 2012). When exposed to an external magnetic field, the behavior of the most traditional magnetic materials (ferri- and ferromagnetic) follows a hysteresis loop, which is defined by two parameters: coercivity (H_c) and remanence. The first one is strongly size-dependent and becomes zero when the size drops below a certain diameter (d_{SP}), as observable in Figure 2 (Koo *et al.*, 2019).

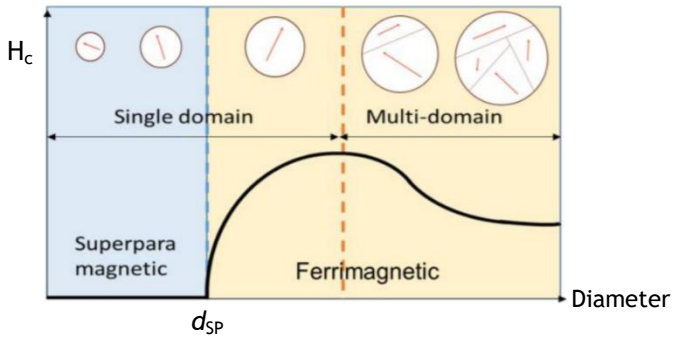

Figure 2 – Relation between coercivity (H_C) and particle diameter. Adapted from Koo et al., 2019

This phenomenon is the superparamagnetism, where thermal variations are strong enough to demagnetize the particles previously magnetized with the external field, returning them to a nonmagnetic state (Akbarzadeh *et al.*, 2012). Thus, having nearly no hysteresis and avoiding magnetism in the absence of external field (Figure 3). This property allows SPIONs to be incredible particles for biological applications, from targeting drug delivery to MRI.

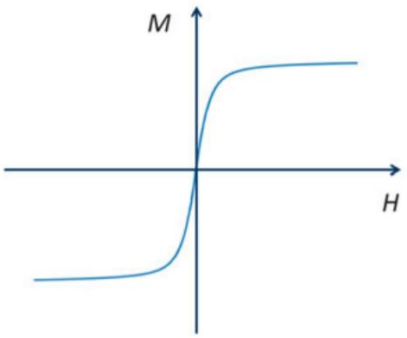

Figure 3 - Superparamagnetic particles magnetization (H) as a function of the applied magnetic field(M) . Adapted from Majetich et al., 2013

The size of NPs is one of the most important features affecting the potential for developing superparamagnetic properties. As the nanoparticle size is reduced, a diameter at which the coercivity reaches the maximum value can be identified, where the magnetic nanoparticles go from a multi-domain to a single-domain; from there, a small decrease can result in the coercivity rapidly drop to zero (Figure 2). The nanoparticles became superparamagnetic at that moment (Majetich *et al.*, 2013).

2.2.2. Hyperthermia

SPIONs already have a significant importance in several clinical applications, both diagnostics and therapeutics. Recently, their potential as theranostic agents have also been addressed, with cancer theranostic applications as one of the main focus for these NPs (Kandasamy *et al.*, 2018; Kandasamy and Maity, 2015; Musielak *et al.*, 2019; Zhang and Song, 2017). Furthermore, one of the two major areas of applications for SPIONs is MRI related applications, focusing on cancer diagnosis and theranostics, with SPIONs as T2 MRI contrast agents (Guo *et al.*, 2015; Rost *et al.*, 2020). Targeted drug delivery is the other major field of research for these particles, with SPIONs-assisted drug delivery systems capable to deliver peptides, DNA molecules and various drugs (such as chemotherapeutic and radioactive agents) (Mahmoudi *et al.*, 2011)). Other applications of multifunctional SPIONs include stem cell tracking, gene delivery and hyperthermia (Mahmoudi *et al.*, 2011). This last therapy holds a great potential for cancer treatments and bacterial biofilm inactivation.

Hyperthermia therapy is defined as the elevation of the body temperature, carried out by irradiation of light, electromagnetic waves or external medical devices (Kandasamy and Maity, 2015). It can be divided into three categories: local, regional and whole-body hyperthermia. Such temperature increase can lead to intracellular heat stress, degradation of cellular components, abnormal protein folding and aggregation, pH variations and possible cell death (Musielak *et al.*, 2019). This therapy found the most success when applied as a cancer treatment, and for that purpose, magnetic hyperthermia (MHT) was proposed. Recently, other applications have been explored with magnetic hyperthermia, performed by using SPIONs to heat targeted areas with an alternating, time-varying magnetic field (AMF) (Zhang and Song, 2017). SPIONs have the capacity to randomly flip the magnetization direction, allowing the transformation of electromagnetic energy into heat, being considered as one of the most effective heating particles for local hyperthermia. Moreover, SPIONs can be incorporated by the target cells, leading to heat deliver at a single cell level, due to their small size (Seabra *et al.*, 2017). In fact, nano-sized particles present much more absorption power at bearable AC magnetic fields than micron-sized particles (Akbarzadeh *et al.*, 2012). The heat can also be controlled by the applied field and several properties of the SPIONs, such as shape, crystallinity, composition and magnetic features (Kandasamy and Maity, 2015).

2.2.3. Cytotoxicity

As a therapy meant to interact with a biological host, it is of extreme importance to consider several details regarding hyperthermia. Even with numerous magnetic NPs available, SPIONs

are the gold standard for MHT. For biomedical applications, MNPs must be composed of a non-toxic and non-immunogenic material, with such a small size that allows a prolonged circulation and the passage through the capillary system, avoiding vessel embolism due to agglomerates (Akbarzadeh *et al.*, 2012). Although the hysteresis loop of other magnetic particles (ferrimagnetic and ferromagnetic) may induce a greater hyperthermia effect, it also might lead to embolization (Laurent *et al.*, 2011). Therefore, SPIONs are preferred for *in vivo* applications, assembling various advantages – good biocompatibility and theranostic potential, capable to be functionalized, guided by a magnetic field with demagnetization once the field is removed, reduced side effects for the patients and without detectable cytotoxicity. However, it is imperative to understand the toxicity range of SPIONs and how they interact with the human body.

The four key parameters of SPIONs impacting biocompatibility and toxicity were already pointed – the nature of the magnetic component, the final size, the coating and the concentration of the SPION (M. Mahmoudi *et al.*, 2011). With the increased attention that these nanoparticles gained recently, several cytotoxicity studies have been conducted. Firstly, the interaction between SPIONs and the target cell can occur by various possible mechanisms, like passive diffusion, receptor mediated endocytosis, clatharin mediated endocytosis and caveoline mediated endocytoses (Patil *et al.*, 2018). Secondly, the exposure to SPION could theoretically lead to diminished mitochondrial activity, inflammation, membrane leakage, formation of apoptotic bodies, chromosome condensation, DNA damage and generation of reactive oxygen species (ROS) (Patil *et al.*, 2018). After entering the cell, enzymes can degrade SPIONs, forming Fe^{2+} ions, which are responsible for the generation of ROS, by modifying mitochondrial and other organelle functions (Singh *et al.*, 2010). However, adding a biocompatible coating to the SPION may have a negative correlation with toxicity. Mahmoudi and colleagues (2009) studied the effect of a PVA coating in the SPION's toxicity against a mouse fibroblast cell line, obtaining a polymer/iron mass ratio of approximately 3 as the maximum level to maintain the greatest compromise for both biocompatibility and magnetic saturation (M. Mahmoudi *et al.*, 2009).

An extensive compilation of cytotoxic assays was performed by Mahmoudi *et al.* (2012), highlighting the cell line used, the average SPIONs size, the coating material, the concentration of SPIONs, the exposure time and the toxicity evaluation assay used by each research paper (Mahmoudi *et al.*, 2012). With numerous scientific reports presented, some conclusion could be gathered, regarding the concentration – SPIONs appear to be non-toxic at low concentrations, with some articles showing no-cytotoxicity up to 100 µg/mL. Depending on the coating, the size of the SPIONs and the cell line used, concentrations as high as 1 mg/mL were also reported as non-toxic in some cases. For example, Gholami *et al.* (2018) tested the *in vitro* cytotoxicity of PVA-coated SPIONs with various concentrations on Neuro2A and HUVEC cells, after 24h of treatment. The results showed no toxicity for both cell lines up to 37.5 µg/mL,

diverging after that concentration – for HUVEC cells, no toxicity was found, with cellular viability superior to 80% even after 150 μg/mL; however, for N2A cells, a decrease in the viability was observed, dropping the viability to 50% with 150 μg/mL SPIONs (Gholami *et al.*, 2018).

2.2.4. SPIONs and Biofilm Disruption

The research from the last decades has been crucial for the development and improvement of techniques using SPIONs for biomedical applications. Besides the plethora of studies focused on cancer theranostics, a revolutionary application was recently established – antibacterial activity, focused on eradication and inactivation of bacterial biofilms. In this context, SPIONs can be used to heat targeted areas relaying on the energy from the external magnetic field. Moreover, their size allows a site-specific penetration into the bacterial biofilm (Seabra *et al.*, 2017).

Eradication of biofilms can face several drawbacks, since their growth favors a dormant state for the bacteria in the inner layers of the biofilm and the amount of antibiotic-resistant strains are rising. Subbiahdoss *et al.* (2012) studied the SPION's effect in the treatment of biomaterial-associated infections (BAI), looking for a deep penetration into the biofilm followed by eradication. In this context, various surface-modified SPIONs were tested – bare, with carboxyethylsilanetriol (CES), with aminopropyltriethoxysilane (APTES) and with PEG – against gentamicin-susceptible *S. aureus* and gentamicin-resistant *S. epidermidis*, with the help of an external magnetic field. The results confirmed the antibacterial efficacy of these SPIONs against adhering *Staphylococci*, with increased percentage of disruption when applied the magnetic field. CES-grafted SPIONs were directed into a gentamicin-resistant biofilm, yielding an 8-fold higher antibacterial efficacy, compared to gentamicin. Moreover, PEGylated SPIONs were not able to perform an antibacterial role, compared to the other surface-modified SPIONs (Subbiahdoss *et al.*, 2012). However, such modification was already used to enhance contrast efficiency in MRI (A. Carvalho *et al.*, 2014).

In 2011, Park *et al.* used SPIONs to increase the temperature of a *P. aeruginosa* biofilm, by producing local hyperthermia with an AC magnetic field. With SPIONs at concentrations from 10 to 60 mg/mL, the temperature increased from 20°C up to 60°C in 4 min (and maintain that value in the following 4 min), for the most concentrated SPION solution. For that solution, a higher than 4 log inactivation of the biofilm was obtain, in the first 8 min, while no inactivation was detected without the magnetic field (Park *et al.*, 2011).

Taylor *et al.* (2012) studied the antibacterial properties of SPIONs coated with many antibacterial metals, such as silver, iron and zinc, using *S. aureus* antibiotic-resistant biofilms and compared the obtained results with the most traditional antibiotics used (vancomycin,

penicillin, oxacillin, gentamicin and streptomycin). The most effective formulation against the antibiotic-resistant biofilm was the zinc conjugated SPIONs. Although, for planktonic bacteria, the silver conjugated SPIONs presented the best antimicrobial activity (Taylor et al. 2012).

Local hyperthermia was also studied by Nguyen *et al.* (2015) as a detachment agent of *Pseudomonas aeruginosa* biofilms, mediated by iron oxide nanoparticles (IONPs), coated with poly((oligo(ethylene glycol) methyl ether acrylate)-block-poly(monoacryloxyethyl phosphate) (POEGA-b-PMAEP). The treatment resulted in 69.2% biofilm dispersion after 20 min, with the temperature increasing from 23 to 40°C, while the treatment without external magnetic field was only able to decrease 19.7%. Moreover, when the IONPs were added in the beginning of the biofilm growth and only magnetically activated 24h later, during the standard 20 min, the obtained reduction in biofilm colony-forming unit (CFU) was 93.8% and an increase of 614% was observed for planktonic CFU, compared to untreated cultures (Nguyen et al. 2015).

The requirement of a coating is a common element across all the articles presented, in order to increase SPION's biocompatibility. A different method of protecting the nanoparticle while reducing the possible toxicity will be mentioned below, built with another nanosystem – liposomes. In this multifunctional nanosystem known as magnetoliposomes (MLPs), SPIONs are encapsulated in LPs, replacing the traditional coatings.

2.3. Magnetoliposomes

Combining liposomes with SPIONs, two well-established nanosystems with an overabundance of incredible qualities by both sides, outlines the innovation by which nanotechnology is known. In this scenario, it is possible to obtain hybrid nanosystems with higher therapeutic proficiency, while also increasing its biocompatibility. The main application for these nanosystems are in line with the already known applications of both LPs and SPIONs, representing a possible solution to improve such systems. Thus, research is focused on their potential as MRI contrast agents (Faria *et al.*, 2013; Garcia Ribeiro *et al.*, 2018) and drug delivery application (Joniec *et al.*, 2016; Shirmardi Shaghasemi *et al.*, 2017), looking for a magnetically-mediated and controlled release of the encapsulated drug. Antibacterial activity has also been reported (Da Costa e Silva *et al.*, 2018).

In order to prepare the SPION-liposome hybrids, some SPIONs properties will influence their final localization within the liposome. The surface chemistry is one of them, impacting both colloidal stability and the association to the liposome. The preparation method and the SPIONs geometry are also crucial to consider. Regarding the spatial localization, two major strategies are possible, as SPIONs can be directly encapsulated within the liposome lumen or between the liposome bilayer (Monnier *et al.*, 2014). Another possible approach was also proposed – direct conjugation to the liposome surface – but has been masked by the potential

of the two addressed before. The addition of a surface functionalization can modulate the SPIONs location and therefore the desired application, conferring them either hydrophobicity (*e.g.* fatty acids and dopamine derivates) or hydrophilicity (*e.g* carboxylates). For example, the preferred location of SPIONs for drug delivery is between the lipid bilayer, since it prevents SPIONs-drug contact and possible damage to the drug (Monnier *et al.*, 2014). Moreover, it allows a more effective disruption of the bilayer, improving the drug release mediated by a magnetic trigger. For this location, the coating should be hydrophobic, allowing SPIONs to be stable inside the hydrophobic chains of the bilayer. For MRI tracking, the preferred location is the lumen (Monnier *et al.*, 2014).

Besides the applications already mentioned, the properties presented by magnetoliposomes should provide an incredible nanosystem for biofilm disruption therapies. In the outside, the fusogenic capacity of LPs can improve the diffusion into the biofilm, while the inner content is responsible for an additional guidance, relying on the external magnetic field applied. Moreover, SPIONs already proved to be excellent candidates for antibacterial applications. For this scenario, the best localization for the SPIONs is the liposome's lumen, mainly due to the fusogenic property and encapsulation ratio. The presence of SPIONs between the bilayer could compromise the fusion process and their release into the biofilm, whereas in the lumen a higher quantity of uncoated SPIONs could be encapsulated.

By now, only one paper was published testing the antibacterial activity of MLPs against *S. aureus*. Da Costa e Silva *et al.* (2018) prepared three different liposomal formulations – with stigmasterol, with magnetite NPs coated with lecithin and with both – and evaluated their antibacterial activity against *S. aureus* and *Citrobacter freundii*. The inhibition of microbial growth after 24h was calculated in three different conditions – without magnetic field (at room temperature and 41°C) and with a magnetic field at 41°C. The temperature was set at 41°C to avoid damage to healthy human cells. The obtained results showed that, in the absence of magnetic field, the temperature elevation led to bacterial growth. However, the addition of the magnetic field increased the inhibition percentage of *S. aureus* up to 98% for the formulation with only magnetite. For *C. freundii*, all formulations obtained results under 50% even in the presence of a magnetic field. Therefore, the liposomal formulation with only magnetic NPs showed the best inhibitory response, with 98% of *S. aureus* inhibition under a magnetic field, equivalent to a MIC of 8.4 μg/mL for magnetite (Da Costa E Silva *et al.*, 2018).

2.4. PEG as an Approach

A common link between the different applications of MLPs is the interaction with the human body, which identifies these vesicles as foreign, leading to several undesirable reactions that can compromise the outcome pretended. To prevent such result, the exterior surface of the

liposomes can be further functionalized with a proper coating, where flexible PEG chains between 2000 and 5000 Da represent the most widely used coatings (Nuytten *et al.*, 2010). PEG is a biocompatible and hydrophilic polymer with the molecular formula $HO\text{-}(CH_2\text{-}CH_2\text{-}O)_n\text{-}H$ (Figure 4), already approved by the US Food and Drug Administration (FDA) for numerous biomedical applications (Shen *et al.*, 2018). It provides stealth capabilities in the human body, increasing the blood circulation time while avoiding clearance by the reticuloendothelial system. Moreover, in general it also increases the storage stability. The term "stealth" drives from the reduced uptake by macrophages, due to the steric stabilization from adsorbing plasma proteins, a property provided by PEG (Monnier *et al.*, 2014; Shirmardi Shaghasemi *et al.*, 2017).

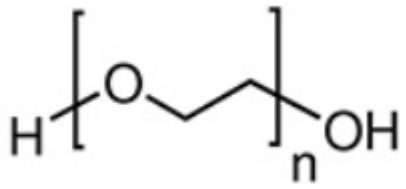

Figure 4 - Chemical structure of PEG

When grafted onto a surface, PEG chains can take on two conformations, mainly depending on the grafting density. For low grafting density, the PEG chains will acquire a "mushroom" conformation, while a "brush" conformation only occurs with higher density (Cruje and Chithrani, 2014). Since each conformation may present different susceptibility to binding with proteins and other components, the molecular percentage of PEG and respective chain length represent two parameters of extreme importance that may affect the desired function of the coating.

A plethora of studies with PEGylated magnetoliposomes were already reported, both for MRI and drug delivery. Martins *et al.* (2014) addressed MLPs for the detection of ischemia-reperfusion injuries, proving their effectiveness as negative contrast agents for MRI, as evidenced by the relaxivities obtained (Martins *et al.*, 2014). The effect of the PEG_{2000} coating was elucidated by the same group in a different paper (A. Carvalho *et al.*, 2014).

Regarding drug delivery applications, PEGylated-MLPs have found the most success against cancer cell lines. For example, A. Askari *et al.* (2020) developed a nanosystem composed of SPIONs and doxorubicin encapsulated inside PEGylated liposomes, and evaluated their theranostic potential against a MCF-7 breast cancer cell line (Askari et al. 2020).

No reports using PEGylated MLPs for biofilm eradication were found.

Chapter 3

Bacterial Membrane Mimetic Models

While it is possible to study the interaction between drugs and bacterial membranes using the bacteria itself, the complexity and diversity presented by biological membranes limits the possible potential of such approach. Besides, working directly with bacteria may require superior installations, specialized professionals and higher costs, preventing small R&D groups to perform such investigations. Regarding complexity, the challenge lies on their dynamic environment, with active and passive processes mixed together. Thus, a specific physical phenomenon is very difficult to isolate and therefore challenging to analyze (Fenz and Sengupta, 2012).

Taking into consideration both complexity and diversity, several biomimetic model membranes have been developed to overcome those barriers, allowing more specific studies at a molecular level under well-defined conditions (Hu and Tam, 2017; Li *et al.*, 2018). The strength of these membranes as first models is related to their simplicity, as an isolated lipid membrane able to individualize a specific process and lead to a well-controlled experiment (Fenz and Sengupta, 2012). Properties such as size, composition and geometry can be tailored according to the investigation planned (Chan and Boxer, 2007).

With different biomimetic systems already developed, the choice among the various options depends on the biological and physicochemical nature of the study. The most common models encompass Langmuir monolayers, supported lipid bilayers (SLB) and liposomes (Beales *et al.*, 2015; Chan and Boxer, 2007; Hu and Tam, 2017; Li *et al.*, 2018).

Langmuir monolayers are obtained on an aqueous surface after spreading amphiphilic lipids to form the monolayer, as presented in Figure 5. It allows a wider choice of conditions,

otherwise restricted in bilayers, such as lipid composition, pH and temperature, and a better regulation of lipid lateral-packing density. Typically, these monolayers are suitable for studies of drug interactions with lipid head groups (Li *et al.*, 2018), but not appropriate for transmembrane events (Afanasenkau and Offenhäusser, 2012).

SLBs were introduced in 1984 by L. K. Tamm as a mimetic model membrane system (Tamm, 1984; Tamm and McConnell, 1985) and have been extensively used since then. They can be defined as a lipid bilayer on a solid surface - built with substrates such as glass, mica, silicon, silicon dioxide, carbon nanotubes, metal/polymer-coated glass plates, and others – with an aqueous solution forming a hydration layer (≈ 1nm) between the bilayer and the surface (Afanasenkau and Offenhäusser, 2012; Li *et al.*, 2018; Peetla *et al.*, 2009). The most common methods for SLB preparation includes direct vesicle fusion, combination of Langmuir-Blodgett (LB) technique with vesicle fusion, combination of LB and Langmuir-Schäfer (LS) techniques and spin coating (Kiessling, Yang, and Tamm 2015). These bilayers, besides providing a biomimetic system, also present good stability and allow incorporation of proteins and further researches related to those molecules and can be easily integrated into biosensors (Afanasenkau and Offenhäusser, 2012). They are mainly suitable to study the phase behavior and lateral mobility of lipids, and accessible to various surface sensitive analytical studies – *e.g.* atomic force microscopy (AFM), quartz crystal microbalance with dissipation (QCM-D),

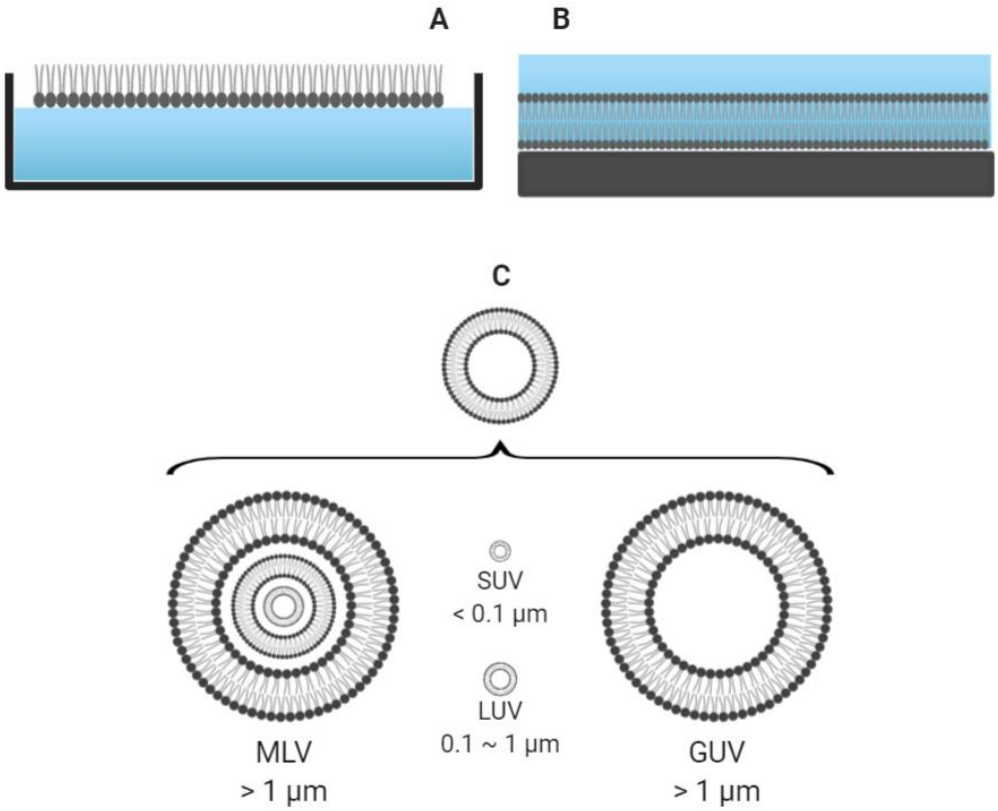

Figure 5 - Schematic representation of a Langmuir monolayer (A), a supported lipid bilayer (B) and liposomes with their different designations (C)

ellipsometry, surface proton resonance (SPR) and spectroscopic techniques (Afanasenkau and Offenhäusser, 2012; Li *et al.*, 2018). A schematic representation of a SLB is presented in Figure 5.

However, the label of the most used biomimetic system bring us back a familiar nano structure. Liposomes, vesicles relatively easy to prepare and handle, possesses an aqueous core surrounded by a phospholipidic double layer, resembling natural cell membranes. These model membranes have been widely used to study the interaction of drugs with membranes of different compositions and even establish membrane related mechanisms of action of drugs (Hu and Tam, 2017; Li *et al.*, 2018; Peetla *et al.*, 2009). Pinheiro *et al.* (2013) studied the effect of rifabutin, an antibiotic broadly used in the treatment of mycobacterial infectious diseases, on human and bacteria cell membrane models by using MLVs. For that, 1,2-dimyristoyl-*rac*-glycero-3-phosphocholine (DMPC), a zwitterionic phospholipid, was chosen as a suitable membrane model of the human cell membrane, while DMPG (a negatively charged lipid) was used as a simple bacterial membrane model. Additionally, DPPE:1,2-dipalmitoyl-sn-glycero-3-phospho-*rac*-(1-glycerol) (DPPG) with a molar ratio of 8:2 was used as a more complex composition for the bacterial cell membrane models (Pinheiro *et al.*, 2013). Matos *et al.* (2012) calculated the partition coefficient to evaluate the interaction of daunorubicin, and antitumoral drug, with LUVs as a cell membrane model, composed of egg phosphatidylcholine (EPC) (Matos, Moutinho, and Loba, 2012). Several studies already proved that liposomes present a good membrane model to estimate partition coefficients, because other methods cannot account for the ionic interactions between lipids and drug that may occur (Li *et al.*, 2018).

When mimicking bacterial membranes, it is important to remember the concept previously presented - both composition and structure need to be taken in consideration, given the differences not only between gram-positive and gram-negative bacteria, but even among species, with various phospholipids to choose from.

As of today, liposomes remain as the best membrane model system. These vesicles can be divided depending on their size and both LUVs and MLVs already demonstrated their capacity to perform as biomimetic models. However, the properties presented by the giant vesicles – GUVs - also led to an extensive research in the past decades. An overview on preparation techniques and possible applications will be provided below.

3.1. Giant Unilamellar Vesicles

In the past decade, GUVs have become a membrane model system of choice. With diameters ranging from 1μm to 100μm, these vesicles can be size-wise compared to biological membranes and observable by optical microscope techniques. These properties allow studies at the single vesicle level with a theorical flat membrane, due to the low curvature presented as a

consequence of the size. GUVs have been initially established and used as a workbench for studying basic properties of simple lipid bilayers. Nowadays, they are increasingly employed in biophysics to investigate the mechanisms driving biological processes at the level of the plasma and organelle membranes. GUVs have also become important tools to try to understand the origin of life or in application-driven research such as in drug delivery or in material synthesis where the vesicles are used as micro-compartments.

3.1.1. Background

Reeves and Dowben described "the preparation and properties of phospholipid vesicles of pre-determined composition several microns in diameter" in the late 60's, marking the first appearance of these giant vesicles, well-suited for studies focused on the lipid membrane permeability (Reeves and Dowben, 1969). However, the "giant" term only appeared a decade later, by Harbich and Helfrich (Harbich and Helfrich, 1979). From 1969 until now, GUVs have been gathering several possible applications, with different preparation methods. As a result of the properties already presented, GUV's most desirable application remains as a biomimetic membrane model system.

3.1.2. Preparation

Since their first appearance, GUVs have been prepared by various approaches. In 1969, Reeves and Dowben used a controlled (gently and slowly, at room temperature) hydration of a thin dry film of bilayer-forming EPC deposited on a glass or Teflon surface, with either an aqueous solution of non-electrolytes or pure water (Reeves and Dowben, 1969). This method – known by the name of gentle hydration or spontaneous swelling - has now many variations, aimed at improving it, as it presents itself with some limitations since GUVs only form if the hydration is performed with specific and precise conditions, such as temperature, osmotic pressure, electrostatic interactions, hydrophobic effects, among others (Dimova and Marques *et al.*, 2019). These variations can be based on the addition of charge lipids (10-20 mol%), such as phosphatidylserine (PS) or phosphatidylglycerol (PG), to improve the yield and the size of the vesicle. The electrostatic repulsions between layers derived from the charged lipids also helps the GUVs formation. However, defects can occur with higher percentages of these lipids. Moreover, vesicle swelling can be promoted by the presence of divalent ions, like Ca^{2+} and Mg^{2+} with concentrations between 1-30 mM. In contrast, the addition of sugar, like D-(-)-fructose, can improve the swelling of the lipid film, based on osmotic effects. In order to increase the control over the vesicle's diameter, it is possible to apply a patterning with photolithographic

templates. In addition to all of these parameters that can influence the formation of GUVs, other approaches such as localized heating, pressure waves and PEGilation can also be used.

Nonetheless, all the improvements, the spontaneous swelling still presents some disadvantages. Firstly, the preparation can take more than a day, leading to the degradation of lipids, if prone to oxidation. Secondly, the vesicle's quality is limited, with a majority having defects (Dimova and Marques *et al.*, 2019). Also, it can only be used for specific amphiphiles (Rideau *et al.*, 2019).

Besides spontaneous swelling, there are other solvent-free methods based on vesicle swelling on substrates.

Gel-assisted represents another preparation technique, comparable to the previous method except on the substrate, a polymer-based gel such as agarose or PVA. Here, the hydrophilic polymer is coated onto the substrate and dried, after being dissolved in water. Then, the amphiphile solution follows the same method as before: manually spread over the polymer, dried and finally the hydration chamber can be filled with the aqueous solution (Dimova and Marques *et al.*, 2019; Rideau *et al.*, 2019). However, in gel-assisted, the hydration should not last more than an hour, a significant reduction compared to the spontaneous swelling process. Besides the time of hydration, only a few other parameters can be adjusted, such as the concentration of lipids, the type of gel and spreading technique used. Yet, a significant drawback to this method is the contamination caused by both agarose and PVA, leading to several possible altered properties like fluidity, permeability and stability. Between the two polymers, agarose is the least desirable, as it easily dissolves in water and ends up incorporated into the vesicles (Weinberger *et al.*, 2013). However, T. Dao and colleagues observed a significant variation to the stretching modulus, lateral diffusion coefficient and membrane packing when producing GUVs using the PVA approach (Dao *et al.*, 2017).

Electroformation (or electroswelling) is another method based on vesicle swelling on substrates and the most widely used for GUVs formation. Developed in 1986 by Angelova and Dimitrov, this approach diverges from the traditional swelling protocol by applying an externally alternative current to the electrodes used as surfaces (Angelova and Dimitrov, 1986). Indium tin oxide (ITO) coated glass and platinum wire are the most common materials used in these conductive slides, separated one from another by a millimetric nonconductive spacer. The lipid solution, prepared in chloroform, methanol or other organic solvent, is deposited on the conductive surface and after the evaporation of the solvent, the chamber is assembled with the second electrode (Dimova and Marques *et al.*, 2019; Rideau *et al.*, 2019; Walde *et al.*, 2010). A swelling solution is also required, similar to the methods previous presented.

With the extensive use of electroformation, several protocols have been developed, with slight variations to the parameters, according to the desired characteristics. Recently, an electroformation device has been developed by Nanion Technologies, called Vesicle Prep Pro,

which has not been extensively used in scientific literature, but the number of publications is growing considerably.

Despite being reported almost 35 years ago, the electroformation mechanism which induces the self-assembly is still not fully understood. Lipid composition, volume and concentration, organic solvent, swelling solution concentration and volume, temperature, voltage, frequency and duration can be tailored, between specific values (Drabik *et al.*, 2018). Under optimal conditions, the obtained GUVs can be homogeneous. The differences between the flat glass ITO surface and the cylindrical Pt surface can also lead to variations in the adhesion of the lipids, as both have their own conductivity and are responsible for different van der Waals and electrostatic interactions (Rideau *et al.*, 2019).

Altogether, these variabilities evidence how flexible electroformation can be, presenting a method capable to form GUVs with chosen qualities with desired lipids and aqueous solution, justifying the lack of uniformity in protocols. Additionally, Rodriguez *et al.* (2005) showed by fluorescence microscopy that electroformation is associated with low defects in the vesicles formed, with 80% devoid of significant flaws while gentle hydration only grants 40% (Rodriguez *et al.*, 2005). A schematic representation of the three solvent-free methods is presented in Figure 6.

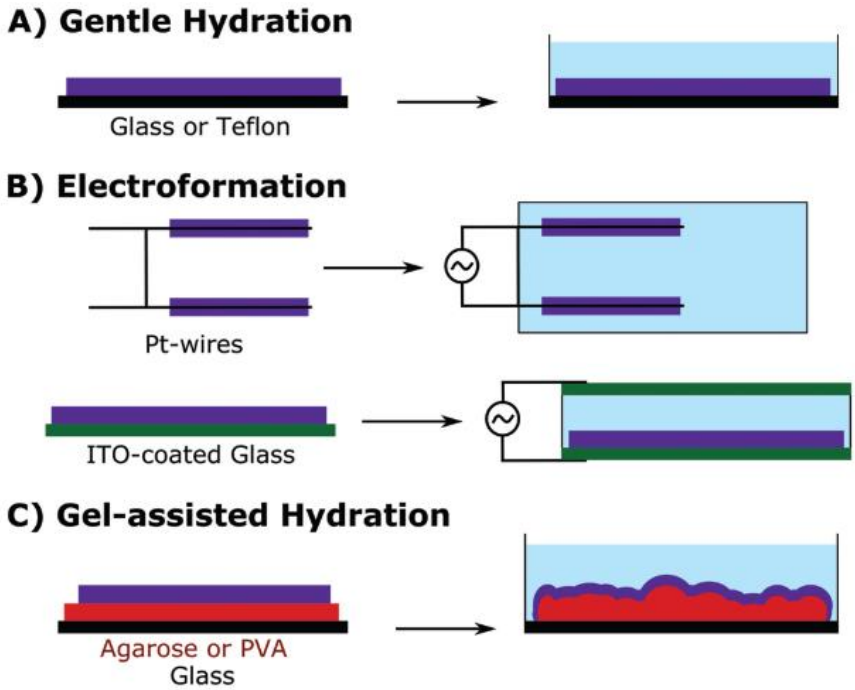

Figure 6 - Schematic representation of the three solvent free methods to prepare GUVs. Adapted from Rideau et al., 2019

Beyond the methods already addressed, there are a large variety of other possibilities based on the assembly from fluid interfaces. Approaches like the emulsion-based methods

gained recognition in the beginning of the century, while microfluidic-assisted methods (for example, the microfluidic double emulsions and the microfluidic jetting) and the continuous droplet interface crossing encapsulation (cDICE) were first described in 2011 (Beales *et al.*, 2015; Dimova and Marques *et al.*, 2019). GUVs can also be formed from an initially planar bilayer, or a micellar lipid solution, or even by the fusion of small vesicles (LUVs) (Walde *et al.*, 2010).

3.1.3. Applications

As stated before, GUVs resemble the elementary structure of all biological cells, mimicking the lipid matrix of the membrane. Therefore, they are extensively used for biomimetic chemistry, biomembrane physics and artificial cell synthesis, with numerous applications already documented (Walde *et al.*, 2010). GUVs proved to be a powerful model to study various physico-chemical properties of membrane, such as mechanical properties (Vitkova *et al.*, 2004), membrane curvature (Moreira *et al.*, 2019), fusion (Heuvingh *et al.*, 2004), budding and fission (Baumgart, Hess and Webb, 2003), growth (Peterlin *et al.*, 2009), fluidity and lipid order (Ariola *et al.*, 2009), membrane dynamics (García-Sáez and Schwille, 2008) and lipid domains visualization (Klymchenko *et al.*, 2009). Moreover, due to their cell-like size, they are increasingly used for studying protein/lipid interactions, when the protein/peptide can be reconstituted in the GUVs membrane (K. Carvalho *et al.*, 2008) or pass across the vesicle bilayer into the interior of the GUV (Shimanouchi *et al.*, 2007). Other possible application includes the examination of cytoskeletal rearrangements within a cell-like model membrane system, which represents a critical step in reconstructing the minimal machinery required for the division of an artificial cell, with GUVs playing an crucial role as cell membrane model (Merkle, Kahya and Schwille, 2008). Although mimicking the interior of cells remains a challenge, given their complexity and singularity, GUVs already found a couple of applications aimed at developing experimental models that resemble a parcel of the interior of cells. For examples, GUVs containing PEG/dextran aqueous two-phase system (ATPS) already showed their potential as synthetic cells capable of dynamic protein and nucleic acid microcompartmentation, developing an experimental model for cytoplasmic organization (Long *et al.*, 2005). Studies related to polymer-induced permeabilization (Vial *et al.*, 2009), GUVs as reaction containers (Liu *et al.*, 2007) and gene expression inside single GUVs (Saito *et al.*, 2009) have also been described, reinforcing the vast range of applications for these giant vesicles.

When using GUVs to mimic cell membranes, the molar ratio of the existing phospholipids represents a crucial factor for the development of steady vesicles. Additionally, the chosen phospholipids will regulate the final surface charge density of GUVs. Y. Tamba and M. Yamazaki (2009) investigated the interaction of Magainin 2, an antimicrobial peptide, with

GUVs of 1,2-dioleoyl-*sn*-glycero-3-phosphatidylcholine (DOPC):1,2-dioleoyl-sn-glycero-3-phosphatidylglyce-rol (DOPG) in various ratios. The obtained results showed that the concentrations of magainin 2 required to induce the same pore formation greatly increased with the decrease of DOPG concentrations, responsible for the negative net charge of the membrane (Tamba and Yamazaki, 2009).

Furthermore, using GUVs as a model membrane for different bacteria have already been reported. C. Ciobanasu *et al*. (2015) studied the interaction of an antimicrobial peptide NKCS using GUVs as a model membrane for *E. Coli* and human cells (Ciobanasu *et al*., 2015). *E. coli* is known for possessing three of the most common membrane phospholipids – PE, PG and cardiolipin (CL) – where PE is the most abundant (Sohlenkamp and Geiger, 2016). However, PE:PG GUVs could not be formed due to the existing negative charge. Rather, the group added DOPC to form stable GUVs, ending up with two formulation as approximations for bacterial membranes, using 1-palmitoyl-2-oleoyl-sn-glycero-3-phosphatidylethanolamine (POPE) and 1-palmitoyl-2-oleoyl-sn-glycero-3-phosphatidylglycerol (POPG). The molar ratio for the DOPC:POPE formulation was 60:40, whereas the formulation of DOPC:POPG was composed of a 70:30 ratio. For both formulations, NKCS proved to be an effective antimicrobial agent, contrasting with the low toxicity toward GUVs comprising DOPC as a mimic for human erythrocytes (Ciobanasu *et al*., 2015).

Mark Kreutzberger *et al*. (2017) also used GUVs as a biomimetic system for the phospholipid bilayer of bacteria, focused specifically on gram-positive bacteria such as *S. aureus* and *Enterococcus spp*. The interaction of GUVs with daptomycin, a polypeptide active against both bacteria mentioned before, was investigated. Thus, two GUVs formulations were developed, comprising 1-palmitoyl-2-oleoyl-*sn*-glycero-3-phosphatidylcholine (POPC):POPG molar ratios of 70:30 and 80:20 (Kreutzberger *et al*., 2017).

Very recently, it was reported by Mohanan *et al*. (2020) a successful attempt to bio-engineer GUVs mimicking bacterial membrane models like *S. aureus* without changing the composition found in their natural ternary mixture of charged lipids. A combination of 60% w/v (DOPG) (sodium salt), 35% w/v 1,2-dioleoyl-sn-glycero-3-[phospho-rac-(3-lysyl(1-glycerol))] (chloride salt) (lysyl PG) and 5% CL was able to form GUVs at pH 5 and pH 7, using the gel-assisted method with a PVA film (Mohanan *et al*., 2020).

Hence, GUVs offer a crucial biophysical tool, capable of a bottom-up approach, to study model membranes starting from minimal systems to more complex ones. However, the interpretation of data can sometimes present ambiguities and challenges. Hence, the properties presented by GUVs, such as a size well above the resolution limit of regular optical microscopy, come in handy, allowing a direct observation for monitoring, in real time, morphological fluctuations and chemical or enzymatic reactions either within or on the surface of a singular giant vesicle (Walde *et al*., 2010). Fluorescence microscopy techniques appear as the “gold standard” to analyse GUVs since the late 1990s, with epifluorescence, confocal and

two photon excitation fluorescence highlighted, each with several purposes already documented (Juhasz *et al.*, 2009; Montes *et al.*, 2007; Ramundo-Orlando *et al.*, 2009; Rodi, Maggio and Bagatolli, 2018). Phase contrast also provides valuable information, but combining the sensitivity and flexibility of a microscope with fluorescence spectroscopy offers the possibility to gather spatially resolved data (Bagatolli and Needham, 2014).

Other techniques can be used simultaneously with the fluorescent microscopy to increase the knowledge towards the given vesicle, such as the micropipet manipulation technique, which uses Hoffman modulation contrast optics in a regular bright field microscope. This allows studies on the mechanical, thermal, adhesive and molecular exchange properties (Bagatolli and Needham, 2014; Roux *et al.*, 2005). Another possible approach is measuring the zeta potential, to exclude possible artefacts resulting from the fluorescent probe or other additional components in the membrane (Steinkühler *et al.*, 2018).

The proposed work wraps the fusogenic and anti-bacterial potential of MLPs for bacterial biofilm disruption, namely *S. aureus*, using GUVs as a biomimetic model membrane. Here, the membrane fusion holds a fundamental role for the successful delivery of SPIONs into the interior of the model membrane. Lira *et al.* (2019) studied the fusion between fusogenic LUVs positively charged and GUVs composed of different molar ration of POPC:POPG. In order to quantify the fusion efficiency, a FRET assay was used, evaluating the intensity of the acceptor dye – 1,2-dioleoyl-*sn*-glycero-3-phosphoethanolamine -N-(lissamine rhodamine B sulfonyl) (DOPE-Rho) – present in the LUV and the donor dye – 1,2-dipalmitoyl-sn-glycero-3-phosphoethanolamine-N-(7-nitro-2-1,3-benzoxadiazol-4-yl) (DPPE-NBD) – in the GUV upon fusion (Lira *et al.*, 2019). A similar approach will be conducted in this work, using MLPs instead of cationic LUVs. Moreover, *S. aureus* is known for its vast antibiotic resistance and an alternative is required. Thus, the work here presented will focus on several levels: starting from the design and optimization of both liposomal formulations - GUVs with a small percentage of POPG as an initial approach for mimicking *S. aureus* membrane; and PEGylated MLPs with antibacterial activity as a potential alternative to antibiotics – leading to the evaluation of the fusogenic capacity of MLPs, using the FRET technique, with the obtained optimized model.

Chapter 4

Materials and Methods

The applied methods for this work will be mentioned in this section, split between three main phases. All the work around magnetoliposomes is described firstly, starting with the synthesis of SPIONs and magnetoliposomes. After, some characterization measures were performed, and the optimized formulation was obtained by a Box-Behnken experimental design. A membrane fusion with the FRET assay was carried out using the optimized formulation and DMPG LUVs. In a second phase, GUVs were prepared with the Vesicle Prep Pro device and observed in a fluorescence microscope. Finally, the membrane fusion assay with the magnetoliposomes and GUVs mimicking *S. aureus* (to some extent) was evaluated.

4.1. Materials

In the table below, all the reagents used for the entirety of the work are listed, accompanied by the respective brand and purity when known.

Table 1 - List of the reagents used, followed by their purity and brand

Reagents	*Purity*	*Brand*
DOPE	≥97%	Sigma-Aldrich ®
DPPC	-	Avanti ® Polar Lipids, Inc.
CHEMS	-	Sigma-Aldrich ®
DMPG	≥97%	Sigma-Aldrich ®
DOPC	-	Avanti ® Polar Lipids, Inc.
POPG	-	Avanti ® Polar Lipids, Inc.
DPPE:N-(7-nitro-2-1,3-benzoxadiazol-4-yl)	-	Avanti ® Polar Lipids, Inc.
DSPE:N-(7-nitro-2-1,3-benzoxadiazol-4-yl)	-	Avanti ® Polar Lipids, Inc.
DOPE:N-(lissamine rhodamine B sulfonyl)	-	Avanti ® Polar Lipids, Inc.
16:0 PEG 2000	-	Avanti ® Polar Lipids, Inc.
PBS buffer	-	Sigma-Aldrich ®
D-Sorbitol	≥98%	Sigma-Aldrich ®
Chloroform	stabilised with 0.6% ethanol	VWR Chemicals
Methanol	≥99.9%	Fisher Chemical
Iron(II) chrolide tetra-hydrate	≥99%	Sigma-Aldrich ®
Iron(III) chloride hexa-hydrate	97%	Sigma-Aldrich ®
Ammonium hydroxide	-	Fisher Chemical
1,10-Phenanthroline hydrate	≥99%	Fisher Chemical
Hydroxylamine hydrochloride	99%	Sigma-Aldrich ®
Hydrochloric acid	-	Fisher Chemical
Sephadex® G-25	-	Sigma-Aldrich ®

Phase 1 – Preparation and Optimization of Magnetoliposomes

4.2. SPIONs Synthesis

To prepare SPIONs, a microwave-assisted technique was used. Compared with the traditional synthesis methods, this protocol presents several advantages, such as more reproducibility and the use of small amounts of reagents. Combining a short reaction time, reasonable

temperatures and high yield (≈80%), crystallinity and monodispersity elevates the quality of the obtained SPIONs (Gonzalez-Moragas *et al.*, 2015).

Based in previously protocols from the group, 250 mg of ferric chloride hexahydrate ($FeCl_3 \cdot 6H_2O$) and 138 mg of ferrous chloride tetrahydrate ($FeCl_2 \cdot 4H_2O$) were dissolved in a glass vessel with the addition of 20 mL of double distilled water, assisted by a magnetic stirring. The obtained formulation had an orange coloration. Next, 3 mL of a 25% ammonium hydroxide (NH4OH) were carefully added to the solution, changing the colour to black. This step required a drop-wise addition inside a closed hotte. The glass vessel was then removed from the stirring and placed in the microwave device, with the following parameters:

- Temperature: 100ºC
- Time: 10 minutes
- Maximum Wattage: 300 W
- Maximum Pressure: 200 psi
- Stirring: Maximum

The procedure lasted for 10 minutes after reaching the desired temperature, removing the glass vessel at that time. Back again in a closed hotte, the solution was transferred to a 50 mL Falcon tube and water was added as desirable, around 20mL. A strong magnet was placed underneath, trapping the SPIONs to the bottom of the Falcon. Then, the supernatant was removed by holding the Falcon and the strong magnet together, pouring the liquid content down. Water was then added again, and the process repeated at least two more times, with less volume each time. Finally, the SPIONs were resuspended in 25mL of water and stored at 4ºC.

4.3. Preparation of Magnetoliposomes

To prepare MLPs, the thin hydration technique was applied, reproducing the protocol presented by Filipa Soares in her master's thesis (Filipa Soares, 2019). The lipid composition chosen was DOPE:DPPC:CHEMS (4:2:4), given the enhanced fusogenic ability already presented by such formulation (Forier *et al.*, 2014; Nicolosi *et al.*, 2010). In addition, 5% of 16:0 PEG2000 PE was also added.

In the first place, lipids were weighted in eppendorfs according to the desired concentration and stored at -20ºC if necessary. A certain volume of SPIONs was pipetted to an eppendorf and a small magnet was placed with glue on the wall, pulling the SPIONs close to it.

After some time, the water was removed and a nitrogen stream was used to dry the SPIONs. Then, both lipids and SPIONs were dissolved in chloroform/methanol (3:1) and transferred to a glass vessel. To fully remove the organic solvent, the solution was placed on a rotary evaporation under a nitrogen stream for approximately 30 min, with the water bath set at 45ºC. Additionally, the glass vessel was placed 1h on vacuum environment and stored at -20ºC until the hydration.

The hydration was carried out by adding 4 mL of PBS buffer to the glass vessel, using the vortex to obtain a homogenised formulation of MLVs. For the size reduction, 2 mL were then placed on a ultrasonication device, varying the time accordingly with the pretended conditions. However, to separate SPIONs that fail to be encapsulated from the remaining SPIONs-encapsulated LPs, an additional step was required, via a size-exclusion chromatography. Thus, 1mL of the formulation was placed in a Sephadex column and 6 mL of MLPs were collected in the end of the run through the column. To prepare fusogenic liposomes without SPIONs, the thin hydration method was completed after the sonication step.

4.4. Characterization of Magnetoliposomes

4.4.1. Particle Size and Polidispersity Index

To measure the hydrodynamic diameter and polidispersity, the well-established dynamic light scattering was used (DLS). This technique allows the measuring of the average size and its distribution across the particles in a suspension, requiring low concentrations. Not only it provides a fast method to obtain these parameters, but also presents a non-destructive protocol. DLS settles on the scattering of light by the particles in the suspension, causing fluctuations in the intensity that reaches the detector. The intensity shifts as time progresses, related to the ongoing Brownian processes in the sample (Pinheiro *et al.*, 2013), where small particles diffuse more quickly resulting in fast fluctuations over time, contrasting with the slower fluctuations of large particles that extend the correlation of the signal. Then, the DLS device extracts the translation diffusion coefficient and uses the Stokes-Einstein equation to obtain the hydrodynamic size (Stetefeld *et al.*, 2016).

The polidispersity index (PDI) is a dimensionless value extracted from the square of the division between the standard deviation and the mean diameter of the particles. The threshold typically associated with monodisperse suspensions is 0.2; higher values reflect polydisperse suspensions.

Here, a Nanobrook ZetaPALS (Zeta Potential Analyser Instruments) was used, with 6 runs of 2 minutes for each sample, at 20ºC. The program returns the values for each run as well as the mean values.

4.4.2. Determination of Lipids Phase Transition Temperature

With DLS, it is also possible to determine the main phase transition temperature of lipids. The several modifications occurring at the transition temperature, change the lateral diffusion, bilayer thickness, permeability and so on, which can be correlated with the mean count rate. A discontinuity of this value is associated with changes in the optical properties of the colloidal solution, increasing upon state transitions (Michel *et al.*, 2006). The results were plotted as "mean count rate vs temperature" and the data could be fitted to sigmoid curves. The following equation (Neves *et al.*, 2016) was used:

$$r_S = r_{S_1} + p_1 T \frac{r_{S_2} - r_{S_1} + p_2 T - p_1 T}{1 + 10^{B\left(\frac{1}{T} - \frac{1}{T_M}\right)}} \quad (\mathbf{1})$$

In this equation, T is the absolute temperature, r_{S_1} and r_{S_2} are the interception values at the y axis, p_1 and p_2 correspond to the slopes at the start and the end of the plot, B is the cooperativity and T_M the midpoint of phase transition.

Thus, the T_M was calculated for two formulations: MLPs with the optimal formulation regarding lipid concentration, sonication time and SPIONs volume and empty LPs with the same formulation. 3 mL were added to the cuvette (50 µL of formulation in PBS) and 43 measurements were performed in the automatic mode, starting at 8ºC all the way up to 50ºC, with 2 runs of 1 minute for each temperature and 3 minutes for temperature stabilization between runs.

4.4.3. Evaluation of Encapsulation Efficiency

When developing MLPs, it is relevant to study the encapsulation efficiency (%EE) of SPIONs, a measure of the amount of these magnetic nanoparticles inside the liposomes compared to the amount initially added. For that, a colorimetric assay was used, addressing the iron content (Fe^{2+}) inside the formulations.

After the size-exclusion chromatography, 100 µL of the formulation diluted in 100 µL of double distilled water were digested with 200 µL of 1M HCl during 2h at 60ºC. Then, after

reaching room temperature, 400 µL of a 10% hydroxylamine hydrochloride solution ($NH_2OH{\cdot}HCl$) were added. This redundant agent allows the reduction of Fe^{3+}, the most common iron ion in SPIONs, into Fe^{2+}. After 15 min, 400 µL of a 0,25% 1,10-phenanthroline solution was added. Phenanthroline combined with Fe^{2+} leads to the formation of a complex and stable ion, characterized by a strong orange coloration that absorbs in the UV-Vis spectrum, with the maximum absorbance around 511 nm. The following day, 800 µL of double distilled water were added, to reach a volume of 2 mL, before the centrifugation at 14 000 rpm during 20 min. It was noticeable a lipid pellet in the bottom of the eppendorf. The same protocol was applied to SPIONs with dilutions of 128x and 256x, using 200 µL of solution instead of the 100 µL plus water used for magnetoliposomes.

The iron concentration was calculated at 511 nm, through a calibration curve previously obtained in the group (Equation 2). After applying the dilution factor for each formulation, the %EE was estimated using the Equation 3.

$$Abs = (0{,}2071 \pm 0{,}0052) \times [Fe](ppm) + (0{,}0096 \pm 0{,}0233) \quad (\mathbf{2})$$

$$\%EE = \frac{[Fe^{2+}]_{MLPs}}{[Fe^{2+}]_{SPIONs}} \times 100 \quad (\mathbf{3})$$

4.5. Determination of PEG Percentage

To assess the suitable percentage of PEG, a small assay was performed with 4 formulations, composed of DOPE:DPPC:CHEMS (4:2:4). Here, the three factors (lipid composition, SPIONs volume and sonication time) chosen were obtain previously with a Box-Behnken protocol without PEG, developed by Filipa Soares (Filipa Soares 2019) - 15 mM, 0,5 mL and 0,5 minutes. To maintain the 4:2:4 ratio, the quantity added for 16:0 PEG2000 PE with different percentages – 0,5%, 2% and 5% - was subtracted to the DOPE mass. The four formulations were then prepared with the protocol already addressed and characterized, with the iron quantification performed three times, with approximately 2 hours between experiments.

4.6. Optimization of the Formulation Preparation Protocol

The optimized formulation was obtained using a design of experiments (DOE) with a three-factor and three-level Box-Behnken statistical protocol. With this design, it is possible to predict the considered independent variables applying a set of 15 experimental runs,

fluctuating the design points of the three dependent variables between a low and a high factor and their midpoints. The number of runs was obtained with the equation below,

$$N = 2k \times (k - 1) + C_0 \quad (\mathbf{4})$$

where k is the number of factor and C_0 the number of central points. Therefore, for a three-factor experiment, 12 unique experiments are required, plus three replicates at the centre point.

The main advantages of a Box-Behnken design are the number of simultaneous factors that can be studied while using a small number of experiments that avoid combinations with all factor set for the lowest and highest value - therefore dodging possible extreme conditions (Ferreira *et al.*, 2007).

From previously assays performed in the group, the chosen factors were the lipid concentration, the volume of SPIONs and the sonication time. A new variable was introduced in this work – the percentage of PEG, for which a preliminary evaluation was performed with the purpose of keeping the three-factors experiment, setting the same percentage for every formulation. The three dependent variables were the mean size of the NPs, the polidispersity index and the encapsulation efficiency. However, after analysing the results from the DLS, two different populations were found: a smaller population, generally below 100 nm but representing 95% of the total nanoparticles, and a larger population superior to 200 nm in the majority of the runs. Thus, it was necessary to split the mean size into two different dependent variables - a representative population and a minority population.

The three-level of variables and the 15 experimental runs generated are presented in Table 2. The results were analysed with the Minitab® software, extracting the response surface regression for each variable, as well as the response surface plots. For the optimized formulation, the goal for each parameter could be set for a certain minimum, maximum or a specific target. Here, the polidispersity index was set for the minimum, while the values for both populations were set for a specific value - 100 nm. The goal was to close the gap between them, although it was certain that the minority population was not going to drop even close to that mark. Thus, the target mean size chosen was 175 nm. With these values set as the most desirable, the software applies the geometric mean to calculate the desirability function, aimed at maximizing it, and the associated 95% confidence interval (CI) and 95% prediction interval (PI) (Ferreira *et al.*, 2007).

Then, three replications of the optimized formulation were prepared and characterized, comparing the results with the predictions given by the software.

Table 2 - Considered factors and experimental runs for the Box-Behnken design

Factors	**Low (-1)**	**Midpoint (0)**	**High (+1)**
Lipid Concentration (mM)	10	20	30
SPIONs Volume (mL)	0.5	1.0	1.5
Sonication Time (min)	0.5	1.5	2.5
Experimental Runs	**Lipid Concentration (mM)**	**SPIONs Volume (mL)**	**Sonication Time (min)**
R1	10	0.5	1.5
R2	30	0.5	1.5
R3	10	1.5	1.5
R4	30	1.5	1.5
R5	10	1.0	0.5
R6	30	1.0	0.5
R7	10	1.0	2.5
R8	30	1.0	2.5
R9	20	0.5	0.5
R10	20	1.5	0.5
R11	20	0.5	2.5
R12	20	1.5	2.5
R13	20	1.0	1.5
R14	20	1.0	1.5
R15	20	1.0	1.5

Phase 2 – Preparation and Visualization of GUVs

4.7. Electroformation using Vesicle Prep Pro

While being on the market since 2006, this device from Nanion Technologies only recently gained a considerable attention throughout the scientific community, with the number of publications rising since 2014. It was the first developed device for automated preparation of GUVs, thought an electroformation procedure. The main advantages of such apparatus, accordingly to the company, are the simplicity offered by the automatization and the production of stable and reproducible GUVs, with homogenous size (between 1-30µm). Moreover, it includes adjustable parameters like temperature, amplitude and frequency. To develop the protocol used in this work, several articles were taken into consideration. For example, Klaerke and colleagues (2018) added 20 µL from a 5 mM lipid solution of 1,2-diphytanoyl-sn-glycero-3-phosphocholine (DPhPc) in chloroform into the conductive side of one

of the indium titanium oxide (ITO) slides (after some seconds, the solvent should evaporate completely). After placing an O-ring around the dry lipid film, the authors added 275 µL of a 350 mM D-Sorbitol solution inside the ring, closing the chamber with the other ITO slide afterwards. The parameters used for the electroformation were a peak-to-peak voltage of 6V and a frequency of 5Hz, for 2 hours at 36ºC (Klaerke *et al.*, 2018).

Also in 2018, Zehra Kahveci prepared a different protocol with some similarities. Starting with a lipid solution of DOPC (or the phospholipid of interest) in chloroform with 10 mM as the final concentration (with or without fluorescence), only 10 µL were placed in the ITO slide. Here, the ITO slide was left on a vacuum dessicator for 15 min, before applying the O-ring and 280 µL of a 195 mM sucrose solution. The electroformation process proposed by the author presented 3 steps: the initial rising, where the applied voltage increases from 0 to 3V during 5 minutes; then, 2 hours with that same voltage; at last, the voltage decreases to 0 during 5 minutes (Kahveci and Pagliara, 2018). Throughout the GUVs formation, the temperature was set at 37ºC and the frequency at 5 Hz, similar to the previous article. The electroformation parameters used by these authors can be defined as the base protocol, which is already implemented in the device. The main features of several other electroformation protocols using Vesicle Prep Pro are presented in Table 3.

Table 3 - Parameters of Electroformation Protocols for the development of GUVs

Reference	**Lipid Stock Solutions**	**Volume (µL)**	**Rehydration Solution**	**Protocol Conditions**			
				Temperature (ºC)	*Voltage (V)*	*Frequency (Hz)*	*Time (h)*
(Bartelds *et al.* 2017)	5 mM DPPC:DOPC:Chol (4:3:3)	15	Water	50	1.1	10	1
(Barthmes *et al.* 2016)	10 mM DPhPC:Chol (10:1)	20	1 M Sorbitol	37	3	5	2
(Bhat *et al.* 2018)	6 mM DMPC	20	210 mM Sorbitol	36	2.5	5	2
(Boyd and Kamat, 2018)	5 mM DOPC	40	285 mM Sucrose	36	3	5	2
(Magnani *et al.* 2018)	1mM PEO-PBD:DPPC	5	240 mM Sucrose	50	1.5	10	1
(Oglęcka *et al.* 2014)	POPC:SM:Chol (1:1:1)	60	Various Sugar Solutions	45	3	5	2
(Ostroumova *et al.* 2014)	11 mM DOPC:DMPC (1:1) 11 mM DOPC:DPPC (1:1) 11 mM DOPC:SM (4:1)	18	500 mM Sorbitol	25	3	10	1
(Soranzo *et al.* 2016)	10 mM DPhPC:Chol (9:1)	*not referred*	1 M Sorbitol	36	3	5	2

4.8. GUVs Formation

As the first step to develop GUVs mimicking the membrane of *S. aureus*, the lipids chosen here were DOPC and POPG. Due to the negative charge of POPG, a certain amount of DOPC was added to form stable GUVs, where a DOPC:POPG 7:3 ratio was defined, as already documented by Ciobanasu and co-workers (Ciobanasu *et al.*, 2015).

To prepare 1 mL of a 10 mM lipid stock solution, 5.5 mg of DOPC, 2.31 mg of POPG and 0.174 mg of DPPE-NBD were weighed in eppendorfs. The labeled lipid, with a 0.2 molar percentage, allowed the direct observation with fluorescence microscopy. The lipid solution, shown in the image below, was then prepared by dissolving the powders in chloroform:methanol (9:1) and stored on a glass container at -20ºC, covered from light.

Figure 7 - Photo taken to one of the old lipid solutions prepared

For the GUVs formation, the lipids were left at least 30 minutes before opening the vial, allowing them to come to room temperature. In the meantime, the conductive side of both ITO-slides was identified using a multimeter – with values below 100 Ω confirming their good state – and placing one of them in the Vesicle Prep Pro chamber, facing upwards. Next, 20 µL of the lipid solution were slowly added to the slide, creating a thin lipid layer. One minute later, the solvent should have evaporated completely, resulting in a dry lipid film. An 18 mm diameter O-ring, supplied with the device, was placed around the lipid film, with the support of a grease also supplied by the company. Then, 280 µL of an aqueous 900 mM D-sorbitol solution was added inside the O-ring and the chamber closed by placing the second slide facing downwards with the help of a tweezers.

With the preparation completed, the Vesicle Prep Pro device was turned on and the formation process could begin. The chosen parameters were very similar to the base protocol:

Temperature: **37ºC** *Frequency*: **5 Hz**

1. *Temperature establishment*
   5 min

2. *Rise*: applied voltage from 0 to 3 V
   5 min

3. *Electroformation*: alternating voltage of 3 V (+3 V and -3 V peaks)
   120 min

4. *Fall*: applied voltage from 3 to 0 V
   5 min

The electroformation parameters were recorded on the computer and stored inside the device for the following experiments.

After the electroformation, the chamber was disassembled and the GUVs were removed carefully with a micropipette with a large-tip diameter, performing up and down movements before dropping the vesicles to an eppendorf. Then, 560 µL of the same D-sorbitol solution was added, obtaining a 1:3 dilution (approximately, since the volume removed from the chamber was always inferior to the 280 µL added). The GUVs were then stored at 4ºC.

In addition to this protocol, other conditions were also tested, as an attempt to improve the results obtained after observation. Regarding the concentrations, a 5 mM lipid solution was also tested, while for the D-sorbitol solution two other concentrations were prepared: 350 mM and 650 mM. Regarding the organic solvent, a chloroform:diethyl ether:methanol (4:5:1) solution was also tried. Lastly, the impact of leaving the ITO slide with the thin lipid layer into a vacuum dessicator up to an hour was also verified.

4.9. Fluorescence Microscopy

The images were then acquired in an inverted Eclipse Ts2R-FL (Nikon) equipped with a Retiga R1 camera and a S Plan Fluor ELWD 40x DIC N1 objective. The results were analysed with the imaging software paired with the microscope (NIS-Elements Viewer) and with Fiji (which updated the architecture of ImageJ) (Schindelin *et al.*, 2012). For qualitative parameters, the NIS-Elements Viewer was used and the images will be found in the results and discussion section, as well as in the supplementary information. For quantitative parameters, the Fiji's Measure from the Analyse tab was used.

Phase 3 – Membrane Fusion Evaluation

4.10. Preliminary Fusion Assay with GUVs

A preliminary fusion assay was performed between the GUVs and the MLPs. Here, 100 µL of GUVs solution were mixed with 25 µL of MLPs, both with the fluorescence donor and acceptor, respectively. The mixture was left for 30 minutes at room temperature and protected from light before imaging in the confocal microscope already referred.

Additionally, the same protocol was repeated after exchanging the PBS of MLPs to Sorbitol with an Amicon® Ultra 0.5 mL centrifugal filter. Following a 5 min centrifugation at 3900rpm with PBS to clean the filter, 400 µL of MLPs were added to the tube and four centrifugations were performed (2000rpm for 5 min, 2500rpm for 7 min, 3500 rpm for 5 min and 3500rpm for 5 min). The filter was inverted to a new Falcon and centrifuged 5 min at 4500rpm, to remove the MLPs with a residual quantity of PBS from the filter. 400 µL of sorbitol solution were then added and the fusion protocol performed.

4.11. FRET Assay with LUVs

Here, MLPs with the optimized composition and a 0,06% mol percentage of DOPE-Rhodamine were fused with LUVs composed of DMPG labelled with DPPE-NBD. To prepare the optimized formulation, the previous protocol was repeated, with the slight addition of DOPE-Rho to the lipid composition. In the end, the same 6 mL were obtained from the column resulting in a final concentration of 5 mM, which was further diluted to 2.5 mM for the FRET assay.

To prepare the LUVs, the DMPG and DPPE-NBD (0.5% mol) were weighted for a concentration of 5.25 mM (and a hydration volume of 4 mL) and stored at -20ºC if not used in the following moments. Then, both were dissolved in chloroform/methanol (3:1), transferred to a glass vessel and placed on the rotary evaporation followed by a vacuum environment, with the same parameters as the MLPs.

The hydration step was also similar, leading to a 4 mL formulation of MLVs. Then, LUVs with homogeneous sizes were prepared by extrusion through a 200-nm Whatman® polycarbonate membrane, 10 times at 45ºC. PBS was also passed through the filter, 3 times before and after the formulation. Then, 3 mL of the formulation were diluted with 3 mL of PBS, ending up with 6 mL of a 2,625 mM LUV formulation.

For the FRET assay, increasing volumes of MLPs were added to a fixed volume of LUVs (Table 4), followed by an incubation period of 15 minutes at 37ºC. To measure the FRET efficiency, a Jasco FP-6500 Spectrofluorometer was used, with a bath set at 39ºC. Initially, the

emission and excitation spectrums of NBD were obtained. For the emission spectrum, the reading was performed between 500 and 700 nm, with an excitation wavelength of 460 nm. Here, the voltage was optimized. For the excitation spectrum, an emission wavelength of 542 nm was used and the spectrum between 300 and 500 nm was obtained.

The remaining samples were then read, from the lowest to the highest concentration of Rho. Additionally, the absorbance spectrum of rhodamine from 250 to 700 nm was also obtained, using 1 mL of PBS and increasing volumes of rhodamine for an optimal spectrum.

The LUVs and MLPs size before fusion were measured in the DLS, as well as the size of the sample with the maximum value of FRET efficiency.

Table 4 - Samples preparation for FRET assay

Samples	[DMPG:NBD] (mM)	Volume (µL)	Volume DMPG:NBD (µL)	Volume MLP:Rho (µL)	Volume PBS (µL)	[MLP:Rho] (mM)
Emission_NBD	1.3	1000	495.24	0	504.76	0
Rho_1	1.3	1000	495.24	20	484.76	0.05
Rho_2	1.3	1000	495.24	40	464.76	0.10
Rho_3	1.3	1000	495.24	60	444.76	0.15
Rho_4	1.3	1000	495.24	80	424.76	0.20
Rho_5	1.3	1000	495.24	100	404.76	0.25
Rho_6	1.3	1000	495.24	120	384.76	0.30
Rho_7	1.3	1000	495.24	140	364.76	0.35
Rho_8	1.3	1000	495.24	160	344.76	0.40
Rho_9	1.3	1000	495.24	180	324.76	0.45
Rho_10	1.3	1000	495.24	200	304.76	0.50
Rho_11	1.3	1000	495.24	220	284.76	0.55

Lastly, two FRET assays were performed with fluorescence donors with different lipidic environment: the standard DPPE-NBD and a 18:0 NBD PE, also known as [1,2-distearoyl-sn-glycero-3-phosphoethanolamine-N-(7-nitro-2-1,3-benzoxadiazol-4-yl)(DSPE)]-NBD, addressing the impact that the stiffness of the membrane domain could had on the fusion.

Chapter 5

Results and Discussion

5.1. Determination of PEG Percentage

The four formulations were prepared, without and with three different percentages of PEG - 0.5%, 2% and 5% - and characterized regarding the mean size, polidispersity and the encapsulation efficiency. For this last parameter, three replicates were performed for each formulation. The results are presented below in Table 5, while an example of the absorbance graphic obtained and respective iron quantifications are presented in the Supplementary Information. Between the three measurements (*A1, A2* and *A3*), time periods of 2h were added.

Table 5 - Impact of different PEG percentages on mean size, PDI and %EE

Characterization		**0,5% PEG**	**2% PEG**	**5% PEG**	**Without PEG**
Mean Size (nm)		234.7	226.5	148.7	214.3
Polidispersity Index		0.255	0.226	0.180	0.272
%EE	*A1*	61.3	66.3	81.2	86.7
	A2	61.5	62.3	75.9	80.5
	A3	63.4	63.1	77.1	82.0

Comparing the three formulation with PEG, it is possible to observe a decreasing tendency for the mean size and polidispersity as a consequence of the increasing percentage of PEG. The presence of a surface functionalization provides additional stability and homogeneity for the formulation, reducing the size differences between the two populations obtained. Although presenting an encapsulation efficiency higher than 80%, the formulation without PEG presented a polidispersity index of 0.272, significantly worse compared with the formulation with 5% PEG.

Thus, the formulation with 5% PEG was defined as the best formulation within the three with PEG in the composition, and the one used for the remaining work, presenting better properties for the three parameters evaluated. This sort of PEGylation, i.e. 5% molar ratio of PEG with 2kDa, was already extensively used with MLPs as MRI contrast agent (Bulte *et al.*, 1999; A. Carvalho *et al.*, 2014) and nanocarrier for drug delivery (Cardoso *et al.*, 2018).

Even though adding 5% PEG improved the overall properties of the MLPs, it is relevant to consider a future work addressing different PEG molecular weight (MW). It is possible to design both mushroom and brush conformations by changing the MW and the molar ratio, applying the concept of Flory radius (R_F). Referring to the radius that a PEG polymer may occupy, it can be calculated as $R_F = an^{0,6}$, where a is length of one monomer and n the number of monomers per chain. The conformation can then be predicted, dividing R_F by the distance (D) between chains (strongly dependent on the molar ratio), with the mushroom state characterized with $R_F/D \leq 1$, while values superior to 1 referring to the brush state (Suk *et al.*, 2016). For 16:0 PEG2000, the monomer length is 0.35 nm whereas the chain present 46 monomers (Garbuzenko *et al.*, 2005), resulting in a $R_F = 3.5\,nm$. Thus, for a NP with 150 nm (radius of 75 nm) and a surface area of around 70 000 nm^2, if the PEG molecules were to take on the brush configuration (1 PEG molecule per 12.25 nm^2, which is the square of 3.5 nm), it would require at least 5770 PEG molecules per nanoparticle. However, the increasing relevance of PEG already lead to several studies around such coating and therefore it was already reported that, for a 5% molar ratio, the PEG molecules develop a brush conformation (Arleth and Vermehren, 2010).

Moreover, the "stealth" qualities of the formulation also need to be confirmed.

5.2. Box-Behnken Experimental Design

With the chosen PEGylation, a 3-factor with 3-level Box-Behnken experimental design was developed as the approach to optimize the formulation. For this, the Minitab® software was used, performing the 15 suggested experiments, with the results presented in the Table 6 below.

The responses for the mean size, representative and minority population, polidispersity index and encapsulation efficiency were obtained for each experimental run. The %EE was calculated as before and the absorbance results can be found in the Table SI.2. All the responses presented significant disparities, with the mean size ranging from 127.8 nm to 362.2 nm, the PDI from 0.165 to 0.299 and the %EE from 54.0 up to 99.1. An important consideration is that both representative and minority populations were heterogeneous, with the size presented as the most representative for each population. In fact, the names "representative" and "minority" were given based on the full experimental results, with the majority of the runs having percentages superior to 97% for the representative population. However, some exceptions were obtained, namely the runs 7 and 10. The run 7 presents a mean size superior to both populations, as a consequence of two factors: first, a reduced percentage of the smallest population was observed, with only 32%; secondly, the remaining 68% of the nanoparticles in the sample were distributed from 348 nm up to 884 nm, with the majority close to 348 nm. In the Table SI.3 it is presented all the percentages for the theoretically representative population.

Table 6 - Box-Behnken experimental results

Experimental Runs	*[Lipid] (mM)*	*SPIONs Volume (mL)*	*Sonication Time (min)*	Mean Size (nm)	Representative Population (nm)	Minority Population (nm)	Polidispersity Index	%EE
R1	10	0.5	1.5	176.9	72.2	269.1	0.230	58.5
R2	30	0.5	1.5	141.0	62.4	188.0	0.169	79.8
R3	10	1.5	1.5	356.2	102.9	450.0	0.230	83.3
R4	30	1.5	1.5	191.8	72.9	261.1	0.203	68.5
R5	10	1.0	0.5	180.1	61.7	231.8	0.193	69.7
R6	30	1.0	0.5	162.3	59.0	205.4	0.165	76.1
R7	10	1.0	2.5	362.2	78.2	348.0	0.288	80.2
R8	30	1.0	2.5	165.9	77.1	257.4	0.220	67.9
R9	20	0.5	0.5	144.2	59.2	200.0	0.190	99.1
R10	20	1.5	0.5	213.0	115.7	357.0	0.205	81.2
R11	20	0.5	2.5	150.0	57.0	204.1	0.196	54.0
R12	20	1.5	2.5	292.8	108.4	494.1	0.299	74.2
R13	20	1.0	1.5	127.8	69.9	193.4	0.191	87.7
R14	20	1.0	1.5	181.7	73.7	269.9	0.213	85.8
R15	20	1.0	1.5	187.1	73.7	343.2	0.217	88.8

The data was then analysed, obtaining several response surface regression models and surface plots before proceeding for the optimization. Minitab® software performed a stepwise regression to find the best suitable quadratic regression model, using 0.15 as the alpha to enter

and remove. The stepwise method combines the other two methods – forward selection and backward elimination – by starting with an empty model and then adding a term in each step if the p-value remains below the alpha to enter. However, contrarily to the forward selection method, after adding a term, it can be later removed if the p-value of that term becomes greater than the alpha to remove, as a consequence of the addition of another suitable term. Thus, the program stops when all variables already in the model present p-values below the alpha to enter and all variables not in the model present p-values superior to the alpha to remove. As an example, the main results for the mean size are presented here, while the remaining responses can be found in the supplementary information (Figure SI.2). In Figure 8 on the left, it is possible to observe whether the association between the terms and the response is statistically significant, with two major results being the p-value for the model and the p-value for lack-of-fit, while on the right the R^2 value is presented, indicating how well the model fits the data for the mean size. To calculate the R^2, the software determines the ratio of the error sum of squares to the total sum of squares. Therefore, R^2 can be defined as the percentage of variation that the model can explain. Complementing the R^2, both adjusted R^2 and predicted R^2 are also presented. The first can be used to compare models with different number of terms, whereas the second can determine how good the predictive ability of the model is for new observations.

Source	DF	Adj SS	Adj MS	F-Value	P-Value
Model	6	70928	11821,3	13,75	0,001
Linear	3	55054	18351,2	21,35	0,000
Lipid Concentration (mM)	1	21466	21465,9	24,97	0,001
SPIONs Volume (mL)	1	24387	24387,4	28,37	0,001
Sonication Time (min)	1	9200	9200,5	10,70	0,011
Square	1	3780	3780,4	4,40	0,069
Lipid Concentration (mM)*Lipid Concentration (mM)	1	3780	3780,4	4,40	0,069
2-Way Interaction	2	12094	6046,8	7,03	0,017
Lipid Concentration (mM)*SPIONs Volume (mL)	1	4128	4128,1	4,80	0,060
Lipid Concentration (mM)*Sonication Time (min)	1	7966	7965,6	9,27	0,016
Error	8	6878	859,7		
Lack-of-Fit	6	4727	787,9	0,73	0,675
Pure Error	2	2150	1075,1		
Total	14	77805			

R-sq	R-sq(adj)	R-sq(pred)
91,16%	84,53%	77,97%

Figure 8 – Statistical impact of each term in the mean value, with the R^2 on the right.

For the mean size, there is a statistically significant association between the three linear terms and the response, while the same cannot be concluded for the square term of the lipid concentration and the 2-way interaction term of lipid concentration combined with the SPIONs volume, presenting p-values greater than 0.05. Thus, the linear terms have more significance to the response, compared to the remaining. For the remaining responses, the results were quite different. For the PDI, all terms that suited the model obtained p-values below 0,05, whereas the %EE produced opposite results, with 0,048 as the smallest p-value

obtained. The only terms that fitted the model for the representative population were the SPIONs volume, with a p-value of 0,001, and the respective square model, although with a p-value of 0,088. Lastly, for the minority population, the three linear terms fitted the model, with the sonication time as the term with less significance, with a p-value superior to 0.05. For all the terms, in every response regression, the variance inflation factor (VIF) obtained was 1, indicating that there was no correlation between terms.

Still on the left side of Figure 8, the first line showed a p-value for the model of 0,001. Thus, it was possible to conclude that the model explains variations in the response and therefore the model is well adjusted. All the other responses obtained similar values, with p-values of the models ranging from 0 to 0.025, as presented in the Figure SI.2.

In order to determine if the model properly specifies the relationship among response and factors, a comparison between the p-value for the lack-of-fit – a measure of error calculated by the software - and the significance level of 0.05 was performed. Therefore, lack-of-fit values greater than 0.05 means the error is not statistically significant. For the mean size, PDI and minority population, such result was observed, with p-values for the lack-of-fit of 0.675, 0.836 and 0.422, respectively. However, the representative population and the %EE obtained values of 0.031 and 0.025, meaning these responses and the terms suffer from a lack of fit, with the model not specifying their relationship properly.

Regarding the R^2, the outcomes obtained for the mean size, across all the three percentages, can be qualified as good results, meaning the model fits the data very well and can predict new observations not perfectly, but considerably well. Likewise, the PDI obtained 85.4% for R^2 and 79.5% for the adjusted R^2, However, the model cannot quite predict new observations with precision, with only 57.0% for the predicted R^2. In fact, all the other predicted R^2 were very low, with 45.6% for the representative population, 51,8% for the minority population and, surprisingly, 2.3% for the encapsulation efficiency. This last value, combined with the lowest R^2 and adjusted R^2 (64.0% and 49.6%, respectively) obtained, showed that this model did not fit the data. The two populations presented R^2 not as good as the mean size, with the data fitting 67.8% and 73.1% of the model, with adjusted R^2 of 62.4% and 65.7%. Given that R^2 always increases with the addition of more terms, the adjusted R^2 is best suited to compare the models with different responses.

Hence, from the five models, only four were used for the optimization: mean size, both populations and the PDI, with the respective equations included in the Figure SI.3. The addition of the representative population, even though it presented lack-of-fit, was considered given the importance that optimizing such parameter represents for the proposed application - for biofilm eradication, the best suited delivery route is intravenous injection, limiting the size range. Moreover, closing the gap between populations was also pretended. Despite presenting lack of fit between the experimental factors and the response variable, the p-value of the model was below 0,05, meaning the model was well adjusted. On the other hand, the

optimization did not include the %EE. The reasons behind such verdict were the obtained lack of fit, the randomness of new observations as a result of the predict R^2 and the high number of models already chosen. Additionally, the results for the %EE seemed to be not influenced by the independent variables. Such conclusion was supported by the Pareto Chart provided by the software that can be found in the Figure SI.4, which presents a graphical presentation of the standardized effect of each term in the response. The graph for the %EE showed a small effect for every term that fitted the model – sonication time, square term of lipid concentration and 2-way interaction of SPIONs volume with both lipid concentration and sonication time. The two population were more affected by the SPIONs volume, while the sonication time was the main influencer for the PDI. The Pareto chart for the mean size is presented below in Figure 9, where it is visible the effect that all three factors had on the response, with the lipid concentration and SPIONs volume as the more relevant.

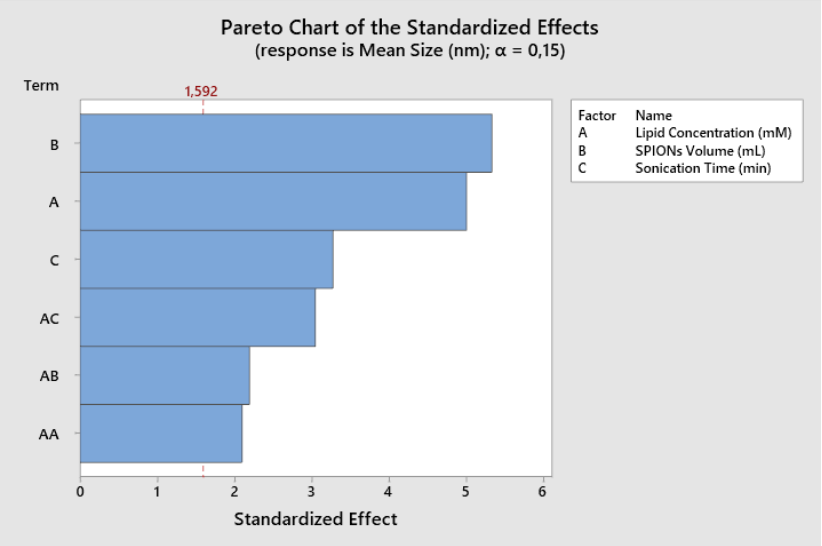

Figure 9 – Impact of each term in the mean size, illustrated by a Pareto Chart

Furthermore, the residual plots for each model are presented in the Figure SI.5. On the right, the residuals are displayed by order, assessing the freedom between them. Here, no pattern was identified, indicating there was no correlation. On the left column, it is shown the graphics of residuals versus fitted values, where a random distribution of residuals is pretended. The graphs for the minority population and PDI did not present detectable patterns, with the point randomly distributed. Moreover, the mean size and representative population obtained some outliers (points far away from the 0) –the runs 9 and 13 were outliers for the mean size, whereas the run 4 was the only one for the representative population. For the %EE graph, an influential point (a run far away from the remaining, but in the x-axis) was observable, as expected. From the 15 experimental runs, a 99,1% encapsulation was registered one time, more than 10% superior to the second highest value. However, the other parameters

of that run were not desirable, illustrating the importance of a Box-Behnken in finding the right optimization in a scenario with multiple analysis.

Lastly, the surface plots and contour plots were drawn, for a graphic display of the combined effect of two variables on a certain response. While the same information can be gathered from these representations, the surface plot presents a 3D visualization and the contour plot only uses two dimensions. Below, in the Figure 10, all the graphics from the mean size can be found, while the remaining were placed in the supplementary information (Figure

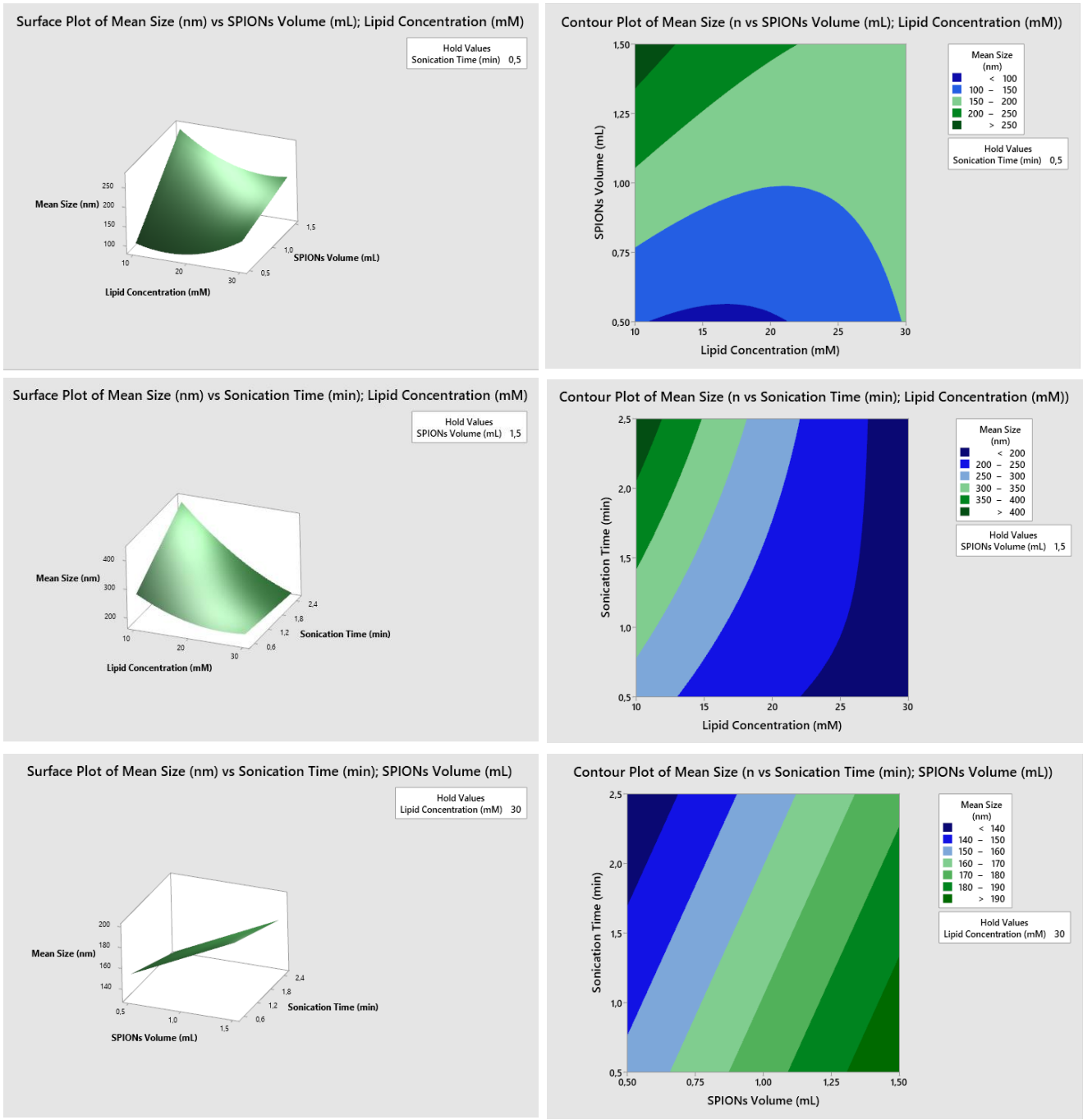

Figure 10 - Surface and Contour plots for mean size

SI.6). As it is only affected by the SPIONs volume, the representative population did not present these plots.

Analysing these plots is very direct, with the 3D surface plot offering depth to the image while the colour-based 2D contour plot allowed a simple perspective of the mean size flow driven from the fluctuation of two independent variables. The first line of graphics showed the mean size versus the SPIONs volume and the lipid concentration, holding the sonication time at 0,5 min. It was possible to understand the influence both variables had in this response: mean sizes above 250 nm were possible combining low concentrations with high volumes, whereas a mean size between 150 and 200 nm (light green in this specific contour plot) could be achieved with a large number of combinations. In the second line, the SPIONs volume was set to 1,5 mL and the sonication time was evaluated with the lipid concentration. As seen before in the Pareto chart, the lipid concentration proven to be more impactful than the sonication time. In fact, the impact of sonication was only observable at low concentrations, where a bigger sonication time would lead to mean sizes superior to 300 nm. After a lipid concentration of 25 mM, the mean size would be the same (under 200 nm) across every sonication time in the range applied in the protocol.

Fixing the lipid concentration at 30 mM, it was possible to conclude that larger volumes were related to an increased mean size. However, contrarily to the absence of an effect previously observed at 30 mM, an increasing sonication time would slightly reduce the mean size across all volumes.

From the plots dedicated to the PDI, it was noticeable that sonication times below 1 minute were enough to ensure low levels of polidispersity. The contour plot for the sonication time and SPIONs volume showed that, for 30 mM, every volume was capable to deliver a PDI below 0.200, as long as the sonication time remained below 1.5 minutes. By switching the SPIONs volume with the lipid concentration, a more relevant impact was found for the lipid concentration. This time, obtaining a PDI below 0,200 was possible for every concentration plus 0.5 minutes as the sonication time, however, while increasing the lipid concentration, the sonication time could also be increased, up to almost 1,5 min at 30 mM. Such tendency was confirmed with the contour plot combining the SPIONs volume and the lipid concentration, fixing the sonication time at 0,5 min, with the lipid concentration presenting a bigger impact than the SPIONs volume.

For the minority population, the three surface plots obtained were flat squares with different inclinations, which translated into contour plots with only oblique lines. These conformations indicated that all three independent variables affected the final size. To only minimize the minority population, the best conformation would be a lipid concentration of 30 mM, 0.5 mL of SPIONs and 0.5 min of sonication.

5.2.1. Response Optimization

After choosing the models, the next step was deciding the different targets for the four responses, between a minimum, maximum or a target value. The PDI was set to the minimum, to improve the monodispersity of the formulation, while the other responses were set to a target, with 100 nm for both populations. However, with the representative population set to 100 nm, the minority population would never reach a value so low. Therefore, to guarantee a mean size below 200 nm, this response was set to 175 nm as the goal. The limit of 200 nm is related with the possibility of administrating this formulation intravenously, as an approach to overcome biological barriers to drug delivery presented by our system. The optimization was then performed by the software, with the results presented below in Figure 11.

Variable	Setting			
Lipid Concentration (mM)	30			
SPIONs Volume (mL)	1,5			
Sonication Time (min)	0,5			
Response	**Fit**	**SE Fit**	**95% CI**	**95% PI**
PDI	0,1567	0,0141	(0,1252; 0,1882)	(0,1074; 0,2059)
Minority Pop. (nm)	285,4	36,9	(204,2; 366,6)	(138,6; 432,2)
Representative Pop. (nm)	99,96	5,64	(87,66; 112,26)	(72,46; 127,46)
Mean Size (nm)	199,0	29,3	(131,4; 266,7)	(103,4; 294,7)

Figure 11 - Optimization parameters obtained from the software

The optimized formulation obtained by the software was composed of 30 mM of lipid concentration, 1.5 mL of SPIONs and half a minute of sonication, with a desirability level of 0.824, indicating a good adjustment to the desired responses. The software prediction for the response and the respective 95% confidence interval and 95% prediction interval are shown in the Figure 11. Additionally, the Figure 12 offered a deeper perspective into the optimal response and the influence of each variable. As an example, it was possible to visualize the impact of the sonication time on the PDI, whereas the SPIONs volume did not displayed a relevant influence in that parameter. Both mean size and minority population were optimized combining the three factors, while the representative population only displayed an exponential relationship with the SPIONs volume.

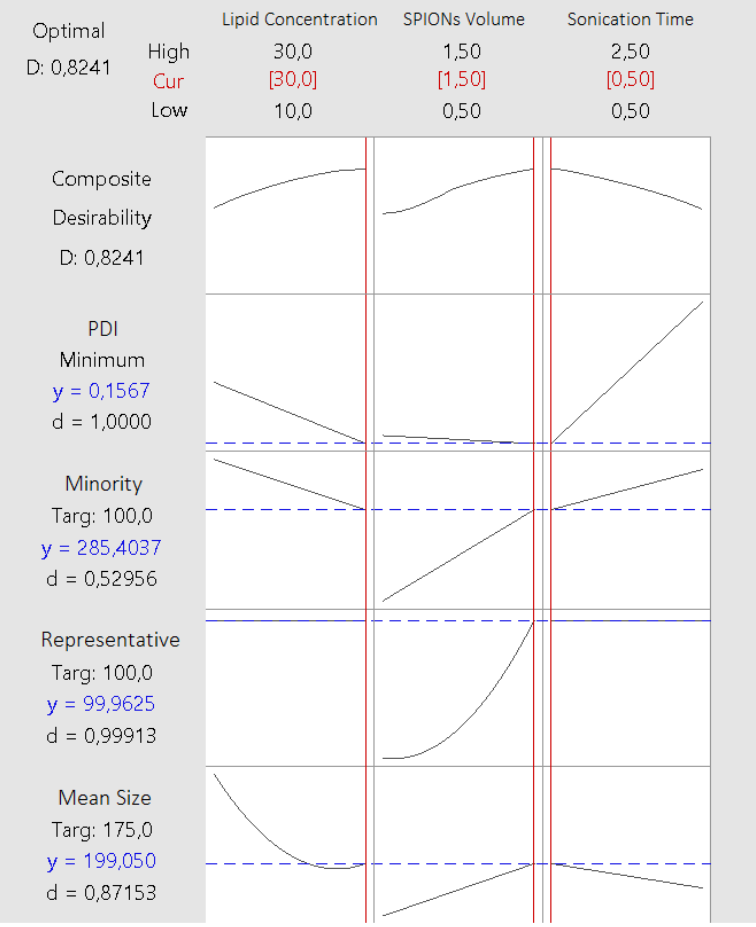

Figure 12 - Influence of each optimized variable in the response

5.3. Characterization of the Optimized Formulation

5.3.1. Size Distribution and Polidispersity Index

The optimized formulation was then prepared in triplicate and compared with the predicted responses from the software. The results are exhibited in the Table 7 below and comparing with the 95% prediction interval, all the mean values were between such limit. As expected, it was not possible to push the minority population to 100 nm, but the overall results (mean size and both populations) were within the expectations. However, the mean value for the PDI barely made into the 95% PI, with two replicates outside that range. That may be explained by the percentage of the minority population in the two replicates with the PDI over 0.200. The results for the %EE, even though it was not optimized, can be classified as satisfactory, but future works should focus on improving this parcel of the formulation.

Table 7 - Characterization of the optimized formulation

Experimental Runs	Mean Size (nm)	Representative Population (nm)	%	Minority Population (nm)	%	Polidispersity Index	%EE
R1	171.5	78.7	*97*	261.2	*3*	0.194	73.2
R2	193.1	92.2	*94*	278.0	*6*	0.206	55.7
R3	180.6	104.4	*87*	307.5	*13*	0.207	68.5
Mean Value	181.7	91.8	*93*	282.2	*7*	0.202	65.8
Standard Deviation	8.9	10.5	*4*	19.1	*4*	0.006	7.4

5.3.2. Phase Transition Temperature

Besides the properties evaluated in the previous experiment, the behaviour upon modifications in the temperature also need to be addressed. At their phase transition temperature, liposomes lose their rigid phase and become more permeable, with increased space between the previously packed phospholipids. From the transition temperature onwards, a more fluid crystalline phase can be observed, with disordered phospholipids (Michel *et al.*, 2006). With several conformal changes at that stage, such as modifications of lateral diffusion, thickness, lateral expansibility and permeability, it is fundamental to understand their impact on the application in hands.

However, these conformational changes allow for an easy determination method of T_M, using the mean count rate of the DLS. As stated by Michel *et al.* (2006), discontinuities in the mean count rate as a result of temperature variation is related to a change in the optical properties of the material in question, reflected by changes in the measured scattering intensity. Therefore, the transition temperature between phases can be determined by obtaining the mean count rate at several temperatures and applying the equation presented in the methods sections responsible for the sigmoid curve (Michel *et al.*, 2006).

The results for the two formulation are summarized in the Figure 13. For the optimized formulation with SPIONs, the curve fits the sigmoid curve, with a significant reduction in the normalized count rate from the 23ºC onwards. Additionally, the adjusted R^2 obtained was 0.9805, indicating a slight difference between the curve and the experimental data, which can be graphically observed. For this formulation, the T_M obtained was 37.9ºC, with a standard deviation of 0.3ºC.

Regarding the empty LPs, a similar relation between the curve and experimental data was shown. However, a sigmoid regression is not well adjusted. Nevertheless, by applying the same equation, the T_M for this formulation would be 31.8ºC with a standard deviation of 7.1ºC.

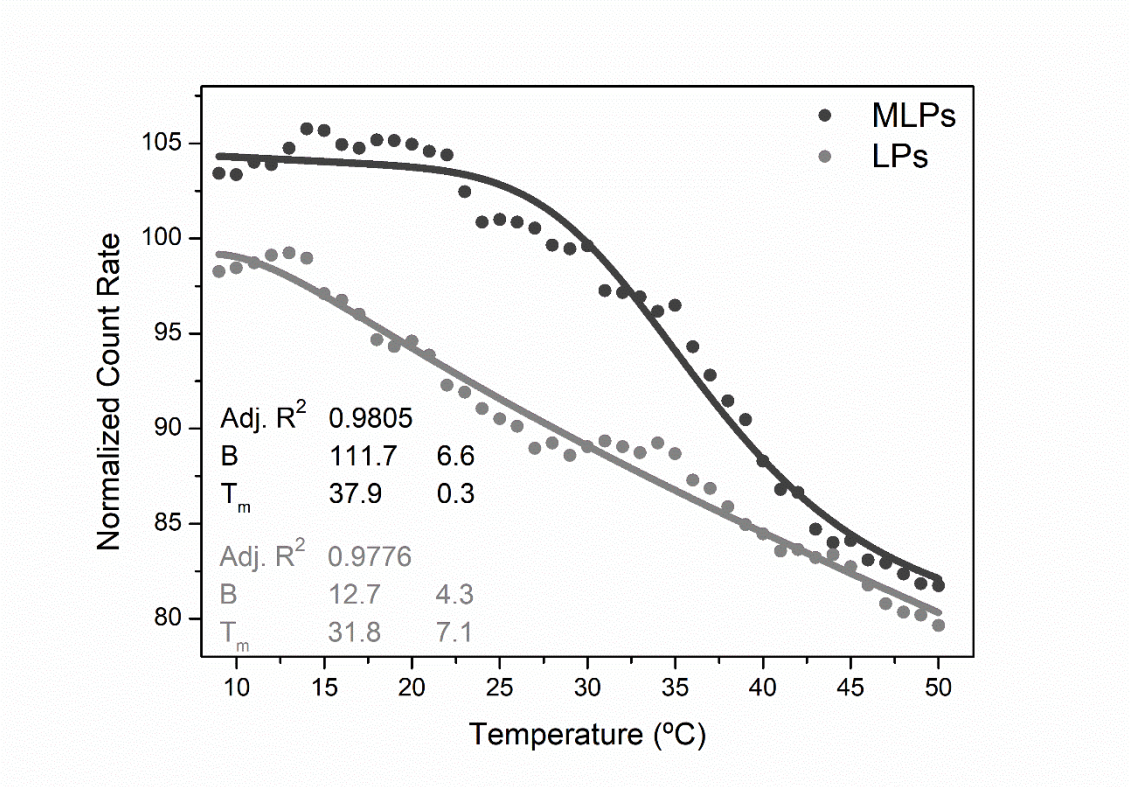

Figure 13 – Normalized count rate as a function of the temperature, for both MLPs and empty LPs

By looking into the lipid composition of the formulations, it is possible to understand the origin of such value for the T_M. The 4:2 ratio of DPPC:DOPE, known for having a T_M of 41ºC and -16ºC respectively, elucidates the disturbing effect of DOPE in the packing of phospholipid, decreasing the T_M. In fact, Filipa Soares (2019) obtained a T_M of 22.54 ± 0.27ºC for a formulation with this composition (Filipa Soares, 2019). However, the addition of a small percentage of PEG linked to DPPE (T_M of 63ºC) at the expense of some DOPE explains the increase when compared to the same formulation without PEG. Other influencing factors may be the increased concentration (from 15 mM to 30 mM) or the SPIONs volume, which was the triple.

While the sigmoid curve presented by the formulation with SPIONs allows for the visualization of a well-defined phase transition, the empty LPs did not follow the same pattern. Although sharing the same composition, the presence of SPIONs and their interactions with the head region of the phospholipids may interfere with the lipid distribution across the bilayers, reducing the possible clustering between lipids of the same type. Such phenomenon would prevent an equal distribution of the lipids and therefore different phase transitions could be

found depending on the location in the membrane, which may explain the lack of a defined transition in the empty LPs. Thus, a larger temperature range should have been used, as an approach to identify possible decreases in the mean count rate close to the individual T_M of the lipids instead of restraining the range to the expected T_M of the mixture (which was not possible due to restrictions with the DLS). To confirm these conclusions and validate the obtained results, more complex methods should be used, like differential scanning calorimetry (DSC), nuclear magnetic resonance (NMR) and FTIR (Michel *et al.*, 2006).

5.4. Preparation and Visualization of GUVs

To obtain the best possible images of GUVs, several conditions were changed back and forward, aiming for clean images of GUVs with homogeneous sizes and without background. With the vast number of variables throughout the preparation, some were fixed from the beginning. For example, the base protocol was chosen and kept for all the experiments and the rehydration solution was always D-sorbitol.

Initially, a preliminary assay without fluorescence was performed. Here, two lipid concentrations were tested (5 and 10 mM) with three different D-sorbitol concentrations (350, 650 and 900 mM). Graphically, the results were not the best, as expected – nonetheless, there were slight improvements following the increase in both concentrations. Between 5 mM and 10 mM, the later presented smaller sizes. In fact, Klaerke *et al*. (2018) mentioned that GUVs size obtained with Vesicle Prep Pro can vary depending on the lipid concentration, from 1 µm (higher concentrations) to 100 µm (smaller concentrations) (Klaerke *et al*., 2018). Since *S. aureus* normally present sizes very close to the lowest value, higher lipid concentration should be chosen, supporting the preliminary assay. Regarding the D-sorbitol solution, low concentrations resulted in multilamellar vesicles, while 900 mM presented unilamellar GUVs. Additionally, higher concentrations help stabilizing the negative charge presented by the POPG to the membrane.

Another important factor to consider was the conceivable contamination by water. To avoid it, the lipid solution should be able to rest at room temperature (if stored at -4ºC) for at least 30 minutes before opening the glass container, to prevent water condensation. Then, after placing the lipid amount on the slide, evaporation should happen in less than a minute (more than that may promote water contamination) resulting on a yellow and transparent thin layer (if it appears as a white deposit, it may indicate the presence of unwanted water). Nonetheless, besides just waiting less than a minute for the evaporation, placing the slide inside a vacuum dessicator was also experimented. Lastly, air bubbles between the two ITO slides and inside the O-ring should be avoided. To achieve that, the upper slide should be lowered at an angle (Klaerke *et al*., 2018).

Moreover, some approaches were tested after the GUVs formation to gather the best possible images from the microscope. Besides the dilution referred in the methods section, others were also experimented, ranging from no dilution up to 1:50. Another relevant condition tried was the time period between electroformation and observation, with periods from 15 minutes up to 5 days. Regarding additional steps to the protocol, various centrifugations were tested (as well as a centrifugation with a 0,45 µm filter) and a dialysis apparatus (Slide-A-Lyzer® 10K Dialysis Cassettes from Thermo Scientific).

For the visualization, a Nikon DAPI-FITC-TRITC filter combination was used. The middle one presents an excitation filter with a narrow bandpass window in the blue, with a wavelength ranging from 475 to 490, approximately. Thus, NBD has an excitation spectrum in the wavelength of the FITC window, meaning thar a blue excitation with the FITC filter will result in a green emission detection.

From the portfolio of images gathered, below is presented one of the samples with the parameters highlighted in the methods section. After the electroformation, a 1:3 dilution was achieved and the samples stored at 4ºC. The images were taken on the subsequent day, approximately 24 hours later.

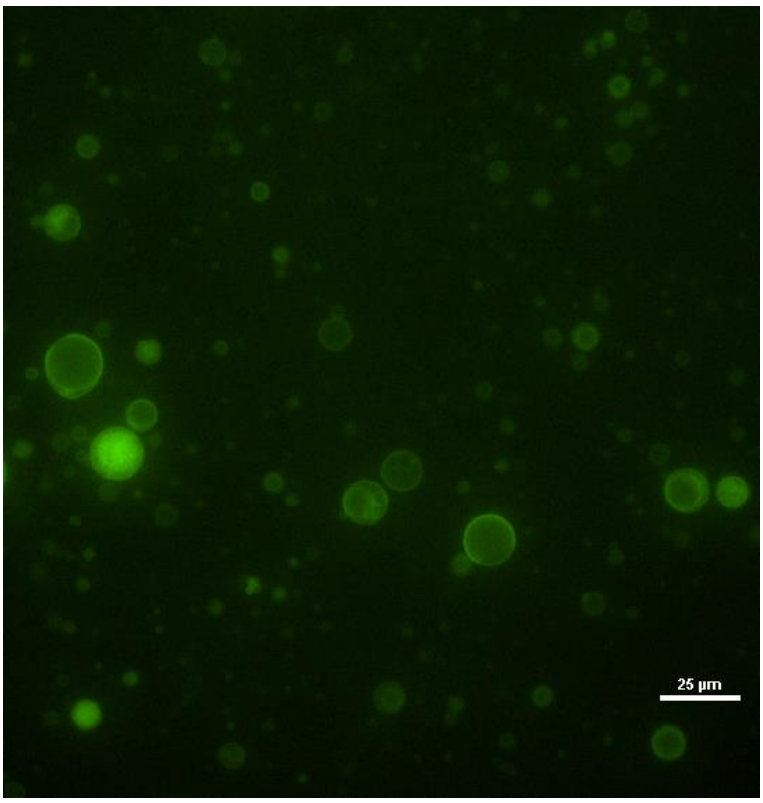

Figure 14 – GUVs 1:3 (40x objective), a day after the electroformation

Using an exposure time of 100 ms and adjusting both brightness and contrast in the program, the result is here shown. From diameters starting at 2 µm up to 12 µm, the samples

were not homogeneous as expected, yet, a range of 10 µm may be acceptable, given the nature of the experiment, the goal pretended and also the order of magnitude in question. The background, however, was not fully removed, despite the several approaches targeting that specific problem. In fact, even the conditions used for the image above sometimes lead to a sturdy interference from the fluorescent dye that did not incorporate the vesicle's membrane (Figure SI.8). Whereas some vesicles presented a good morphology (with a well-defined membrane with a circle shape), the sample as a whole suffered from more than a few drawbacks. Besides the wide-ranging sizes and background limitations already referred, the samples itself were very heterogenous (Figure SI.9), possessing some artefacts like the one on the left side of the figure above. Additionally, a particular occurrence was verified, more common as recent the sample was - after the GUVs formation, a fusogenic phenomenon between GUVs was found, with various clusters of small GUVs registered. Such manifestation was found up to 48 hours after the end of the electroformation and can be seen in the Figure SI.10.

As an attempt to improve the image above, several methods were tried. For the dilution, the best results were obtained with small values, ranging from a dilution 1:2 up to a dilution 1:5. After choosing the dilution 1:3, some additional steps to the process were added. Unfortunately, none of them improved the results already registered. One of the images obtain after using the 10000 MW dialysis cassettes can be found in the Figure SI.10, where some vesicles offered good morphology, although some clusters were present as well as the background. For the centrifugation with a 0.45 µm filter, nothing was retained in it and the Figure SI.11 displays the solution that went through – besides the background problem, there were more unknown particles than well-defined GUVs. Regarding the centrifugations and the addition of the vacuum dessicator step, the results were even worse, either amplifying the background or destroying the GUVs. For example, the Figure SI.12 was the supernatant after a 200rpm centrifugation at 20ºC during 5 min, while the pellet did not demonstrate any fluorescence at all.

The visualization protocol was also adapted while searching for the best measures. Besides the traditional microscope slide, a 96-well plate was also tested. The finest images were obtained on the microscope slide after mixing a drop of the GUV solution and a drop of water, however, the observation must be performed rapidly, as the GUVs deteriorate in water over time (Barthmes *et al.*, 2016).

The last decades offered new perspectives for the use of GUVs as bacterial-membrane mimetic models, making use of their qualities compared to the other models. However, when trying to mimic bacteria (*S. aureus* more specifically, for the work in question) while keeping the integrity of the model, some limitations need to be factored. For example, some authors follow the *S. aureus* composition while developing mimetic models and therefore follow the path of molecular ratios of 60:40 and 3:2 of PG:cardiolipin (Kao *et al.*, 2012; Sani *et al.*, 2013),

the true composition of *S. aureus*. However, while optimizing the mechanism in that regard, both authors had to choose LUVs below 100 nm instead of GUVs, as the last was very unstable with such composition. From another perspective, authors follow the qualities of GUVs and choose these giant vesicles to mimic bacterial membranes. In this pathway, the limitations are linked with the allowed composition and size, diverging from bacteria in that context. For example, GUVs of DOPC:DOPG 75:25 and DOPC:POPG 70:30 were already reported by the respective authors as approximations to bacteria membranes (Ciobanasu *et al.*, 2015; Al Nahas *et al.*, 2019). While the membrane properties may be similar to the membrane of a bacteria, these models focus on mimicking sections of the membrane for their studies and do not attempt to mimic the bacteria membrane as a whole (allowing them to neglect the size). However, to develop a nanosystem capable of eradicate the *S. aureus* biofilms in the human organism, the mimetic model needs to combine the two standpoints referred: GUVs with a more suitable composition and size. Here, despite the limitations faced during the imaging process, the obtained GUVs added a more appropriate size to the mimetic model while keeping the vesicles with the 70:30 ratio. Moreover, the chosen concentrations for the lipid and rehydration solutions played a fundamental part on the size recorded.

From this point, a better protocol needs to be considered to improve the quality of the display. Then, the next step should be to bring the membrane composition of the giant vesicles closer to the *S. aureus* membrane. Yet, despite these optimizations, the fusion process with the nanosystem developed before could be verified and the results are presented in the Section 5.5.

5.5. Membrane Fusion Evaluation

The final experiment in this work was a preliminary fusion assay between the GUVs with NBD and the optimized MLPs with Rho. The Nikon DAPI-FITC-TRITC filter combination referred before is designed for simultaneous detection with minimal crossover between adjacent bands, which is another reason why the NBD-Rho pair is so often used. As explained in a previous section, the excitation spectrum of NBD is in the wavelength of the FITC window, meaning that a blue excitation with the FITC filter will result in a green emission detection. However, it will not affect the signal from the MLPs, which can be seen with the TRITC filter – it offers an excitation filter with a narrow bandpass window in the green, with a wavelength ranging from 545 to 565 nm, close to the excitation wavelength of Rho – and characterized by a red emission detection. Therefore, the samples were placed in the microscope and after choosing the framework pretended, two photographs were taken without moving the samples: one with the FITC filter to only observe the GUVs and the other with the TRITC filter to see the red coloured MLPs. Then, the images were merged with the NIS-Elements Viewer program and analysed.

Since the solvents used were different, a solvent exchange was performed, to address a possible negative impact of PBS in the GUVs stability.

The ratio for the fusion was chosen based on reports founds in the bibliography, such as the 4:1 ratio used (Trier *et al.*, 2011) and a 5:1 ratio as well (Lira *et al.*, 2019). The images obtained also suffer from the excessive background already mentioned from the GUVs solution, which resulted in very low-quality images. However, from a direct observation of the merged images (Figure 15 and 16), it was possible to see the underlines of a successful fusion. In fact, the fusion appears to occur between multiple GUVs and multiple MLPs, instead of a single GUV with multiple MLPs – as a result, the size of the vesicles increased substantially. It is also possible to observe an orange colouring in the GUVs membrane, which may indicate the occurrence of hemifusion (a step towards the full fusion, where the mixing of the lipids from the outer membranes occurred).

Comparing the results of MLPs suspended in D-sorbitol and suspended in PBS, it seems to indicate that neither the PBS nor the solvent replacement protocol negatively affected the vesicles and the fusion process, given the similarities recorded between the images - Figure 15 shows the two images obtained when using D-sorbitol, whereas one of the images of the fusion with MLPs in PBS is shown in the Figure 16.

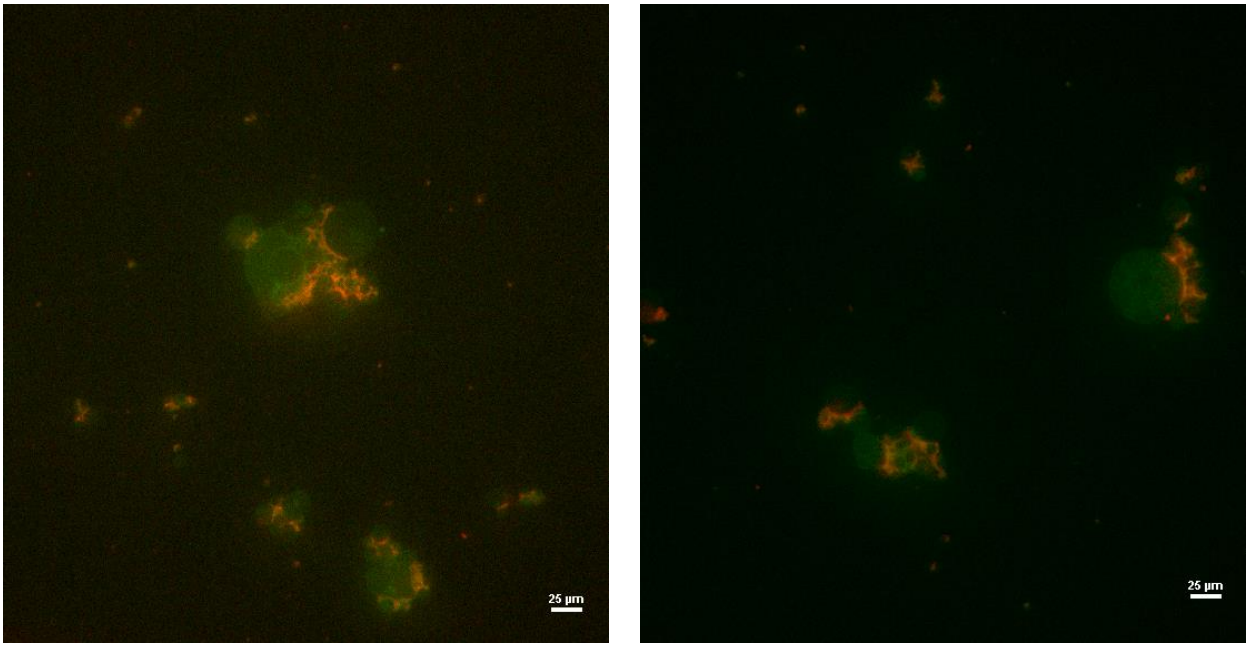

Figure 15 – Merged images from MLPs in D-Sorbitol and GUVs, addressing the fusion process

Despite these results being fairly preliminary, a promising proof-of-concept can be taken from them. Nanotechnology-based approaches play a pivotal role in the search for more effective strategies to combat bacterial infections, where SPIONs have already demonstrated their potential. When combined to another "stealth" nanosystem, fighting bacterial infections

in the human body becomes a reality, albeit dependent on the ability to perform more effective screenings of new molecules and nanosystems, for a safe and effective application. In that regard, bacterial membrane mimetic systems are being exploited as replacements for the bacteria itself since interaction studies with bacteria are time consuming and many times require special work conditions (like *S. aureus*). Here, the fusion between GUVs representing a *S. aureus* mimetic model with the nanosystem developed, strengthens the ideology of using hybrid nanosystems with SPIONs to eradicate biofilms in the human body, not limited to *S. aureus*, but with an emphasis on it due to its incredible developed antibiotic resistance. More studies on this need to be performed, but these results offer a good perspective on both systems used in this work.

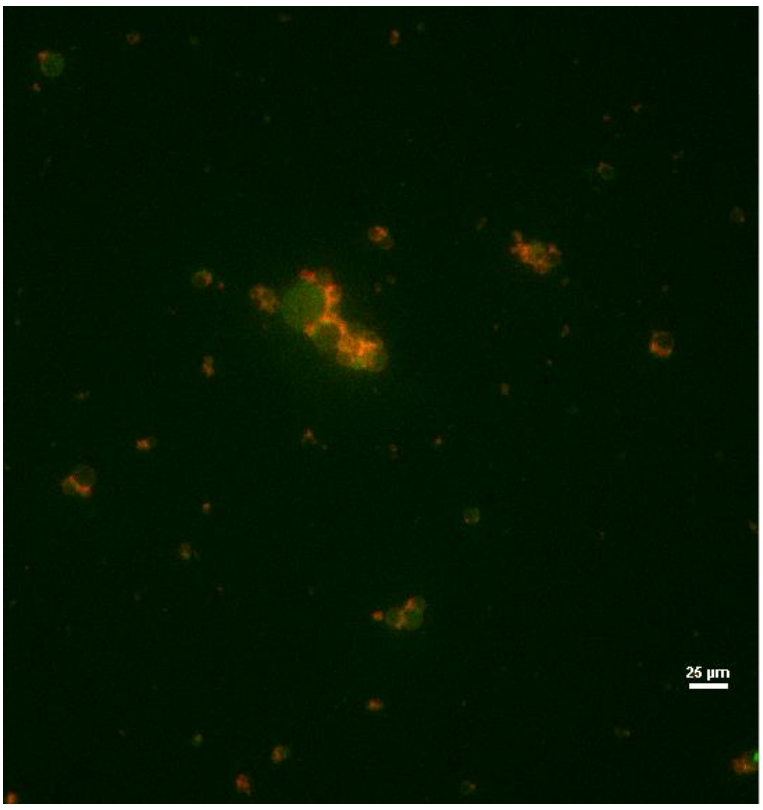

Figure 16 – Merged images from MPLs in PBS and GUVs, addressing the fusion process

5.6. FRET Assay with LUVs

To evaluate the possible membrane fusion between the optimized MLPs and DMPG LUVs, a Förster resonance transfer energy assay was developed. While the main theory was introduced in the 1940s by Förster, only recently the technique expanded, following the developments in nanoscience and nanobiotechnology. The reason behind such evolution is related with the r^{-6}

distance dependence, approximately between 1 and 20 nm, values that fit incredibly well with recent nanotechnologies. By definition, FRET "is an energy transfer process between a luminescent donor molecule or particle (the donor D) and a light-absorbing acceptor molecule or particle (the acceptor A)" (Medintz and Hildebrandt, 2014). These two molecules are called the FRET-pair, where some conditions need to be fulfilled. The acceptor A must be capable of absorbing light in the same spectral range as the emission of D. The relationship between the absorption energy of A and emission energy of D is called the "resonance condition", completing the acronym of the technique. In FRET, the luminescence energy from D is transferred nonradiatively through dipole-dipole interactions to A with an efficiency (η_{FRET}) that is dependent on the distance between them: $\eta_{FRET} \approx r^{-6}$, as initially introduced.

Mathematically, the r^{-6} influence in the FRET rate (K_{FRET}) can be observed by the following equation:

$$k_{FRET} = \frac{9(\ln 10)\kappa^2 \Phi_D}{128\pi^5 N_A n^4 \tau_D r^6} J \tag{5}$$

where κ is orientation factor between A and D, Φ_D is the luminescence quantum yield of D, τ_D is the luminescence lifetime of D (in the absence of FRET), n is the refractive index, N_A is Avogadro's number and J is the spectral overlap integral, which is generally defined in the wavelength scale. At a certain distance, an equilibrium between the FRET rate and all other decay rates can be observed (where $k_{FRET} = {\tau_D}^{-1}$), which is called the Förster distance (R_0) and known by the distance at which the energy transfer efficiency is 50%. The Förster distance can be calculated by replacing k_{FRET} with ${\tau_D}^{-1}$ and r with R_0 in the previous equation, resulting in the following equation.

$$R_0 = \left(\frac{9(\ln 10)\kappa^2 \Phi_D}{128\pi^5 N_A n^4} J\right)^{\frac{1}{6}} \tag{6}$$

To determine R_0, it is important to consider the different units across all the parameters affecting the final value. Starting with the constants, they can be combined into one value:

$$\frac{9(\ln 10)}{128\pi^5 N_A} = 8.79 \times 10^{-28}\, mol \tag{7}$$

From there, the several equations already reported are in line with the chemical units used to determine the remaining parameters, with the spectral overlap integral having a major role in the final unit. If the units of J are $M^{-1}cm^3$, the R_0 can be determined by the Equation 8, presented below (Cheung, 2002).

$$R_0 = [8.79 \times 10^{-25} \ (n^{-4} \kappa^2 \Phi_D J)]^{\frac{1}{6}} \ cm \tag{8}$$

To calculate the FRET efficiency, a plethora of methods have been reported, from determination by donor quenching or acceptor sensitization to donor or acceptor photobleaching. Here, the first was used by comparing the spectroscopic data of the donor in the absence and presence of the acceptor. By combining Equations 5 and 6, it is possible to obtain a relation between the FRET rate, the luminescence decay time of the donor and the distances (Equation 9). Then, the FRET efficiency can be expressed and worked in a way that allows its determination with the spectroscopic data obtained (Medintz and Hildebrandt, 2014).

$$k_{FRET} = {\tau_D}^{-1} \left[\frac{R_0}{r}\right]^6 \tag{9}$$

$$\eta_{FRET} = \frac{k_{FRET}}{k_{FRET} + {\tau_D}^{-1}} = \frac{1}{1 + \left({}^{r}/_{R_0}\right)^6} = 1 - \frac{\Phi_{DA}}{\Phi_D} = 1 - \frac{\tau_{DA}}{\tau_D} = 1 - \frac{I_{DA}}{I_D} \tag{10}$$

The last part of Equation 10 can only be used if all the measurement parameters are the same for both experiments (absence and presence of A), which was the case in this work.

Schematically, the basic FRET principle can be represented with a Jablonski diagram, as shown on the left side of Figure 17. The acceptor must have an excitation spectral range in the same wavelength as the emission spectrum of D. One example is the NBD-Rho pair, one of the most common FRET-pair and the one used in this work. In the right side, the overlap of both excitation and emission spectrums of NBD and Rho is presented, confirming the good match of these two fluorescence dyes for the experiment.

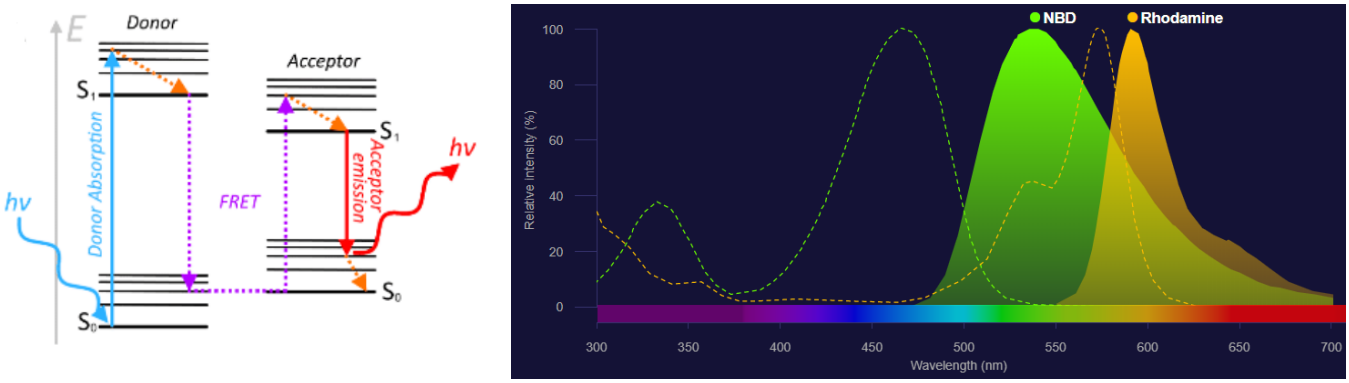

Figure 17 - A Jablonski diagram is presented on the left (Hochreiter et al., 2015), while the emission and excitation spectrums (dashed line - excitation; coloured - emission) are represented on the right, obtained from the Fluorescence SpectraVierwer from ThermoFisher Scientific

As for the FRET assay itself, the voltage was optimized at 390 V, which translated into a maximum absorbance peak below 850 for the emission spectrum of NBD. The 11 samples with different concentrations of Rho were then performed and the wavelength spectrums obtained were overlapped in one single picture, shown in Figure 18. It is the confirmation of the energy transfer process, with the acceptor peak rising, following the concentration increase. With an excitation wavelength of 460 nm, the donor (LUVs with NBD) was able to absorb the energy provided and transfer it to the acceptor present in the mixture – higher concentrations were able to receive more energy leading to higher absorbances until the saturation.

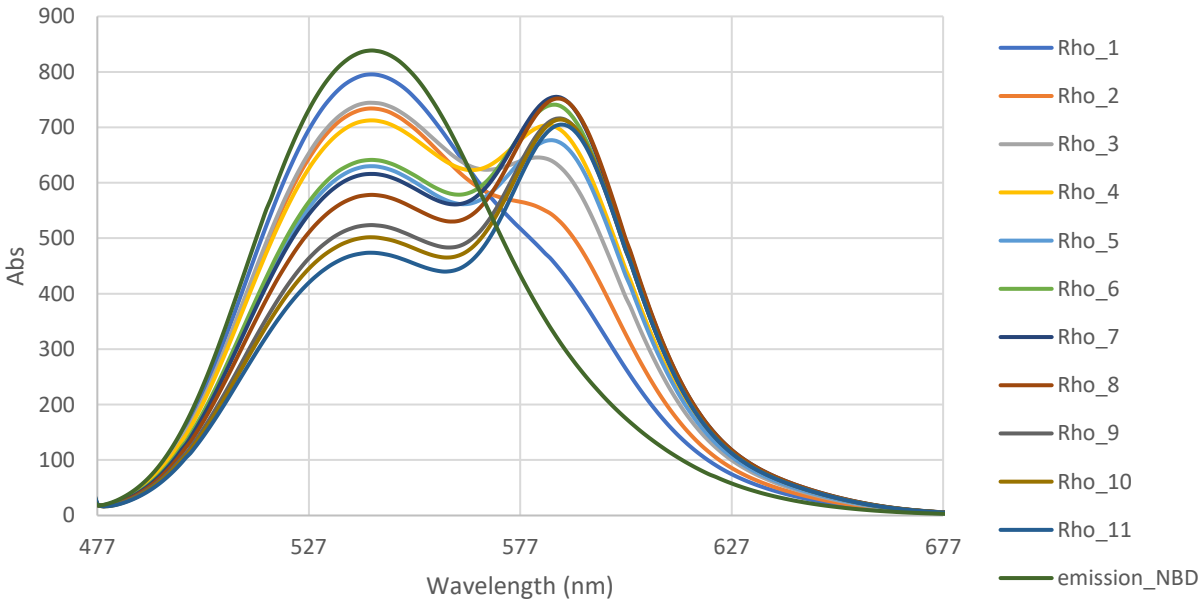

Figure 18 - Schematic compilation of FRET assay results, with the DPPE-NBD peak on the left and the DOPE-Rho on the right, indicating a successful energy transfer from one fluorescence dye to the other

The saturation was obtained with a concentration of 0.35 mM of the acceptor, the optimized formulation with rhodamine. From that moment onwards, the reduction of fluorescence intensity from the LUVs with NBD was not accompanied by the opposite effect from the MLPs. Thus, the FRET efficiency was calculated with the Equation 9 for the Rho_7 sample, obtaining an efficiency of 26.5%. These results are in line with the expected since the presence of PEG in the membrane of the MLPs should impact the transfer process negatively. To confirm such conclusion, an assay without PEG should also be performed in the future.

To further confirm the occurrence of fusion, the size of both donor and acceptor before fusion were measured in the DLS and compared with the size of one of the samples. Whereas all samples could be used here, the two with higher fluorescence intensity for the MLPs were the most suitable to obtain the maximum contrast in size. For the LUVs with NBD, the mean size was 159.7 nm with a PDI of 0.024. Meanwhile, the MLPs with Rho obtained a mean size of 136.5 nm and a PDI of 0.,126 (two populations were observable, where 98% were around 50 nm

and the remaining close to 163 nm). The Rho_8 sample was chosen and the mean size registered was 198.5 nm, with two very distinguished populations: while 92% had a size close to 93 nm, the bigger population was far superior, with sizes around 700 nm, resulting in a PDI of 0.321. These differences support the fusion procedure, suggesting different mechanisms: partial fusions resulting in sizes of 93 nm and multiple fusions were responsible for the agglomerates of 700 nm.

The magnitude of R_0 is dependent on the spectral properties of the donor and acceptor dyes, as well as the lipid composition of the vesicle in play. For FRET to occur, the two molecules need to be in close proximity (below 10 nm), which was verified here, with a calculated R_0 of 2.8 nm. This value supports the results obtained before, yet, it differs from the value found in the bibliography of 4.9 nm for the same FRET pair (Pathak and London, 2015). However, the lipid mixture and the characteristics of the vesicles were quite different, easily justifying the discrepancy between the two values.

Additionally, another FRET experiment was prepared after discovering a different NBD – DSPE-NBD – mixed with the DPPE-NBD. It was then possible to prepare an assay to address the possible effects that the stiffness of the membrane domain could had on the fusion. Two FRET assays were then prepared, using LUVs with different NBD but sharing the same MLPs.

In the Figure 19, it is presented the contrasts between both results. On the right, the absence of FRET from the DSPE-NBD is shown, whereas the results from DPPE-NBD are presented on the right, with a clear energy transfer between the two participants. Moreover, the samples were also analysed with the DLS, comparing the different sizes before and after the supposed fusion. While the MLPs were the same for both trials and presented a mean size of 210 nm (and the typical dual population), the two DMPG with different NBD were measured and the results were very similar: 171,2 nm for the DSPE variant and 174,1 nm for the DPPE variant, with PDI below 0,070. After the FRET, the sample with the biggest concentration of Rho was evaluated and the results were very curious: the mean size was the same for both experiments (195,4 and 195,6 nm) with PDI of 0,200 for DPPE-NBD and 0,184 for DSPE-NBD. However, while the FRET with DPPE-NBD obtained a population with 102 nm (68%) and other with 339 nm, clearly evidencing signals of a fusion process, the FRET with DSPE-NBD obtained the results normally associated with MLPs: a small representative population, with 99% of the samples with 50 nm. In addition to confirming the absence of a fusion process with this fluorescence dye, this last result raises a question about the interaction between the MLPs and the LUVs with DSPE. With the absence of fusion, the expected results from the DLS would be two populations resembling both vesicles. However, by interpreting the results from the DLS, the DMPG LUVs were not present in the Rho_11 sample, at least in their previous size. To understand the impact of the lipid domain in the fusion, more studies addressing this are needed.

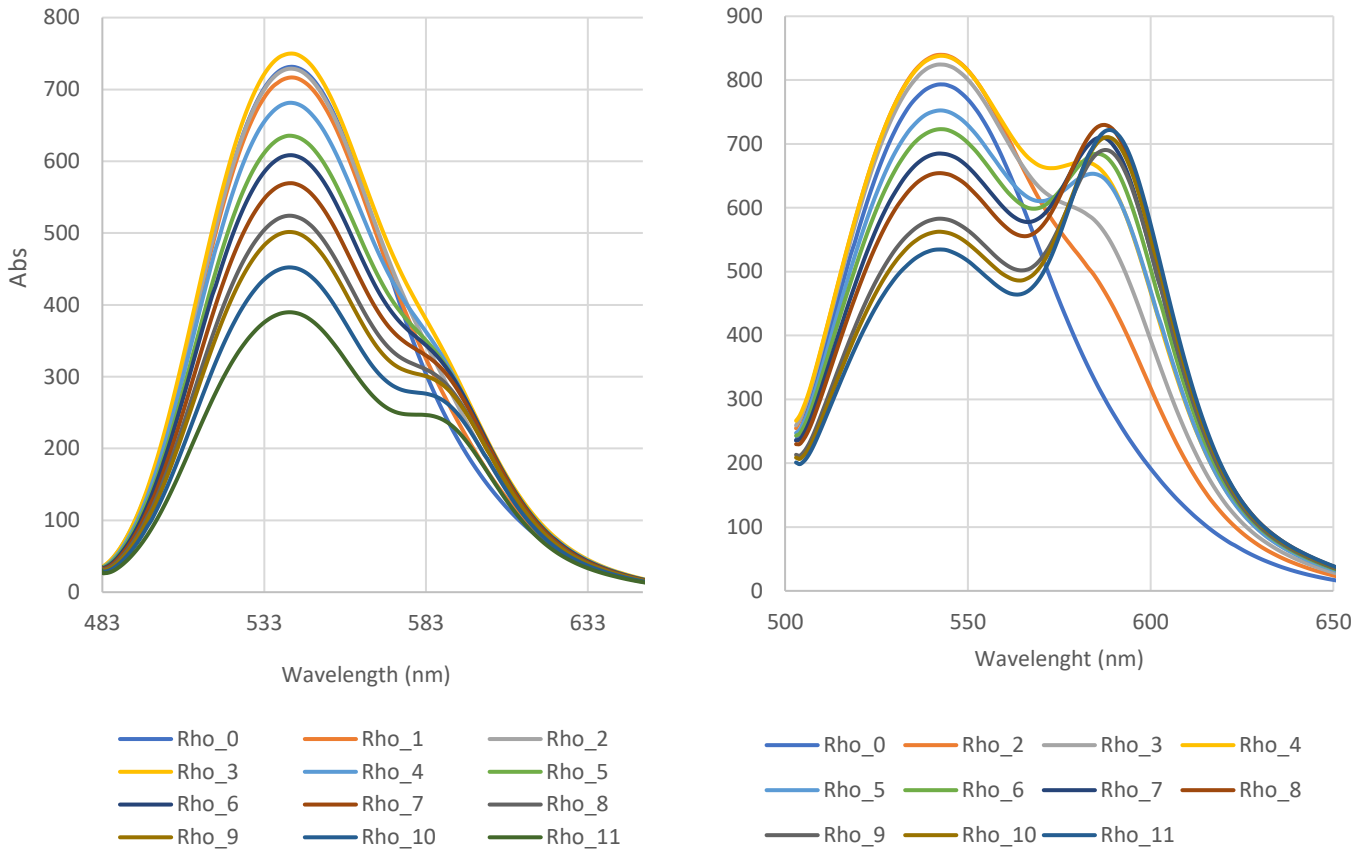

Figure 19 – FRET experiments with NBD with different lipidic environment. On the left, DSPE-NBD was the fluorescence dye used for the LUVs, whereas DPPE-NBD was used for the FRET on the right. The rhodamine peak is only visible on the FRET assay with DPPE-NBD.

Chapter 6

Conclusions and Future Works

6.1. Conclusions

Antibiotics resistance has become a major concern worldwide for the medical community and a rising issue for the public health in general, with *S. aureus* biofilms among the most resistant and also one of the most common causes of human bacterial infections. From the alternatives researched in the past decades, nanotechnology-based approaches are starting to provide efficient strategies to combat bacterial infections. One promising methodology is combining SPIONs – which recently showed antibacterial properties through magnetic hyperthermia but are very small in size and tend to aggregate, leading to cytotoxicity – with other nanosystems capable of reducing the drawbacks that SPIONs face. While it is possible to study the interaction between drugs and bacterial membranes using the bacteria itself, the research is time consuming and many times requires special work conditions. Additionally, the complexity and diversity presented by biological membranes originates a need for a more effective screening of new molecules and nanosystems. In this context, several biomimetic model membranes have been developed to overcome those barriers, with GUVs presenting a crucial role.

Thus, the aim of this work was to develop and optimize fusogenic liposomes loading SPIONs with suitable features for intravenous administration using a Box–Behnken design and then perform a preliminary evaluation of their fusogenic capacity using the GUVs model, also developed and optimized, through fluorescence microscopy and using DMPG:LUVs for FRET assays. One of the features of the formulation was the addition of a PEGylation, addressed at a preliminary level. The optimized formulation was characterized in size, polidispersity, encapsulation efficiency and phase transition temperature. The GUVs were prepared through an electroformation process with an automated device and their composition was intended to function as an approximation of the *S. aureus*.

The assay with PEG allowed to determine the percentage used for the remaining work, with 5% presenting the best mean size and PDI, only behind the formulation without PEG in the %EE. From there, the 3-factor, 3-level Box–Behnken experimental design was performed and the optimized formulation was obtained for a lipid concentration of 30 mM using 0.5 minutes of sonication time and 1.5 mL of SPIONs. The characterization confirmed the predicted results from the Minitab® software, with a mean size of 181.7 nm, a PDI of 0,202 and a representative population close to the 100 nm mark. For the phase transition, DLS measurements throughout a wide range of temperatures were performed and a well-defined sigmoid curve was verified, obtaining 37.9 ºC as the T_M for the optimized formulation.

From there, the GUVs were prepared and optimized, with the final condition being 10 mM as the lipid concentration, 900 mM for the D-sorbitol solution and a dilution of 1:3 after the electroformation. For the visualization, a drop of water improved the quality of images and an exposure time of 100 ms was, most of the times, the best decision for the 40x objective. Despite the permanent background, the morphology of the vesicles was promising.

The final step of this work was the preliminary evaluation of the fusogenic capacity with both models: with LUVs, a FRET efficiency of 26,5% was obtained; with GUVs, the fusion was observable by merging images from different channels. The results were very promising, with both models offering a good prospective for future works. Additionally, from the different NBD used in the last experiment, it was possible to observe the lack of fusion for the DSPE-NBD, demonstrating the impact of the membrane domain in the fusion.

6.2. Future Works

As highlighted throughout this work, a significant work still needs to be performed. And before developing future experiments to fully understand the fusogenic capacity of the magnetoliposomes developed, some improvements should be weighted. One of them is clearly referring to the background of GUVs, which was a significant limitation to the quality and definition of the obtained images. Therefore, to resolve this issue, one possible solution may

be replacing the rehydration solution, from D-sorbitol to sucrose, allowing to perform a sedimentation protocol, by adding glucose with the same concentration after the electroformation. The different molecular weight would result in the sedimentation of GUVs which in turn would improve the quality of the visualization under the microscope.

Additionally, some experiments should also be made to improve the results from the first phase of this work. For the characterization of the optimized formulation, other tests should be performed, to complete the information surrounding the nanosystem. For example, neither the colloidal stability nor the cytotoxicity results were developed. In fact, the latter was supposed to have been done, but some complications with schedules resulted in their transition to future work. The phase transition temperature should also be addressed again later, as the results were not enough to understand the impact of each variable. Moreover, the range of temperatures should also be increased, as well as the time of each measurement. If necessary, other methods could also be tested (DSC, FTIR, etc).

Regarding the magnetic properties of SPIONs, the addition of magnetisation experiments should be considered to understand the antimicrobial activity of the developed formulation and confirm the existence of superparamagnetic properties.

References

Afanasenkau, Dzmitry and Andreas Offenhäusser, 2012. "Positively Charged Supported Lipid Bilayers as a Biomimetic Platform for Neuronal Cell Culture" *Langmuir"*.

Akbarzadeh, Abolfazl *et al.,* 2013. "Liposome: Classification, Preparation, and Applications" *Nanoscale Research Letters* .

Akbarzadeh, Abolfazl, Mohamad Samiei and Soodabeh Davaran, 2012. "Magnetic Nanoparticles: Preparation, Physical Properties, and Applications in Biomedicine" *Nanoscale Research Letters* 7(144)

Angelova, Miglena I., and Dimiter S. Dimitrov, 1986. "Liposome Electroformation." *Faraday Discussion of the Chemical Society* (81): 303–11.

Archer, Nathan K. *et al.,* 2011. "*Staphylococcus Aureus* Biofilms Properties, Regulation and Roles in Human Disease" *Virulence* 2(5): 445–59.

Ariola, Florly S. *et al.,* 2009. "Membrane Fluidity and Lipid Order in Ternary Giant Unilamellar Vesicles Using a New Bodipy-Cholesterol Derivative" *Biophysical Journal* 96: 2696–2708.

Arleth, Lize and Charlotte Vermehren, 2010. "An Analytical Model for the Small-Angle Scattering of Polyethylene Glycol-Modified Liposomes" *Journal of Applied Crystallography* 43: 1084–91.

Askari, Alireza *et al.*, 2020. "Synthesis, Characterization and in Vitro Toxicity Evaluation of Doxorubicin-Loaded Magnetoliposomes on MCF-7 Breast Cancer Cell Line" *Journal of Drug Delivery Science and Technology* 55:101447.

Bagatolli, Luis A., and David Needham, 2014. "Quantitative Optical Microscopy and Micromanipulation Studies on the Lipid Bilayer Membranes of Giant Unilamellar Vesicles" *Chemistry and Physics of Lipids*: 99–120.

Bangham, A. D. 1993. "Liposomes: The Babraham Connection" *Chemistry and Physics of Lipids* 64(1–3): 275–85.

Bartelds, Rianne *et al.,* 2017. "Lipid Phase Separation in the Presence of Hydrocarbons in Giant Unilamellar Vesicles" *AIMS Biophysics* 4(4): 528–42.

Barthmes, Maria *et al.,* 2016. "Electrophysiological Characterization of the Archaeal Transporter NCX_Mj Using Solid Supported Membrane Technology." *Journal of General Physiology* 147(6): 485–96.

Baumgart, Tobias, Samuel T. Hess, and Watt W. Webb, 2003. "Imaging Coexisting Fluid Domains in Biomembrane Models Coupling Curvature and Line Tension." *Nature* 425(October): 821–24.

Beales, Paul A., Barbara Ciani, and Alexa J. Cleasby, 2015. "Nature's Lessons in Design: Nanomachines to Scaffold, Remodel and Shape Membrane Compartments." *Physical Chemistry Chemical Physics* 17(24): 15489–507.

Bhat, Anupama *et al.,* 2018. "Probing Interactions between AuNPs/AgNPs and Giant Unilamellar Vesicles (GUVs) Using Hyperspectral Dark-Field Microscopy" *International Journal of Molecular Sciences* 19(4).

Boyd, Margrethe A., and Neha P. Kamat, 2018. "Visualizing Tension and Growth in Model Membranes Using Optical Dyes" *Biophysical Journal* 115(7): 1307–15.

Bulte, Jeff W. M., Marcel De Cuyper, Daryl Despres, and Joseph A. Frank, 1999. "Preparation,

Relaxometry, and Biokinetics of PEGylated Magnetoliposomes as MR Contrast Agent" *Journal of Magnetism and Magnetic Materials* 194: 204–9.

Cardoso, Beatriz D., Irina S. R. Rio, Ana Rita O. Rodrigues, and Francisca C. T. Fernandes, 2018. "Magnetoliposomes Containing Magnesium Ferrite Nanoparticles as Nanocarriers for the Model Drug Curcumin" *Royal Society open Science* 5(181017).

Carvalho, A., M. B.F. Martins, M. L. Corvo, and G. Feio, 2014. "Enhanced Contrast Efficiency in MRI by PEGylated Magnetoliposomes Loaded with PEGylated SPION: Effect of SPION Coating and Micro-Environment" *Materials Science and Engineering C* 43: 521–26.

Carvalho, Kévin, Laurence Ramos, Christian Roy, and Catherine Picart, 2008. "Giant Unilamellar Vesicles Containing Phosphatidylinositol(4,5)Bisphosphate: Characterization and Functionality" *Biophysical Journal* 95(9): 4348–60.

Chan, Yee-Hung M., and Steven G. Boxer, 2007. "Model Membrane Systems and Their Applications" *Current Opinion in Chemical Biology* 11(6): 581–87.

Cheung, Herbert C., 2002. "Resonance Energy Transfer" In *Topics in Fluorescence Spectroscopy*, 127–34.

Ciobanasu, Corina, Agnieszka Rzeszutek, Ulrich Kubitscheck, and Regine Willumeit, 2015. "NKCS, a Mutant of the NK-2 Peptide, Causes Severe Distortions and Perforations in Bacterial, but Not Human Model Lipid Membranes" *Molecules* 20(4): 6941–58.

Da Costa E Silva, Rosangela M. F. *et al.*, 2018. "Preparation of Magnetoliposomes with a Green, Low-Cost, Fast and Scalable Methodology and Activity Study against *S. Aureus* and *C. Freundii* Bacterial Strains" *J. Braz. Chem. Soc* 29(12): 2636–45.

Cruje, Charmainne, and Devika B. Chithrani. 2014. "Polyethylene Glycol Functionalized Nanoparticles for Improved Cancer Treatment." *Reviews in Nanoscience and Nanotechnology* 3(1): 20–30.

Dao, T. P.T. *et al.*, 2017. "Membrane Properties of Giant Polymer and Lipid Vesicles Obtained by Electroformation and Pva Gel-Assisted Hydration Methods" *Colloids and Surfaces A: Physicochemical and Engineering Aspects* 533(September): 347–53.

Dimova, Rumiana, 2012. "Giant Vesicles: A Biomimetic Tool for Membrane Characterization" In *Advances in Planar Lipid Bilayers and Liposomes* 1st ed. Elsevier Inc.

Dimova, Rumina (Ed.), Carlos M. (Ed.) Marques, Pasquale Stano, and Peter Walde, 2019. "Preparation methods for giant unilamellar vesicles" In *The Giant Vesicle Book*.

Drabik, Dominik, Joanna Doskocz, and Magda Przybyło, 2018. "Effects of Electroformation Protocol Parameters on Quality of Homogeneous GUV Populations" *Chemistry and Physics of Lipids* 212(November 2017): 88–95.

Drulis-Kawa, Zuzanna, and Agata Dorotkiewicz-Jach, 2010. "Liposomes as Delivery Systems for Antibiotics" *International Journal of Pharmaceutics* 387(1–2): 187–98.

Faria, M. R. *et al.*, 2013. "Synthesis and Characterization of Magnetoliposomes for MRI Contrast Enhancement" *International Journal of Pharmaceutics* 446(1–2): 183–90.

Fenz, Susanne F., and Kheya Sengupta, 2012. "Giant Vesicles as Cell Models" *Integrative Biology (United Kingdom)* 4(9): 982–95.

Ferreira, S. L.C. *et al.*, 2007. "Box-Behnken Design: An Alternative for the Optimization of Analytical Methods" *Analytica Chimica Acta* 597(2): 179–86.

Filipa Soares, 2019. "Development of Hybrid Nanosystems Based on Membrane Lipids as SPIONs Nanocarriers for *Staphylococcus Aureus* Biofilms Disruption"

Forier, Katrien *et al.*, 2014. "Lipid and Polymer Nanoparticles for Drug Delivery to Bacterial Biofilms" *Journal of Controlled Release* 190: 607–23.

Freeman, M. W., A. Arrott, and J. H. L. Watson, 1960. "Magnetism in Medicine" 404(May 2013): 127–29.

Garbuzenko, Olga, Yechezkel Barenholz, and Aba Priev, 2005. "Effect of Grafted PEG on Liposome Size and on Compressibility and Packing of Lipid Bilayer" *Chemistry and Physics of Lipids* 135(2): 117–29.

García-Sáez, Ana J., and Petra Schwille, 2008. "Fluorescence Correlation Spectroscopy for the Study of Membrane Dynamics and Protein / Lipid Interactions" *Methods* 46: 116–22.

Garcia Ribeiro, Rita Sofia *et al.,* 2018. "Magnetoliposomes as Contrast Agents for Longitudinal in Vivo Assessment of Transplanted Pancreatic Islets in a Diabetic Rat Model" *Scientific Reports* 8(1): 1–12.

Gholami, Leila *et al.,* 2018. "Green Facile Synthesis of Low-Toxic Superparamagnetic Iron Oxide Nanoparticles (SPIONs) and Their Cytotoxicity Effects toward Neuro2A and HUVEC Cell Lines" *Ceramics International* 44(8): 9263–68.

Gonzalez-Moragas, Laura *et al.,* 2015. "Scale-up Synthesis of Iron Oxide Nanoparticles by Microwave-Assisted Thermal Decomposition" *Chemical Engineering Journal* 281: 87–95.

Gu, Bing *et al.,* 2013. "The Emerging Problem of Linezolid-Resistant *Staphylococcus*" *Journal of Antimicrobial Chemotherapy* 68: 4–11.

Guo, Hongyan *et al.,* 2015. "Theranostic Magnetoliposomes Coated by Carboxymethyl Dextran with Controlled Release by Low-Frequency Alternating Magnetic Field" *Carbohydrate Polymers* 118: 209–17.

Hall-Stoodley, Luanne, J. William Costerton, and Paul Stoodley, 2004. "Bacterial Biofilms: From the Natural Environment to Infectious Diseases" *Nature Reviews Microbiology* 2(2): 95–108.

Harbich, W., and W. Helfrich, 1979. "Alignment and Opening of Giant Lecithin Vesicles by Electric Fields" *Zeitschrift fur Naturforschung - Section A Journal of Physical Sciences* 34(9): 1063–65.

Hasan, Nurhasni *et al.,* 2019. "PEI/NONOates-Doped PLGA Nanoparticles for Eradicating Methicillin-Resistant *Staphylococcus Aureus* Biofilm in Diabetic Wounds via Binding to the Biofilm Matrix" *Materials Science and Engineering C* 103(December 2018): 109741.

Heuvingh, J., F. Pincet, and S. Cribier, 2004. "Hemifusion and Fusion of Giant Vesicles Induced by Reduction of Inter-Membrane Distance" *The European Physical Journal* 14: 269–76.

Hochreiter, Bernhard, Alan Pardo Garcia, and Johannes A. Schmid, 2015. "Fluorescent Proteins as Genetically Encoded FRET Biosensors in Life Sciences" *Sensors (Switzerland)* 15(10): 26281–314.

Hu, Xiaohui, and Kin Tam, 2017. "Biomembrane Mimics and Their Roles in Anti-Bacterial Drug Discovery" *ADMET and DMPK* 5(1): 9–13.

Joniec, Aleksandra, Slawomir Sek, and Pawel Krysinski, 2016. "Magnetoliposomes as Potential Carriers of Doxorubicin to Tumours" *Chemistry - A European Journal* 22(49): 17715–24.

Juhasz, Janos, Frances J. Sharom, and James H. Davis, 2009. "Quantitative Characterization of Coexisting Phases in DOPC/DPPC/Cholesterol Mixtures: Comparing Confocal Fluorescence Microscopy and Deuterium Nuclear Magnetic Resonance." *Biochimica et Biophysica Acta - Biomembranes* 1788(12): 2541–52.

Kahveci, Zehra, and Stefano Pagliara, 2018. "Giant Unilamellar Vesicles (GUVs) Preparation by Electroformation Method." *protocols.io* (July).

Kanafani, Zeina A., and Vance G. Fowler, 2006. "*Staphylococcus Aureus* Infections: New Challenges from an Old Pathogen" *Enfermedades Infecciosas y Microbiologia Clinica* 24(3): 182–93.

Kandasamy, Ganeshlenin *et al.,* 2018. "Systematic Investigations on Heating Effects of Carboxyl-Amine Functionalized Superparamagnetic Iron Oxide Nanoparticles (SPIONs) Based Ferrofluids for in Vitro Cancer Hyperthermia Therapy" *Journal of Molecular Liquids* 256: 224–37.

Kandasamy, Ganeshlenin, and Dipak Maity, 2015. "Recent Advances in Superparamagnetic Iron Oxide Nanoparticles (SPIONs) for in Vitro and in Vivo Cancer Nanotheranostics" *International Journal of Pharmaceutics* 496(2): 191–218.

Kao, Pei Hsiu, Shinne Ren Lin, Wan Ping Hu, and Long Sen Chang, 2012. "Naja Naja Atra and Naja Nigricollis Cardiotoxins Induce Fusion of *Escherichia Coli* and *Staphylococcus Aureus* Membrane-Mimicking Liposomes" *Toxicon* 60(3): 367–77.

Kiessling, Volker, Sung Tae Yang, and Lukas K. Tamm, 2015. "Supported Lipid Bilayers as Models for Studying Membrane Domains" In *Current Topics in Membranes* Elsevier Ltd.

Klaerke, Dan A. *et al.,* 2018. "Reconstitution and Electrophysiological Characterization of Ion Channels in Lipid Bilayers" *Current Protocols in Pharmacology* 81(1): 1–17.

Klymchenko, Andrey S. *et al.,* 2009. "Visualization of Lipid Domains in Giant Unilamellar Vesicles Using an Environment-Sensitive Membrane Probe Based on 3-Hydroxyflavone" *BBA - Biomembranes* 1788: 495–99.

Koo, Khong Nee, Ahmad Fauzi Ismail, Modh Othman, and Mukhlis Rahman, 2019. "Preparation and Characterization of Superparamagnetic Magnetite (Fe3O4) Nanoparticles: A Short Review" *Malaysian Journal of Fundamental and Applied Sciences* 15(1): 23–31.

Kreutzberger, Mark A., Antje Pokorny, and Paulo F. Almeida, 2017. "Daptomycin-Phosphatidylglycerol Domains in Lipid Membranes" *Langmuir* 33(47): 13669–79.

Labruère, Raphaël, A. J. Sona, and Edward Turos, 2019. "Anti–Methicillin-Resistant *Staphylococcus Aureus* Nanoantibiotics" *Frontiers in Pharmacology* 10(October): 1–24.

Laurent, Sophie, Silvio Dutz, Urs O. Häfeli, and Morteza Mahmoudi, 2011. "Magnetic Fluid Hyperthermia: Focus on Superparamagnetic Iron Oxide Nanoparticles" *Advances in Colloid and Interface Science* 166(1–2): 8–23.

Li, Hewen, Tao Zhao, and Zhihua Sun, 2018. "Analytical Techniques and Methods for Study of Drug-Lipid Membrane Interactions" *Reviews in Analytical Chemistry* 37(1): 1–23.

Lira, Rafael B., Tom Robinson, Rumiana Dimova, and Karin A. Riske, 2019. "Highly Efficient Protein-Free Membrane Fusion: A Giant Vesicle Study" *Biophysical Journal* 116(1): 79–91.

Lister, Jessica L., and Alexander R. Horswill, 2014. "*Staphylococcus Aureus* Biofilms: Recent Developments in Biofilm Dispersal" *Frontiers in Cellular and Infection Microbiology* 4(178).

Liu, Xiaolong *et al.,* 2007. "Using Giant Unilamellar Lipid Vesicle Micro-Patterns as Ultrasmall Reaction Containers to Observe Reversible ATP Synthesis / Hydrolysis of F0F1-ATPase Directly" *Biochimica et Biophysica Acta* 1770: 1620–26.

Long, M Scott *et al.,* 2005. "Dynamic Microcompartmentation in Synthetic Cells" *PNAS* 102(17): 5920–25.

Magnani, C. *et al.,* 2018. "Hybrid Vesicles from Lipids and Block Copolymers: Phase Behavior from the Micro- to the Nano-Scale" *Colloids and Surfaces B: Biointerfaces* 168: 18–28.

Mahmoudi, M., A. Simchi, A. S. Milani, and P. Stroeve, 2009. "Cell Toxicity of Superparamagnetic Iron Oxide Nanoparticles" *Journal of Colloid and Interface Science* 336(2): 510–18.

Mahmoudi, Morteza *et al.,* 2011. "Superparamagnetic Iron Oxide Nanoparticles (SPIONs): Development, Surface Modification and Applications in Chemotherapy" *Advanced Drug Delivery Reviews* 63(1–2): 24–46.

Mahmoudi, Morteza, Heinrich Hofmann, Barbara Rothen-Rutishauser, and Alke Petri-Fink, 2012. "Assessing the In Vitro and In Vivo Toxicity of Superparamagnetic Iron Oxide Nanoparticles" *Chemical Reviews* 112: 2323–38.

Majetich, Sara A., Tianlong Wen, and O. Thompson Mefford, 2013. "Magnetic Nanoparticles" *MRS Bulletin*

38(11): 899–903.

Martins, M. Bárbara A.F. *et al.,* 2014. "New Long Circulating Magnetoliposomes as Contrast Agents for Detection of Ischemia-Reperfusion Injuries by MRI" *Nanomedicine: Nanotechnology, Biology, and Medicine* 10(1): 207–14.

Matos, Carla, Carla Moutinho, and Paulo Loba, 2012. "Liposomes as a Model for the Biological Membrane : Studies on Daunorubicin Bilayer Interaction" *Journal of Membrane Biology* 245: 69–75.

Mcguinness, Will A., Natalia Malachowa, and Frank R. Deleo, 2017. "Vancomycin Resistance in *Staphylococcus Aureus*" *Yale Journal of Biology and Medicine* 90: 269–81.

Medintz, Igor, and Niko Hildebrandt, 2014. *FRET - " How to Apply FRET: From Experimental Design to Data Analysis" In Förster Resonance Energy Transfer: From Theory to Applications, First Edition*.

Merkle, Dennis, Nicoletta Kahya, and Petra Schwille, 2008. "Reconstitution and Anchoring of Cytoskeleton inside Giant Unilamellar Vesicles" *ChemBioChem* 9: 2673–81.

Michel, Nicolas *et al.,* 2006. "Determination of Phase Transition Temperatures of Lipids by Light Scattering" *Chemistry and Physics of Lipids* 139: 11–19.

Mohammed, Yasser Hussein Eissa *et al.,* 2018. "Vision for Medicine: *Staphylococcus Aureus* Biofilm War and Unlocking Key's for Anti-Biofilm Drug Development" *Microbial Pathogenesis* 123: 339–47.

Mohanan, Gayathri, Karthika S. Nair, K. Madhavan Nampoothiri, and Harsha Bajaj, 2020. "Engineering Bio-Mimicking Functional Vesicles with Multiple Compartments for Quantifying Molecular Transport" *Chemical Science*.

Monnier, Christophe A. *et al.,* 2014. "Magnetoliposomes: Opportunities and Challenges" *European Journal of Nanomedicine* 6(4): 201–15.

Montes, L. Ruth, Alicia Alonso, Felix M. Goñi, and Luis A. Bagatolli, 2007. "Giant Unilamellar Vesicles Electroformed from Native Membranes and Organic Lipid Mixtures under Physiological Conditions" *Biophysical Journal* 93(10): 3548–54.

Moormeier, Derek E., and Kenneth W. Bayles, 2017. "*Staphylococcus Aureus* Biofilm: A Complex Developmental Organism" *Molecular Microbiology* 104(3): 365–76.

Moreira, Wallance *et al.,* 2019. "Interaction of Artepillin C with Model Membranes : Effects of PH and Ionic" *BBA - Biomembranes* 1861: 410–17.

Musielak, Marika, Igor Piotrowski, and Wiktoria M. Suchorska, 2019. "Superparamagnetic Iron Oxide Nanoparticles (SPIONs) as a Multifunctional Tool in Various Cancer Therapies" *Reports of Practical Oncology and Radiotherapy* 24(4): 307–14.

Al Nahas, K. *et al.,* 2019. "Lab on a Chip: A Microfluidic Platform for the Characterisation of Membrane Active Antimicrobials" *Lab Chip* 19: 837–44.

Neves, A. R., Cláudia Nunes, H. Amenitsch, and Sallete Reis, 2016. "Effects of Resveratrol on the Structure and Fluidity of Lipid Bilayers: A Membrane Biophysical Study" *Soft Matter* 12(7): 2118–26.

Nguyen, Thuy Khanh *et al.,* 2015. "Iron Oxide Nanoparticle-Mediated Hyperthermia Stimulates Dispersal in Bacterial Biofilms and Enhances Antibiotic Efficacy" *Scientific Reports* 5(November): 1–15.

Nicolosi, Daria, Marina Scalia, Vito M. Nicolosi, and Rosario Pignatello, 2010. "Encapsulation in Fusogenic Liposomes Broadens the Spectrum of Action of Vancomycin against Gram-Negative Bacteria" *International Journal of Antimicrobial Agents* 35(6): 553–58.

Nuytten, N. *et al.,* 2010. "PEGylated Lipids Impede the Lateral Diffusion of Adsorbed Proteins at the Surface of (Magneto)Liposomes" *Colloids and Surfaces B: Biointerfaces* 80(2): 227–31.

Oglęcka, Kamila *et al.,* 2014. "Oscillatory Phase Separation in Giant Lipid Vesicles Induced by Transmembrane Osmotic Differentials" *eLife* 3: 1–18.

Ostroumova, Olga S., Evgeny G. Chulkov, Olga V. Stepanenko, and Ludmila V. Schagina, 2014. "Effect of Flavonoids on the Phase Separation in Giant Unilamellar Vesicles Formed from Binary Lipid Mixtures" *Chemistry and Physics of Lipids* 178: 77–83.

Park, Hongsuk *et al.,* 2011. "Inactivation of *Pseudomonas Aeruginosa* PA01 Biofilms by Hyperthermia Using Superparamagnetic Nanoparticles" *Journal of Microbiological Methods* 84(1): 41–45.

Pathak, Priyadarshini, and Erwin London, 2015. "The Effect of Membrane Lipid Composition on the Formation of Lipid Ultrananodomains" *Biophysical Journal* 109(8): 1630–38.

Patil, Rakesh M. *et al.,* 2018. "Comprehensive Cytotoxicity Studies of Superparamagnetic Iron Oxide Nanoparticles" *Biochemistry and Biophysics Reports* 13: 63–72.

Peetla, Chiranjeevi, Andrew Stine, and Vinod Labhasetwar, 2009. "Biophysical Interactions with Model Lipid Membranes: Applications in Drug Discovery and Drug Delivery" *Molecular Pharmaceutics* 6(5): 1264–76.

Peterlin, Primoz *et al.,* 2009. "Growth and Shape Transformations of Giant Phospholipid Vesicles upon Interaction with an Aqueous Oleic Acid Suspension" *Chemistry and Physics of Lipids* 159: 67–76.

Pinheiro, Marina *et al.,* 2013. "The Influence of Rifabutin on Human and Bacterial Membrane Models : Implications for Its Mechanism of Action" *The Journal of Physical Chemistry* 117: 6187–93.

Pinto, Rita M. *et al.,* 2019. "Impact of Nanosystems in *Staphylococcus Aureus* Biofilms Treatment" *FEMS Microbiology Reviews* 43(6): 622–41.

Pinto, Rita M. *et al.,* 2020. "Innovative Strategies Toward the Disassembly of the EPS Matrix in Bacterial Biofilms" *Frontiers in Microbiology* 11(952).

Del Pozo, Jose Luis, 2018. "Biofilm-Related Disease" *Expert Review of Anti-Infective Therapy* 16(1): 51–65.

Ramundo-Orlando, Alfonsina *et al.,* 2009. "The Response of Giant Phospholipid Vesicles to Millimeter Waves Radiation" *Biochimica et Biophysica Acta - Biomembranes* 1788(7): 1497–1507.

Reeves, John P., and Robert M. Dowben, 1969. "Formation and Properties of Thin-walled Phospholipid Vesicles" *Journal of Cellular Physiology* 73(1): 49–60.

Rideau, Emeline, Frederik R. Wurm, and Katharina Landfester, 2019. "Self-Assembly of Giant Unilamellar Vesicles by Film Hydration Methodologies" *Advanced Biosystems* 3(6): 1–13.

Rodi, Pablo M., Bruno Maggio, and Luis A. Bagatolli, 2018. "Direct Visualization of the Lateral Structure of Giant Vesicles Composed of Pseudo-Binary Mixtures of Sulfatide, Asialo-GM1 and GM1 with POPC" *Biochimica et Biophysica Acta - Biomembranes* 1860(2): 544–55.

Rodriguez, Nicolas, Frédéric Pincet, and Sophie Cribier, 2005. "Giant Vesicles Formed by Gentle Hydration and Electroformation: A Comparison by Fluorescence Microscopy" *Colloids and Surfaces B: Biointerfaces* (42): 125–30.

Rost, N. C.V. *et al.,* 2020. "Magnetic Particle Imaging Performance of Liposomes Encapsulating Iron Oxide Nanoparticles" *Journal of Magnetism and Magnetic Materials* 504.

Roux, Aurélien *et al.,* 2005. "Role of Curvature and Phase Transition in Lipid Sorting and Fission of Membrane Tubules" *EMBO Journal* 24(8): 1537–45.

Rukavina, Zora, and Željka Vanic, 2016. "Current Trends in Development of Liposomes for Targeting Bacterial Biofilms" *Pharmaceutics* 8(18).

Sabat, Artur J. *et al.,* 2018. "Daptomycin Resistant *Staphylococcus Aureus* Clinical Strain With Novel Non-Synonymous Mutations in the MprF and VraS Genes : A New Insight Into Daptomycin Resistance" *Frontiers in Microbiology* 9(2705).

Saito, Hirohide *et al.,* 2009. "Time-Resolved Tracking of a Minimum Gene Expression System Reconstituted

in Giant Liposomes" *ChemBioChem* 10: 1640–43.

Sani, M. A. *et al.,* 2013. "Maculatin 1.1 Disrupts *Staphylococcus Aureus* Lipid Membranes via a Pore Mechanism" *Antimicrobial Agents and Chemotherapy* 57(8): 3593–3600.

Schindelin, Johannes *et al.,* 2012. "Fiji : An Open-Source Platform for Biological-Image Analysis" *Nature Methods* 9(7): 676–82.

Scriboni, Andreia Borges *et al.,* 2019. "Fusogenic Liposomes Increase the Antimicrobial Activity of Vancomycin against *Staphylococcus Aureus* Biofilm" *Frontiers in Pharmacology* 10(November): 1–11.

Seabra, Amedea B., Milena T. Pelegrino, and Paula S. Haddad, 2017. "Antimicrobial Applications of Superparamagnetic Iron Oxide Nanoparticles: Perspectives and Challenges" In *Nanostructures for Antimicrobial Therapy: Nanostructures in Therapeutic Medicine Series*, Elsevier, 531–50.

Shen, Zhiqiang, Alessandro Fisher, Wing K. Liu, and Ying Li, 2018. "PEGylated "Stealth" Nanoparticles and Liposomes" In *Engineering of Biomaterials for Drug Delivery Systems: Beyond Polyethylene Glycol* Elsevier Ltd.

Shimanouchi, Toshinori *et al.,* 2007. "Permeation of a ß-Heptapeptide Derivative across Phospholipid Bilayers" *Biochimica et Biophysica Acta* 1768: 2726–36.

Shirmardi Shaghasemi, Behzad, Mudassar Mumtaz Virk, and Erik Reimhult, 2017. "Optimization of Magneto-Thermally Controlled Release Kinetics by Tuning of Magnetoliposome Composition and Structure" *Scientific Reports* 7(1): 1–10.

Singh, Neenu, Gareth J. S. Jenkins, Romisa Asadi, and Shareen H. Doak, 2010. "Potential Toxicity of Superparamagnetic Iron Oxide Nanoparticles (SPION)" *Nano Reviews* 1(5358).

Sohlenkamp, Christian, and Otto Geiger, 2016. "Bacterial Membrane Lipids : Diversity in Structures and Pathways" *FEMS Microbiology Reviews* 40(1): 133–59.

Soranzo, Thomas *et al.,* 2016. "Functional Characterization of P7 Viroporin from Hepatitis C Virus Produced in a Cell-Free Expression System" *Protein Expression and Purification* 118: 83–91.

Steinkühler, Jan *et al.,* 2018. "Charged Giant Unilamellar Vesicles Prepared by Electroformation Exhibit Nanotubes and Transbilayer Lipid Asymmetry" *Scientific Reports* 8(1): 1–9.

Stetefeld, Jörg, Sean A. Mckenna, and Trushar R. Patel, 2016. "Dynamic Light Scattering : A Practical Guide and Applications in Biomedical Sciences" *Biophysical Reviews* 8: 409–27.

Subbiahdoss, Guruprakash *et al.,* 2012. "Magnetic Targeting of Surface-Modified Superparamagnetic Iron Oxide Nanoparticles Yields Antibacterial Efficacy against Biofilms of Gentamicin-Resistant *Staphylococci*" *Acta Biomaterialia* 8(6): 2047–55.

Suk, Jung Soo *et al.,* 2016. "PEGylation as a Strategy for Improving Nanoparticle-Based Drug and Gene Delivery" *Advanced Drug Delivery Reviews* 99: 28–51.

Tamba, Yukihiro, and Masahito Yamazaki, 2009. "Magainin 2-Induced Pore Formation in the Lipid Membranes Depends on Its Concentration in the Membrane Interface" *Journal of Physical Chemistry B* 113(14): 4846–52.

Tamm, L. K., 1984. "The Substrate Supported Lipid Bilayer - a New Model Membrane System" *Klinische Wochenschrift* 62: 502–3.

Tamm, L. K., and H. M. McConnell, 1985. "Supported Phospholipid Bilayers" *Biophysical Journal* 47(1): 105–13.

Taylor, Erik N. *et al.,* 2012. "Superparamagnetic Iron Oxide Nanoparticles (SPION) for the Treatment of Antibiotic-Resistant Biofilms" *Small* 8(19): 3016–27.

Trier, Sofie, Jonas R. Henriksen, and Thomas L. Andresen, 2011. "Membrane Fusion of PH-Sensitive

Liposomes - A Quantitative Study Using Giant Unilamellar Vesicles" *Soft Matter* 7(19): 9027–34.

Vial, F., F. Cousin, L. Bouteiller, and C. Tribet, 2009. "Rate of Permeabilization of Giant Vesicles by Amphiphilic Polyacrylates Compared to the Adsorption of These Polymers onto Large Vesicles and Tethered Lipid Bilayers" *Langmuir* 25(13): 7506–13.

Vitkova, V., M. Mader, and T. Podgorski, 2004. "Deformation of Vesicles Flowing through Capillaries" *Europhysics Letters* 68(3): 398–404.

Walde, Peter, Katia Cosentino, Helen Engel, and Pasquale Stano, 2010. "Giant Vesicles: Preparations and Applications" *ChemBioChem* 11(7): 848–65.

Wang, Zhao *et al.*, 2016. "Fusion between Fluid Liposomes and Intact Bacteria: Study of Driving Parameters and in Vitro Bactericidal Efficacy" *International Journal of Nanomedicine* 11: 4025–36.

Weinberger, Andreas *et al.*, 2013. "Gel-Assisted Formation of Giant Unilamellar Vesicles" *Biophysical Journal* 105(1): 154–64.

Zhang, Zhi Qiang, and Soo Chang Song, 2017. "Multiple Hyperthermia-Mediated Release of TRAIL/SPION Nanocomplex from Thermosensitive Polymeric Hydrogels for Combination Cancer Therapy" *Biomaterials* 132: 16–27.

Supplementary Information

Table SI 1 - Iron Quantification in the PEG Percentage Assay

	Fe^{2+} Quantification	SPIONs	0,5% PEG	2% PEG	5% PEG	Without PEG
A1	*Preparation*	256	40	40	40	48
	Quantification	10	20	20	20	20
	Total Dilution factor	2560	800	800	800	960
	Abs 511 nm	0.2051	0.3932	0.4244	0.5175	0.4617
	[Fe] sample (mg/l)	0.944	1.852	2.003	2.452	2.183
	[Fe] initial (mg/l)	2417	1482	1602	1962	2096
A2	*Preparation*	256	40	40	40	48
	Quantification	10	10	10	10	10
	Total Dilution factor	2560	400	400	400	480
	Abs 511 nm	0.2106	0.8011	0.8115	0.9865	0.8724
	[Fe] sample (mg/l)	0.971	3.822	3.872	4.717	4.166
	[Fe] initial (mg/l)	2485	1529	1549	1887	2000
A3	*Preparation*	256	40	40	40	48
	Quantification	10	10	10	10	10
	Total Dilution factor	2560	400	400	400	480
	Abs 511 nm	0.2051	0.8033	0.7991	0.9742	0.8646
	[Fe] sample (mg/l)	0.944	3.833	3.812	4.658	4.128
	[Fe] initial (mg/l)	2417	1533	1525	1863	1982

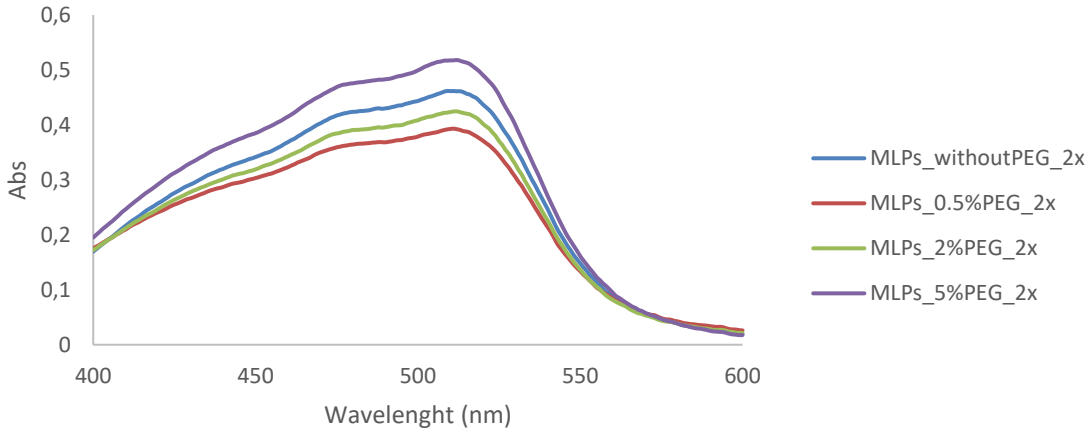

Figure SI 1 - Schematic representation of the results for the preliminary assay to determine the PEG percentage

Table SI 2 - Box-Behnken experimental results for encapsulation efficiency

Exp. Runs	Lipid Concentration (mM)	SPIONs Volume (mL)	Sonication Time (min)	Dilution Factor Preparation	Dilution Factor Quantification	Total Dilution Factor	Abs 511 nm	[Fe] sample (mg/L)	[Fe] initial (mg/L)	%EE
R1	10	0.5	1.5	40	20	800	0.476	2.252	1801.5	58.5
R2	30	0.5	1.5	48	20	960	0.540	2.563	2460.7	79.8
R3	10	1.5	1.5	16	40	640	0.840	4.011	2567.0	83.3
R4	30	1.5	1.5	16	20	320	1.375	6.595	2110.4	68.5
R5	10	1.0	0.5	24	20	480	0.936	4.475	2148.2	69.7
R6	30	1.0	0.5	24	20	480	1.021	4.883	2343.9	76.1
R7	10	1.0	2.5	24	20	480	1.077	5.152	2473.1	80.2
R8	30	1.0	2.5	24	20	480	0.913	4.361	2093.3	67.9
R9	20	0.5	0.5	48	20	960	0.668	3.180	3052.8	99.1
R10	20	1.5	0.5	16	20	320	1.629	7.818	2501.7	81.2
R11	20	0.5	2.5	48	20	960	0.369	1.735	1665.2	54.0
R12	20	1.5	2.5	16	20	320	1.489	7.143	2285.8	74.2
R13	20	1.0	1.5	24	20	480	1.176	5.630	2702.5	87.7
R14	20	1.0	1.5	24	20	480	1.150	5.509	2644.2	85.8
R15	20	1.0	1.5	24	20	480	1.190	5.701	2736.5	88.8

Table SI 3 - Percentage of the Representative Population

Experimental Runs	Mean Size (nm)	Representative Population (nm)	% Representative Population
R1	176.9	72.2	98
R2	141.0	62.4	98
R3	356.2	102.9	97
R4	191.8	72.9	97
R5	180.1	61.7	99
R6	162.3	59.0	99
R7	362.2	78.2	33
R8	165.9	77.1	98
R9	144.2	59.2	99
R10	213.0	115.7	32
R11	150.0	57.0	99
R12	292.8	108.4	99
R13	127.8	69.9	99
R14	181.7	73.7	98
R15	187.1	73.7	94

Response Surface Regression: Representative Pop. (nm) versus Lipid Concentration (mM); SPIONs Volume (mL); Sonication Time (min)

Source	DF	Adj SS	Adj MS	F-Value	P-Value
Model	2	3217,20	1608,60	12,62	0,001
Linear	1	2776,24	2776,24	21,79	0,001
SPIONs Volume (mL)	1	2776,24	2776,24	21,79	0,001
Square	1	440,96	440,96	3,46	0,088
SPIONs Volume (mL)*SPIONs Volume (mL)	1	440,96	440,96	3,46	0,088
Error	12	1529,17	127,43		
Lack-of-Fit	10	1519,44	151,94	31,24	0,031
Pure Error	2	9,73	4,86		
Total	14	4746,37			

R-sq	R-sq(adj)	R-sq(pred)
67,78%	62,41%	45,65%

Response Surface Regression: Minority Pop. (nm) versus Lipid Concentration (mM); SPIONs Volume (mL); Sonication Time (min)

Source	DF	Adj SS	Adj MS	F-Value	P-Value
Model	3	92109	30703	9,95	0,002
Linear	3	92109	30703	9,95	0,002
Lipid Concentration (mM)	1	18729	18729	6,07	0,031
SPIONs Volume (mL)	1	61422	61422	19,91	0,001
Sonication Time (min)	1	11958	11958	3,88	0,075
Error	11	33931	3085		
Lack-of-Fit	9	22712	2524	0,45	0,836
Pure Error	2	11219	5609		
Total	14	126040			

R-sq	R-sq(adj)	R-sq(pred)
73,08%	65,74%	51,80%

Response Surface Regression: PDI versus Lipid Concentration (mM); SPIONs Volume (mL); Sonication Time (min)

Source	DF	Adj SS	Adj MS	F-Value	P-Value
Model	4	0,016868	0,004217	14,60	0,000
Linear	3	0,014932	0,004977	17,23	0,000
Lipid Concentration (mM)	1	0,004232	0,004232	14,65	0,003
SPIONs Volume (mL)	1	0,002888	0,002888	10,00	0,010
Sonication Time (min)	1	0,007812	0,007812	27,05	0,000
2-Way Interaction	1	0,001936	0,001936	6,70	0,027
SPIONs Volume (mL)*Sonication Time (min)	1	0,001936	0,001936	6,70	0,027
Error	10	0,002888	0,000289		
Lack-of-Fit	8	0,002496	0,000312	1,59	0,442
Pure Error	2	0,000392	0,000196		
Total	14	0,019757			

R-sq	R-sq(adj)	R-sq(pred)
85,38%	79,53%	57,03%

Response Surface Regression: %EE versus Lipid Concentration (mM); SPIONs Volume (mL); Sonication Time (min)

Source	DF	Adj SS	Adj MS	F-Value	P-Value
Model	4	0,12686	0,03172	4,45	0,025
Linear	1	0,03078	0,03078	4,32	0,064
Sonication Time (min)	1	0,03078	0,03078	4,32	0,064
Square	1	0,02717	0,02717	3,81	0,080
Lipid Concentration (mM)*Lipid Concentration (mM)	1	0,02717	0,02717	3,81	0,080
2-Way Interaction	2	0,06891	0,03446	4,83	0,034
Lipid Concentration (mM)*SPIONs Volume (mL)	1	0,03278	0,03278	4,60	0,058
SPIONs Volume (mL)*Sonication Time (min)	1	0,03614	0,03614	5,07	0,048
Error	10	0,07131	0,00713		
Lack-of-Fit	8	0,07085	0,00886	38,60	0,025
Pure Error	2	0,00046	0,00023		
Total	14	0,19818			

R-sq	R-sq(adj)	R-sq(pred)
64,01%	49,62%	2,34%

Figure SI 2 - Statistical impact of each term in the remaining variables, with the R^2 on the right

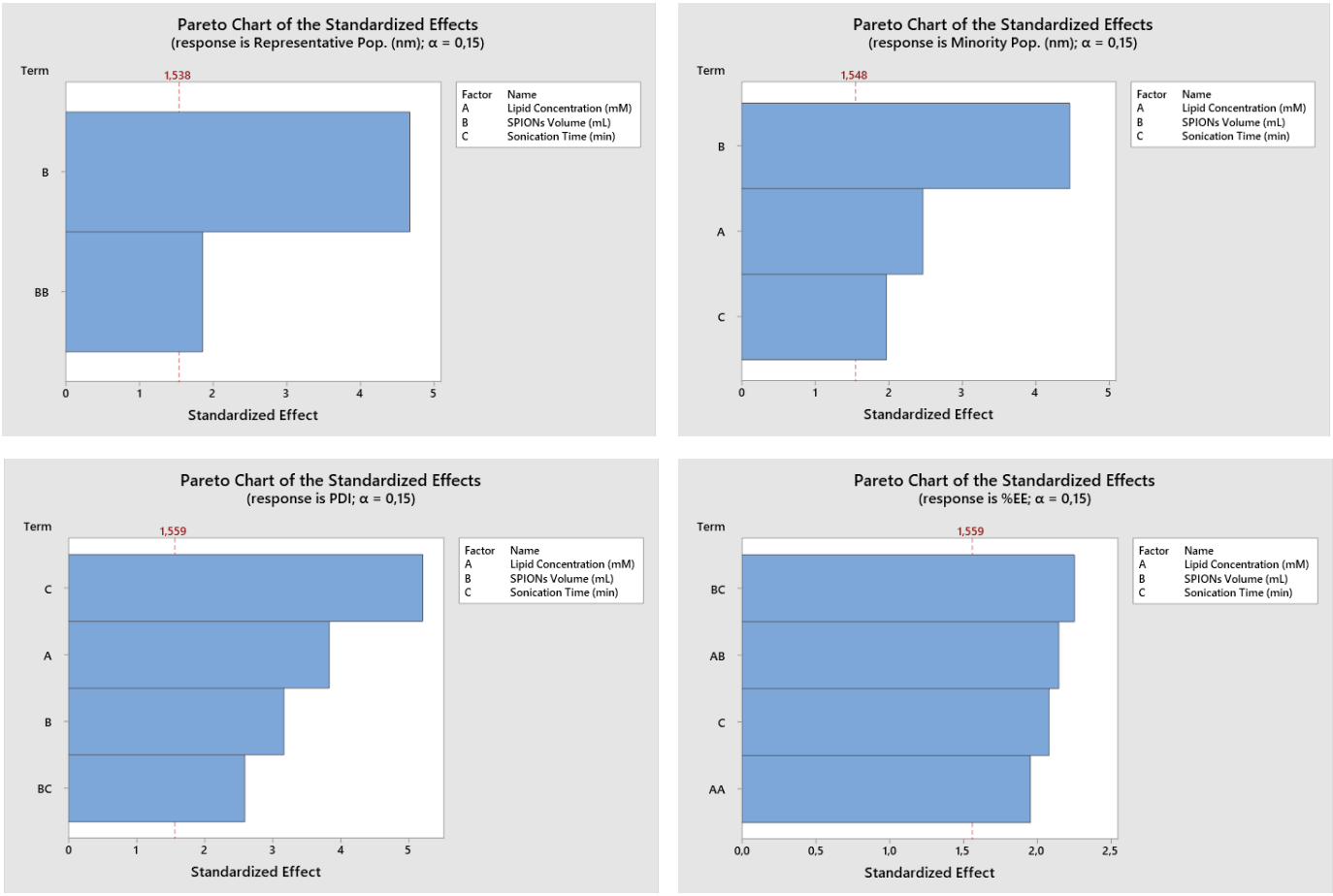

Figure SI 3 - Impact of each term in both populations, PDI and encapsulation efficiency, illustrated by a Pareto Chart

Regression Equation in Uncoded Units

Mean Size (nm) = -7,6 - 4,79 Lipid Concentration (mM) + 238,9 SPIONs Volume (mL)
+ 123,2 Sonication Time (min)
+ 0,318 Lipid Concentration (mM)*Lipid Concentration (mM)
- 6,42 Lipid Concentration (mM)*SPIONs Volume (mL)
- 4,46 Lipid Concentration (mM)*Sonication Time (min)

Representative Pop. (nm) = 76,7 - 49,7 SPIONs Volume (mL)
+ 43,5 SPIONs Volume (mL)*SPIONs Volume (mL)

Minority Pop. (nm) = 148,4 - 4,84 Lipid Concentration (mM) + 175,2 SPIONs Volume (mL)
+ 38,7 Sonication Time (min)

PDI = 0,2411 - 0,002300 Lipid Concentration (mM) - 0,0280 SPIONs Volume (mL)
- 0,0128 Sonication Time (min) + 0,0440 SPIONs Volume (mL)*Sonication Time (min)

Figure SI 4 - Regression Equation for mean size, both populations and PDI

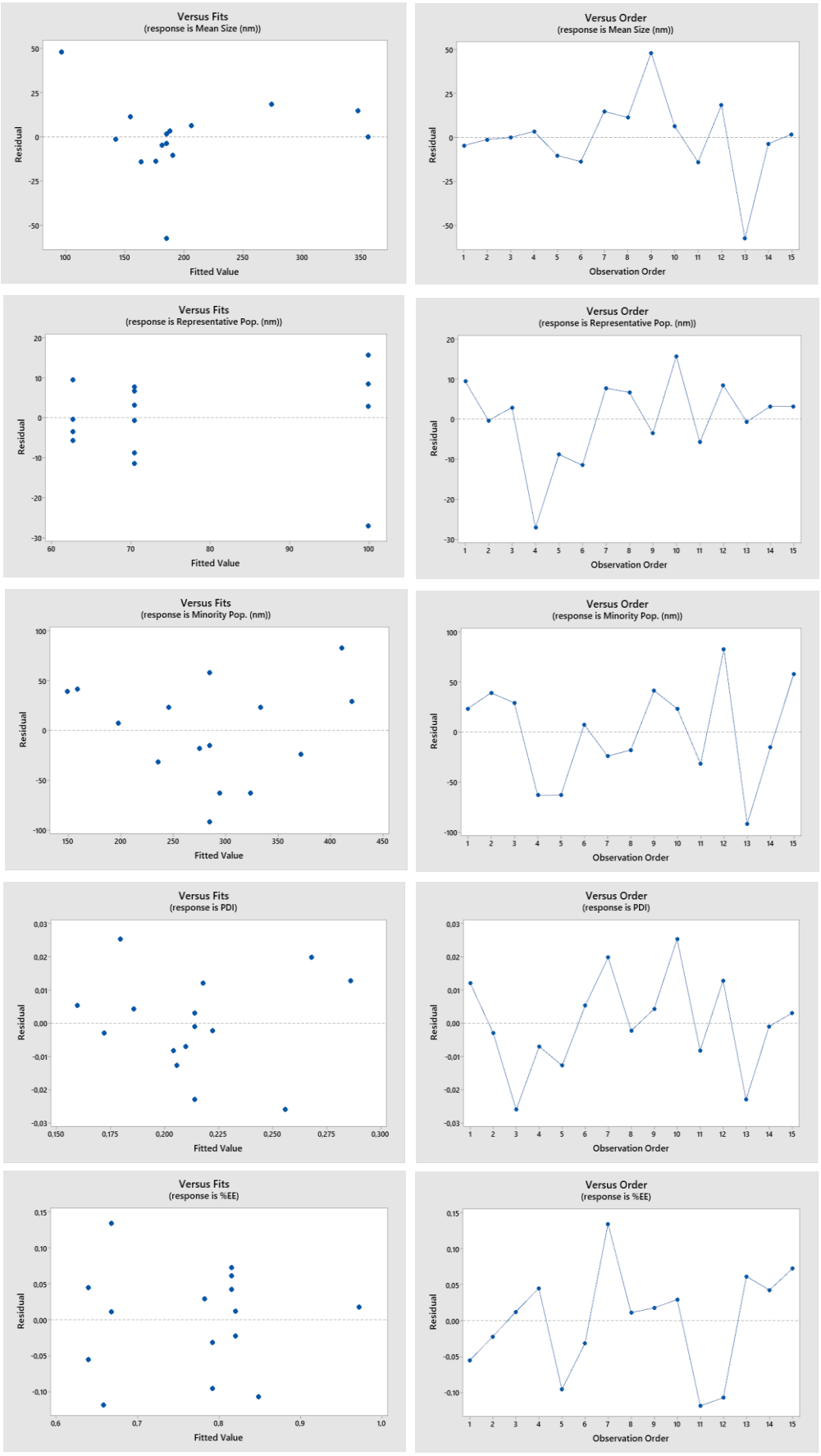

Figure SI 5 – Residual graphics for all the variables

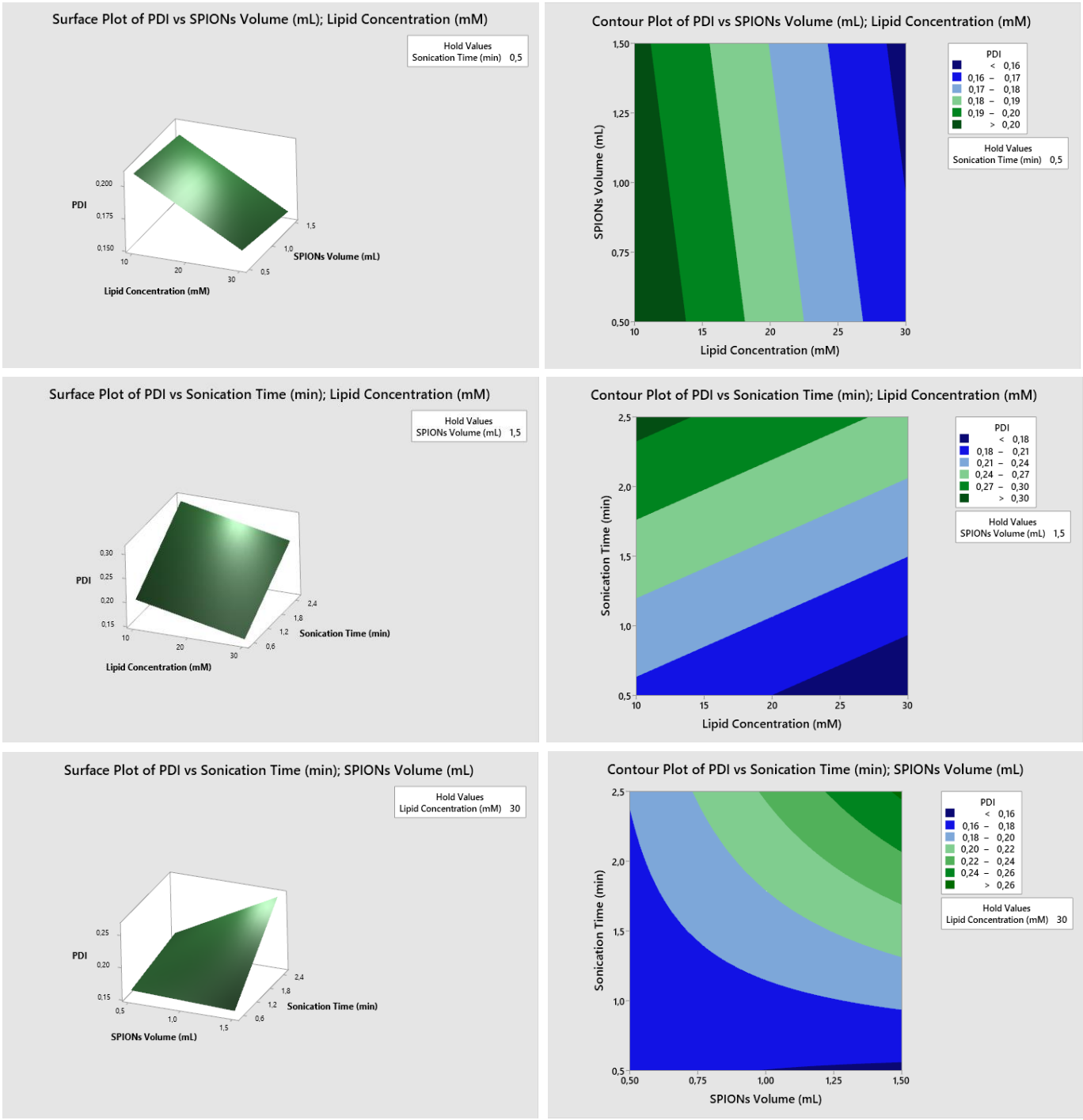

Figure SI 6 - Surface and Contour plots for PDI

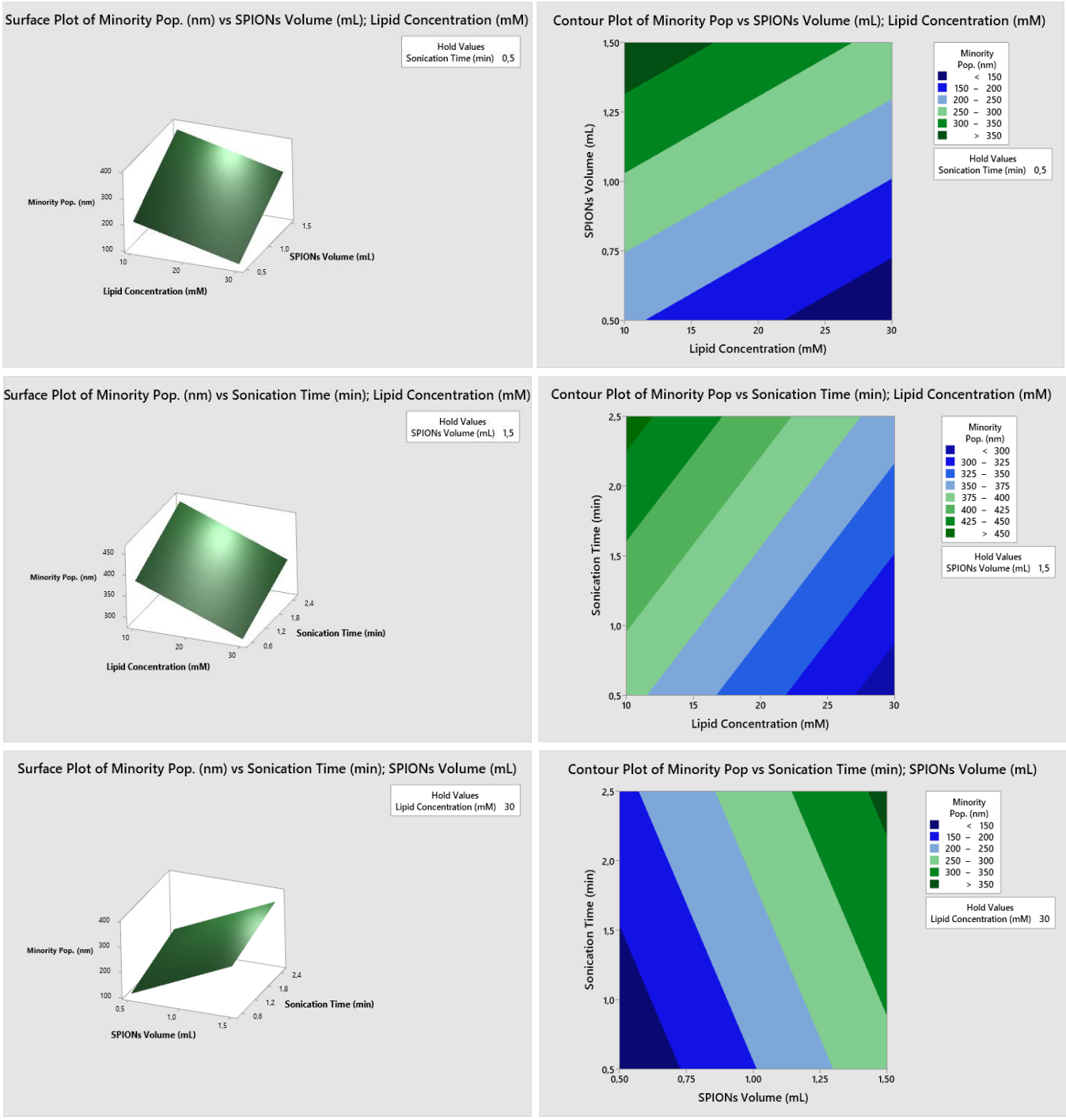

Figure SI 7 - Surface and Contour plots for minority population

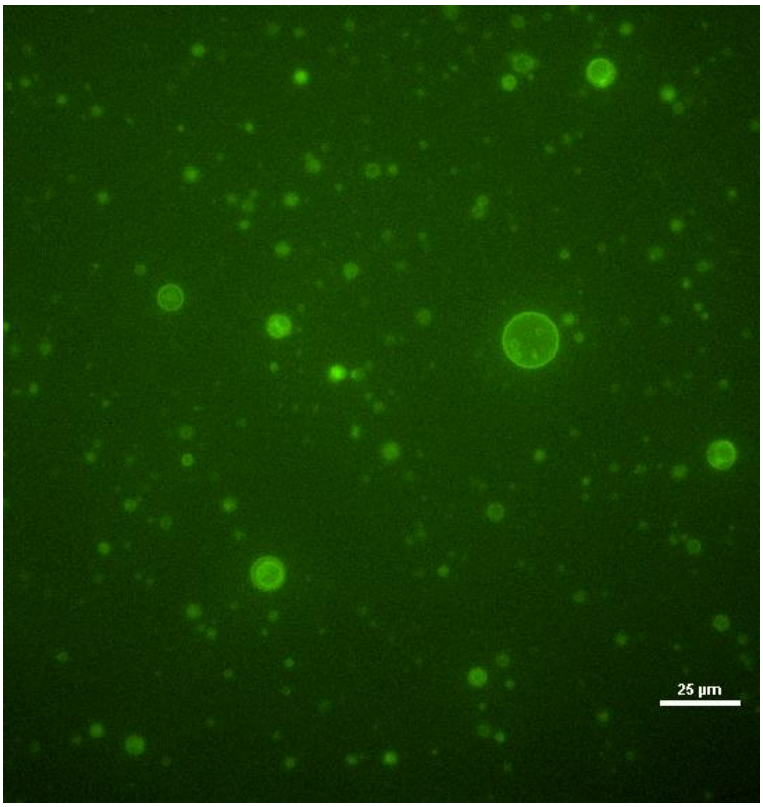

Figure SI 8 - GUVs 1:3 (40x objective), a day after the electroformation

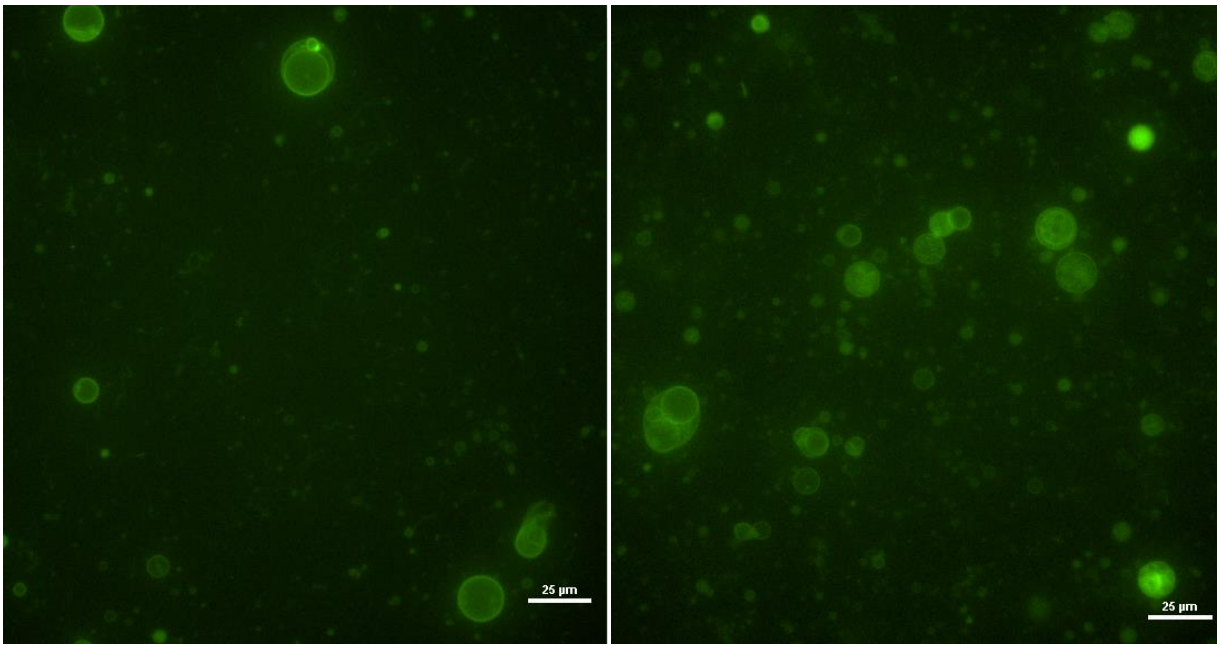

Figure SI 9 - GUVs 1:3 (40x objective), obtained from the same sample

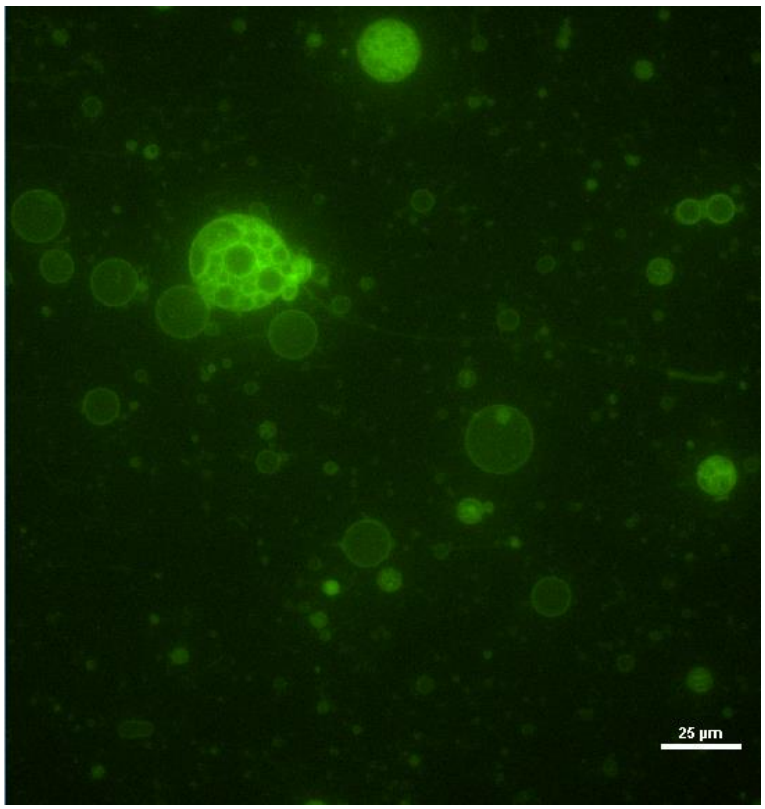

Figure SI 10 - GUVs 1:3 (40x objective), after a dialysis protocol

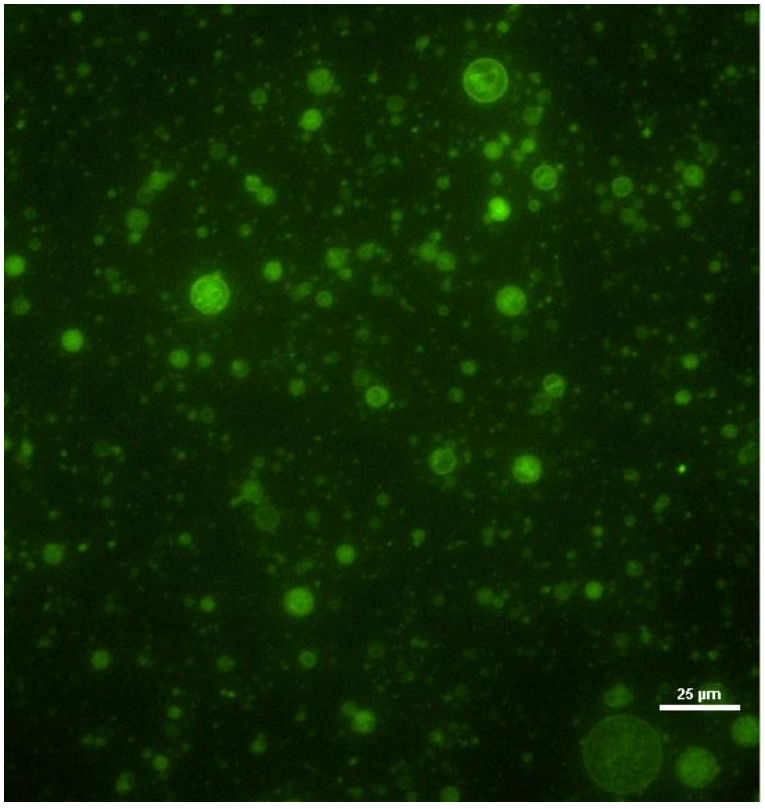

Figure SI 11 - GUVs 1:3 (40x objective), after passing through a 0,45 µm filter

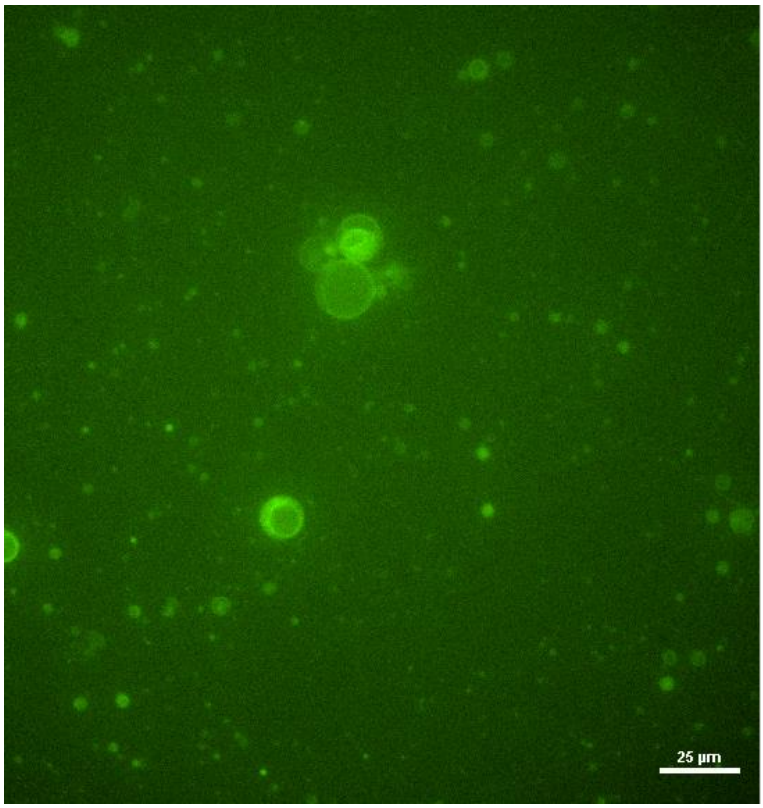

Figure SI 12 - GUVs 1:3 (40x objective), after a 200-rpm centrifugation for 5 minutes (supernatant)